TOHOKU
UNIVERSITY

The 14th International Symposium on Water Environment Systems

---with Perspective of Global Safety

19th ~ 20th November, 2026

Department of Civil and Environmental Engineering
Graduate School of Engineering
Tohoku University

GP-RSS
International Joint Graduate Program in Resilience and Safety Studies

SyDE
WISE Program for Sustainability in the Dynamic Earth
変動地球共生学卓越大学院プログラム

SPONSORS



International Joint Graduate Program in Resilience and Safety Studies of Tohoku University

http://gp-rss.tohoku.ac.jp/



WISE Program for Sustainability in the Dynamic Earth of Tohoku University

https://syde.tohoku.ac.jp/



Department of Civil and Environmental Engineering, Graduate School of Engineering, Tohoku University
https://www.eng.tohoku.ac.jp/

Graduate School of Environmental Sciences, Tohoku University
https://www.kankyo.tohoku.ac.jp/

ORGANIZERS

Dr. So KAZAMA	Professor, Tohoku Univ
Dr. Yu-You LI	Professor, Tohoku Univ
Dr. Daisuke SANO	Professor, Tohoku Univ
Dr. Keiko UDO	Professor, Tohoku Univ
Dr. Kengo KUBOTA	Associate Professor, Tohoku Univ
Dr. Mohan AMARASIRI	Associate Professor, Tohoku Univ
Dr. Janaka Bamunawala	Assistant Professor, Tohoku Univ
Dr. Yusuke HIRAGA	Assistant Professor, Tohoku Univ

SECRETARIAT

Dr. Yu QIN	Assistant Professor, Tohoku Univ
Dr. Wakana OISHI	Assistant Professor, Tohoku Univ
Dr. Yujie CHEN	Assistant Professor, Tohoku Univ
Dr. Nanako INOKAWA	Assistant Professor, Tohoku Univ
Ryota MAEDA	DC Student, Tohoku Univ
Yilei WANG	DC Student, Tohoku Univ

PARTICIPANTS

Nagoya Institute of Technology

Toshikazu KITANO	Professor

Central Environmental Authority (CEA), Sri Lanka

Himali Karunaweera	Director

Mahasarakham University (Faculty of Public Health)

Sirapat Khodseewong	Assistant Dean
Rujira Nonsa-ard	Lecturer

Beijing University of Technology, China

Weikang QI	Associate Professor
Cong WANG	Associate Professor
Jingyun WANG	Student
Shiwei GAO	Student
Lijun YIN	Student

King Mongkut's University of Technology Thonburi

Chaiwat EKKAWATPANIT	Associate Professor

Korea Institute of Science and Technology (KIST)

Hyeonjin CHOI	Associate Professor

Kumoh National Institute of Technology

Seong Jin NOH	Associate Professor
Bomi KIM	Researcher
Hyuna WOO	Student
Yaewon LEE	Student

Research Center for Eco-Environmental Sciences, Chinese Academy of Sciences

Qianwen SUI	Associate Professor

University of Wisconsin-Madison

Daniel B Wright	Associate Professor

G. Aaron Alexander	Researcher

University of Moratuwa

Jagath MANATUNGE	Professor
Lalith RAJAPAKSE	Professor
Luminda GUNAWARDHANA	Senior Lecturer

King Mongkut's University of Technology North Bangkok

Weerayuth PRATOOMCHAI	Assistant Professor

Nagoya University

Jiayuan JI	Assistant Professor

The University of Tokyo

Jialing NI	Assistant Professor

Hokkaido University

Yemei LI	Researcher

University of Macau

Rumeng WANG	Researcher

National Yang Ming Chiao Tung University

Tzu-Hsien YU	Student
Yi-Fang WU	Student

Tohoku University

Nanako INOKAWA	Assistant Professor
Atsuya IKEMOTO	Student
Francisco GIVOVICH	Student
Haruki TAMAKAWA	Student
Irfans Maulana FIRDAUS	Student
Keita KUBO	Student
Monton Methaprayun	Student
Ryotaro TAHARA	Student
Ryuto UGAJIN	Student
Sachio IWABU	Student
Shota UCHIZONO	Student

Takayasu YASUGI	Student
Wasitha DILSHAN	Student
Yilei WANG	Student

SYMPOSIUM

19 Nov (Thu) (GMT +9)

8:50 - 9:00 Opening Speech & Group Photo

9:00-12:30 Oral Session I : *Water & Wastewater treatment*

9:00 ~9:30	[Keynote Lecture] Chlorine Inactivation of Antibiotic-Resistant Escherichia coli in Hospital Wastewater **Sirapat Khodseewong**, *Faculty of Public Health, Mahasarakham University*
9:30 ~10:00	[Keynote Lecture] Ageing in a Warming Field: Heat-Related Illness and Perception on Climate Change among Older Smallholder Farmers in Thailand **Rujira Nonsa-ard**, *Faculty of Public Health, Mahasarakham University*
10:00~10:15	***Coffee break***
10:15~10:35	Spatial Estimation of Water Quality Variables in the Natori River Network Using Spatial Statistical Models **Takayasu YASUGI**, *Tohoku University*
10:35-10:55	Reframing Anammox Biofilm Development and Carrier Design from a Mechanobiological Perspective **Rumeng WANG**, *University of Macau*
10:55-11:15	Salinity-Dependent Nitrifier Adaptation Governs Partial Nitritation Stability **Yunjing WANG**, *Beijing University of Technology*
11:15-11:30	***Coffee break & Free discusion***

11:30-13:00 *Lunch Break*

13:00-14:00 Poster Session

Machine learning-based prediction of continuous anaerobic digestion performance in palm oil mill effluent treatment

Yemei LI, *Hokkaido University*

Life Cycle Assessment of Down-flow Hanging Sponge for Small-scale Wastewater Treatment Plants

Shota UCHIZONO, *Tohoku University*

Magnetostrictive Biosensing Platform for Wastewater Surveillance of Immunoglobulin A as a Community-Level Infection Biomarker

Yilei WANG, *Tohoku University*

Salinity-Dependent Nitrifier Adaptation Governs Partial Nitritation Stability

Yunjing WANG, *Beijing University of Technology*

Novel separate aeration self-circulating technology for continuous aerobic granular sludge process: Performance evaluation, hydrodynamic simulation and control strategy

Shiwei GAO, *Beijing University of Technology*

Long-term Nitrogen Removal Performance of an Anaerobic Ammonia Oxidation Membrane Bioreactor

Lijun YIN, *Beijing University of Technology*

Four kinds of probability papers in flood frequency analysis

Toshikazu KITANO, *Nagoya Institute of Technology*

Drought and Flood Assessment in the Ubolratana Reservoir Basin in Northeastern of Thailand Using Using Coupled Water Balance and Flood Models

Weerayuth PRATOOMCHAI, *King Mongkut's University of Technology North Bangkok*

Dynamic urban pluvial flood emulation with SegFormer: Input design and diagnostic evaluation

Hyuna WOO, *Kumoh National Institute of Technology*

Reservoir regulation and scale-dependent flood amplification under warming climates: a WRF-Hydro storyline of Typhoon Hinnamnor in the Nakdonggang basin

Yaewon LEE, *Kumoh National Institute of Technology*

Precipitation-type classification and deep-learning super-resolution of Radar-AMEDAS rainfall

Hyeonjin CHOI, *Korea Institute of Science and Technology (KIST)*

Development of a Dynamic Flood Evacuation Model and Evacuation Strategies

Tzu-Hsien YU, *National Yang Ming Chiao Tung University*

Evaluating Levels of AI Agent in Hydrologic Modeling: A Comparative Analysis via Rainfall–Runoff Simulation

Yi-Fang WU, *National Yang Ming Chiao Tung University*

Evaluation of the accuracy and applicability of 1m Resolution inundation analysis

Nanako INOKAWA, *Tohoku University*

Sensitivity of simulated rice yield-loss events caused by irrigation-reservoir pre-release to the yield-loss threshold

Atsuya IKEMOTO, *Tohoku University*

Precipitation Characteristics at Different Spatial Resolutions Using a Large-Ensemble Climate Dataset

Ryotaro TAHARA, *Tohoku University*

Correction of Precipitation Data for Long-Term Runoff Analysis

Ryuto UGAJIN, *Tohoku University*

Global Classification of Extreme Precipitation Regimes

Irfans Maulana FIRDAUS, *Tohoku University*

What Controls the Rainfall–Discharge Relationship? The Roles of Basin and Rainfall Characteristics Across Japan

Monton Methaprayun, *Tohoku University*

Delineating Rainfall Homogeneous Regions for Japanese Class-A Watersheds Using the Spatial L-Moments (SLAM) Method: A Comparison with MLIT-Defined Regions

Wasitha DILSHAN, *Tohoku University*

Quantifying the Climate Sensitivity of Atmospheric-River-Induced Extreme Precipitation Events

Francisco GIVOVICH, *Tohoku University*

Effects of Low-intervention Channel Management on Aquatic Insect HSI under Future Climate

Keita KUBO, *Tohoku University*

Analysis of the Spatiotemporal Characteristics of Extreme Precipitation Using the Japanese Long-term Regional Reanalysis Dataset RRJ-Conv

Sachio IWABU, *Tohoku University*

Nationwide Assessment of Flood Retention Measures Utilizing Agricultural Land

Haruki TAMAKAWA, *Tohoku University*

14:00-17:30 Oral Session II : *Hydrology & Hydro-ecology*

14:00~14:20	Future Groundwater Stress in the Yom and Nan River Basins under Climate Change **Chaiwat EKKAWATPANIT**, *King Mongkut's University of Technology Thonburi*
14:20~14:40	Modernizing Flood Hazard and Risk Assessment using Gridded Rainfall Data, Stochastic Methods, and Physics-based Modeling **Daniel B Wright**, *University of Wisconsin-Madison*
14:40~15:00	Green Infrastructure and Urban Resilience: Effects on Seasonal Hydrology and Extreme Heat in Milwaukee, Wisconsin, USA **G. Aaron Alexander**, *University of Wisconsin-Madison*
15:00~15:15	***Coffee break***
15:15~15:35	Risk-Based Selection of Water Quality Monitoring Stations for Early Warning at the Ambatale Water Supply Scheme in Sri Lanka **Lalith RAJAPAKSE**, *University of Moratuwa*
15:35~15:55	Enhancing Health Security through Strengthened Legal Governance, Institutional Integration, and Technological Advancement for Sustainable Water Management in the Kelani River Basin, Sri Lanka **Himali Karunaweera**, *Central Environmental Authority (CEA), Sri Lanka*
15:55~16:15	Correlation-Based Assessment of Water Quality Parameters in the Kelani River Basin, Sri Lanka **Jagath MANATUNGE**, *University of Moratuwa*
16:15~16:30	***Coffee break***
16:30~16:50	An Overview of Water Quality in the Kelani River Basin: Current Status and Spatial Temporal Changes **Luminda GUNAWARDHANA**, *University of Moratuwa*
16:50~17:10	Model and data interactions for hydrologic prediction in a changing climate **Seong Jin NOH**, *Kumoh National Institute of Technology*
17:10~17:30	Beyond rainfall maxima: multi-storyline hydrodynamic assessment of inundation extremes under climate change **Bomi KIM**, *Kumoh National Institute of Technology*

17:30 - 17:45 General discussion & Closing Remarks

18:00 - 20:00 Network Dinner

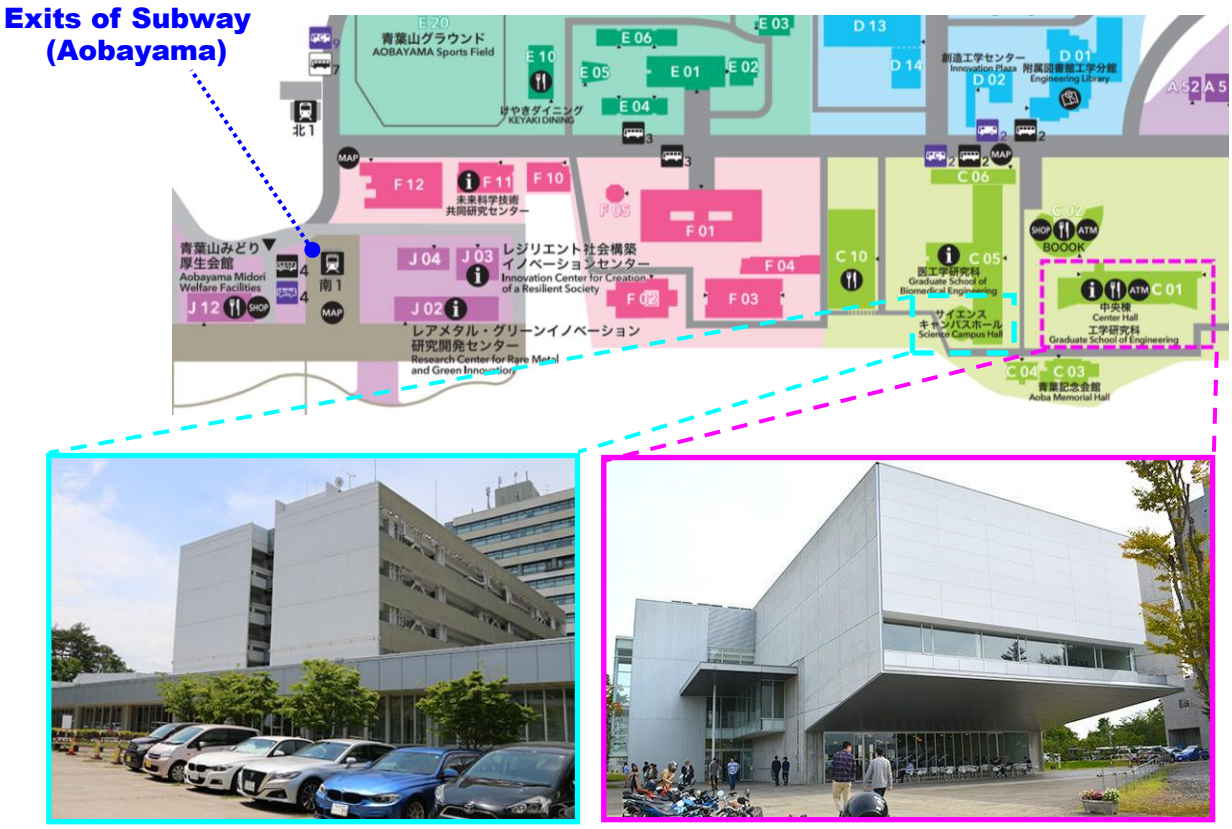
20 Nov (Fri) FIELDWORK (On demand)

VENUE

School of Engineering, Aobayama New Campus, Tohoku University

東北大学大学院工学研究科　青葉山キャンパス

- Conference: Science Campus Hall (C05)
  （会場：サイエンスキャンパスホール(C05)）
- Network Dinner: Center Hall & Aoba Restaurant (C01)
  （懇親会：工学部中央棟・工学部食堂(C01)）

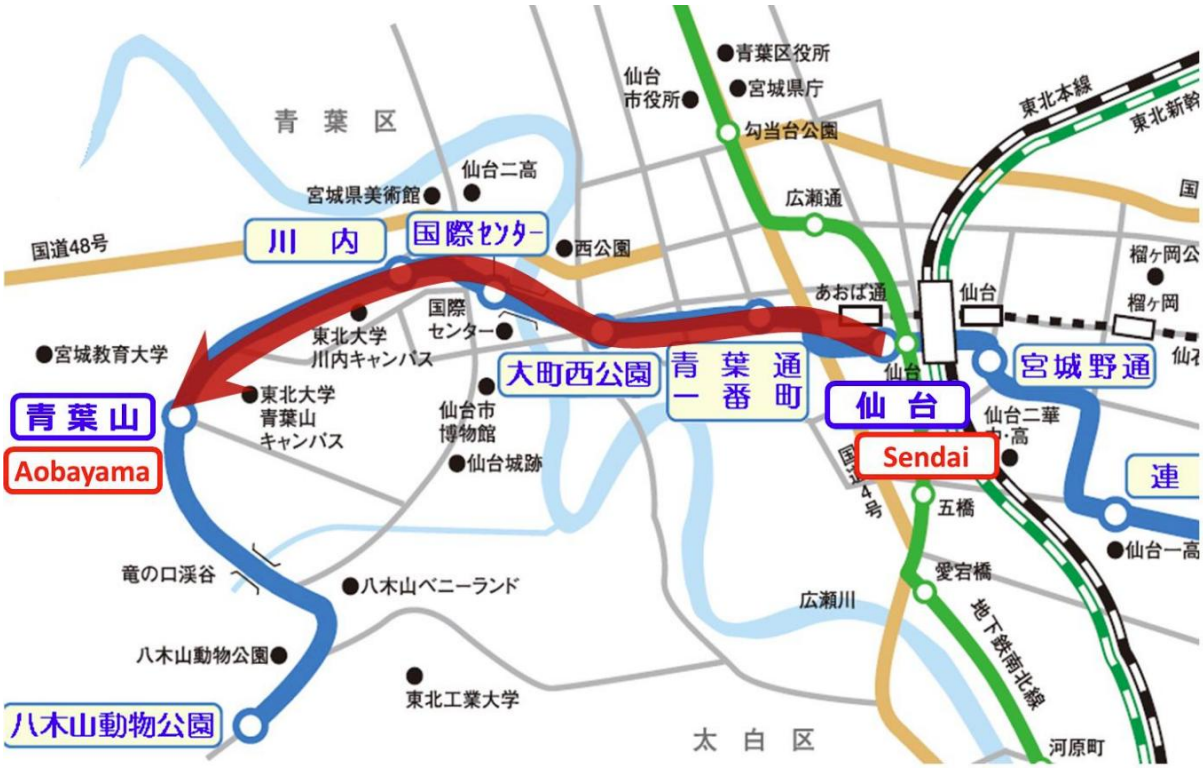


Left: Science Campus Hall (On south of School of Engineering Administration Office)

(C05, サイエンスキャンパスホール、工学部管理棟の南側)

Right: Center Hal & Aoba Restaurant (C01, 工学部中央棟・工学部食堂)

ACCESS



Public access: Only Subway **Tozai Line** is recommended.

If you start from **Sendai Sation** (or Aoba-dori Ichiban-cho), please take the direction of Yagiyama Zoological Park (Yagiyama Dobutsu Koen) and get off at **Aobayama**. (Ticket fee: 250 Yen)

公共交通機関：　地下鉄・東西線はオススメ

「仙台駅」（又は「青葉通一番町」）から「八木山動物公園」方面に「青葉山」まで。

（運賃：250 円）

Limited Chlorination Performance and Antimicrobial-Resistant *Escherichia coli* in a Full-Scale Hospital Wastewater Treatment System in Northeastern Thailand

○ Napaporn WANGPHUMYAI[1], Benchamaporn KONGCHADI[1], Phanphasa THUMTHIANG[1], Patcharakorn SAKULRANG[1] & Sirapat KHODSEEWONG[1*]

[1]Department of Environmental Health, Faculty of Public Health, Mahasarakham University, Maha Sarakham 44150, Thailand.

[*]E-mail: sirapat.k@msu.ac.th

Abstract

This pilot study compared the abundance and antimicrobial susceptibility of *Escherichia coli* before and after chlorination in a full-scale hospital activated sludge system in Northeastern Thailand. Grab samples were collected at both points in three rounds (July–October 2026). *E. coli* was enumerated using the three-tube most probable number (MPN) method, and six confirmed isolates (three per point) were tested against a 14-antimicrobial panel using Kirby–Bauer disk diffusion (CLSI M100, 2026). Pre-chlorination *E. coli* ranged from 4.1×10^5 to $\geq 2.4 \times 10^6$ MPN/100 mL (geometric mean). In two of the three rounds, post-chlorination concentrations remained at the upper detection limit; therefore, reduction could not be quantified; in the third round, reduction was 0.48 $\log_{10}$ (67%). Pre-chlorination isolates were resistant to penicillin, β-lactam/β-lactamase-inhibitor combinations, third-generation cephalosporins, cefoxitin, ertapenem, gentamicin, and trimethoprim–sulfamethoxazole, but susceptible to imipenem and amikacin. Post-chlorination isolates were mostly susceptible. Full-scale chlorination achieved less than 1 $\log_{10}$ reduction, and ertapenem-resistant *E. coli* entered the disinfection stage, indicating that hospital effluent may remain a pathway for antimicrobial resistance dissemination.

Keywords: antimicrobial resistance, chlorination, *Escherichia coli*, hospital wastewater, and One Health.

1 Introduction

Antimicrobial resistance (AMR) was associated with an estimated 4.95 million deaths worldwide in 2019 [1]. Hospital wastewater concentrates antibiotic residues, resistant bacteria, and resistance genes; in Thailand, it is usually treated on site and chlorinated before discharge. Under controlled laboratory conditions, chlorination of Thai hospital effluent achieved 2.38–4.47 $\log_{10}$ reductions of coliform bacteria [2], but culture-based reductions in full-scale hospital systems can be much lower, around 0.3–1.3 log [3].

In Thailand, extended-spectrum β-lactamase (ESBL)-producing *E. coli* has been recovered from hospital sewers, whereas carbapenem resistance remains rare [4]. Data linking full-scale chlorination performance with the susceptibility of surviving *E. coli* in Northeastern Thai hospitals are scarce. Therefore, this pilot study aimed to compare (i) *E. coli* abundance, (ii) antimicrobial susceptibility patterns of *E. coli isolates,* and (iii) selected physicochemical parameters before and after chlorination in a hospital wastewater treatment system.

2 Materials and methods

Study site and sampling. The study was conducted at a completely mixed activated sludge system (design flow 250 m^3/d) of a hospital in Maha Sarakham Province, with liquid chlorine dosing before a contact tank. Grab samples were collected 15–30 cm below the surface before chlorination and from the chlorine contact tank between 08:00 and 10:00 in three rounds (July–October 2026). Post-chlorination samples were collected in sterile bottles containing sodium thiosulfate, and all samples were kept at 4 °C until analysis.

Enumeration and identification. *E. coli* was enumerated in duplicate by a three-tube MPN method at 10−3, 10−4, and 10^{-5} dilutions [5], with lactose broth (presumptive), EC broth (confirmed), and eosin methylene blue agar (completed). EC broth was incubated at 35–37 °C instead of 44.5 °C owing to shared incubator constraints. Isolates were confirmed by Gram staining and biochemical tests (TSI, MIL, and urease).

Antimicrobial susceptibility testing. Six biochemically confirmed isolates, each from a different colony (three before and three after chlorination), were adjusted to 0.5 McFarland and tested on Mueller–Hinton agar. Each isolate was tested against one antimicrobial group, covering 14 antimicrobials in total (Table 2), and interpreted according to CLSI M100 [6]. pH, turbidity, and electrical conductivity were measured on site.

Data analysis. MPN values were $\log_{10}$-transformed and summarized as geometric means. Log reduction (LR) was calculated as $\log_{10}(N_0) - \log_{10}(N)$, where N_0 and N are the pre- and post-chlorination concentrations, respectively; rounds with censored post-chlorination values (all tubes positive) were reported as not quantifiable.

3 Results and discussion

Abundance of *E. coli*. The pre-chlorination concentrations were high in all rounds (Table 1). In rounds 1 and 2, all tubes were positive at both points ($\geq 2.4 \times 10^6$ MPN/100 mL); therefore, reduction could not be quantified. In round 3, the geometric mean decreased from 4.1×10^5 to 1.3×10^5 MPN/100 mL (LR 0.48; 67%). This reduction lies within the range reported for full-scale hospital systems [3] and far below that achieved under controlled dosing [2]. Because residual chlorine, contact time, and ammonia were not measured, the cause cannot be determined; formation of weaker combined chlorine in ammonia-rich activated sludge effluent is one plausible explanation that warrants

verification. Culture-based MPN also misses viable but non-culturable cells [3].

Table 1 Geometric mean *E. coli* (MPN/100 mL) before and after chlorination (NQ = not quantifiable)

Round	Before	After	LR (log_{10})
1	$\geq 2.4 \times 10^6$	$\geq 2.4 \times 10^6$	NQ
2	$\geq 2.4 \times 10^6$	$\geq 2.4 \times 10^6$	NQ
3	4.1×10^5	1.3×10^5	0.48

Antimicrobial susceptibility. Pre-chlorination isolates showed resistance across five antimicrobial classes, including third-generation cephalosporins, cefoxitin, and ertapenem, while imipenem and amikacin remained active (Table 2). Resistance to cephalosporins, together with cefoxitin, suggests possible ESBL and/or AmpC production. Ertapenem resistance with imipenem susceptibility may reflect AmpC or ESBL combined with porin loss rather than a carbapenemase; however, phenotypic confirmation (combination disk and mCIM) is required. Gentamicin resistance is consistent with the high rate (77%) reported among Thai ESBL-producing *E. coli* [4]. Post-chlorination isolates were mostly susceptible. Because each antimicrobial class was tested on a single isolate per point, this difference cannot be attributed to chlorination, and multidrug resistance [7] could not be assigned at the isolate level.

Water quality. Mean pH increased slightly from 7.95 ± 0.03 to 8.10 ± 0.03 (n = 5), which shifts free chlorine toward the less effective hypochlorite ion. Mean turbidity increased from 33.4 ± 4.3 to 43.4 ± 2.1 NTU, suggesting solids carry-over that can shield bacteria from disinfectants.

Table 2 Inhibition zone diameters (mm) and interpretation of *E. coli* isolates

Antimicrobial (µg)	Before	After
Ampicillin (10)	6 (R)	16 (I)
Amoxicillin–clavulanate (20/10)	6 (R)	15 (I)
Ampicillin–sulbactam (10/10)	6 (R)	23 (S)
Piperacillin–tazobactam (100/10)	11 (R)	30 (S)
Ceftazidime (30)	9 (R)	30 (S)
Cefotaxime (30)	6 (R)	35 (S)
Ceftriaxone (30)	6 (R)	32 (S)
Cefoperazone (75)	6 (R)	34 (S)
Cefoxitin (30)	6 (R)	27 (S)
Ertapenem (10)	16 (R)	38 (S)
Imipenem (10)	23 (S)	32 (S)
Gentamicin (10)	6 (R)	19 (S)
Amikacin (30)	20 (S)	20 (S)
Co-trimoxazole (1.25/23.75)	6 (R)	30 (S)

6 = no inhibition zone (disk diameter); S = susceptible, I = intermediate, and R = resistant.

4 Conclusions

Full-scale chlorination at the studied hospital achieved less than 1 log_{10} reduction of *E. coli* in the only quantifiable round, and *E. coli* resistant to multiple classes, including ertapenem, was present in wastewater before disinfection. Monitoring of free and combined residual chlorine and contact time, wider MPN dilution series, complete antimicrobial panels on larger isolate collections, and phenotypic confirmation of ESBL and carbapenemase production are recommended to address these limitations.

References

[1] Antimicrobial Resistance Collaborators, Global burden of bacterial antimicrobial resistance in 2019: a systematic analysis, Lancet, 399 (2022) 629-655.

[2] S. Suwannasin, S. Sreesai, C. Warodomrungsimun, C. Singhakant, W. Magun, Reduction and regrowth of total coliform bacteria, fecal coliform bacteria, and *E. coli* after chlorine and peracetic acid disinfection in the hospital effluent, ScienceAsia, 50 (2024) 2024026.

[4] C. Runcharoen, K.E. Raven, S. Reuter, et al., Whole genome sequencing of ESBL-producing *Escherichia coli* isolated from patients, farm waste and canals in Thailand, Genome Med., 9 (2017) 81.

[5] American Public Health Association, AWWA, WEF, Standard Methods for the Examination of Water and Wastewater, 23rd ed., American Public Health Association, Washington DC (2017).

[6] CLSI, Performance Standards for Antimicrobial Susceptibility Testing, CLSI supplement M100, Clinical and Laboratory Standards Institute, Wayne, PA (2026).

[7] A.-P. Magiorakos, A. Srinivasan, R.B. Carey, et al., Multidrug-resistant, extensively drug-resistant and pandrug-resistant bacteria: an international expert proposal for interim standard definitions for acquired resistance, Clin. Microbiol. Infect., 18 (2012) 268-281.

Speaker biography

Dr. Rujira NONSA-ARD

Faculty of Public Health, Mahasarakham University, Thailand

Biographical profile

Dr. Rujira Nonsa-ard is a lecturer in the Faculty of Public Health at Mahasarakham University, Thailand. She is also affiliated with the university's Excellent Center for Community Aged Care. Her published work covers community health and biomedical sciences, including health and safety among older adults in rural Thailand. [1,2]

Her research on ageing includes fall prevention among community-dwelling older adults, with attention to the home environment, mobility and preventive behaviours. She has also contributed to a systematic review of fall prevention interventions for older people with cognitive impairment. These studies examine health risks in everyday living environments and approaches to prevention in community settings. [2,3]

Her earlier research was undertaken within the Biomedical Sciences Program at Khon Kaen University. Her publications include work on nutrition and immune-cell function, as well as the relationships between telomere length, resting metabolic rate and aerobic capacity. This academic background spans laboratory research and studies of health in the community. [4,5]

Sources

[1] Mahasarakham University, Faculty of Public Health. Academic staff directory.

[2] Nonsa-ard et al. BMC Geriatrics (2026). Community fall prevention study.

[3] Glangkarn et al. JBI Evidence Implementation (2026). Fall prevention review.

[4] Ruknarong et al. Archives of Allied Health Sciences (2021). Vitamin C and PMN function.

[5] Nonsa-ard et al. International Journal of Molecular Sciences (2022). Telomere length and metabolism.

Spatial Estimation of Water Quality Variables in the Natori River Network Using Spatial Statistical Models

○ Takayasu YASUGI[1*], Mohan AMARASIRI[1] & Daisuke SANO[1]
[1]Department of Civil and Environmental Engineering, Tohoku University, Miyagi 980-8579, Japan.
[*]E-mail: yasugi.takayasu.r8@dc.tohoku.ac.jp.

Abstract
Accurate water quality modeling is essential for effective water resource management and aquatic ecosystem conservation; however, it remains challenging due to flow heterogeneity and complex chemical reactions within river networks. While spatial stream network (SSN) models address spatial connectivity and stream distance through network-based covariance structures, the optimal model structure can vary significantly depending on the target water quality variable and observation period. This study investigates the applicability of SSN models for predicting water temperature, pH, dissolved oxygen (DO), and biochemical oxygen demand (BOD) in the Natori River network, Japan, using monthly observations from April 2023 to March 2025. Eighteen candidate models featuring different combinations of fixed effects and covariance structures were compared using the corrected Akaike information criterion (AICc), and predictive performance was evaluated using leave-one-out cross-validation (LOOCV) with iterative model selection. The selected model structures varied by water quality variables and months, with tail-up covariance frequently selected for pH and nugget-only structures for DO. These findings highlight the critical need to evaluate alternative model structures and predictive performance when applying SSN models to river water quality estimation.
Keywords: Geostatistics; Spatial stream network models; Spatial interpolation; Water quality modeling.

1 Introduction
Although river water quality is monitored at only a limited number of locations, understanding its spatial distribution is essential for evaluating water quality conditions across a river network. However, spatial relationships in river systems are complex, driven not only by geographical proximity but also by the branching structure and hydrological connectivity of the network.

Spatial stream network (SSN) models provide a statistical framework that incorporates stream distance and flow connectivity into spatial covariance structures [1, 2]. These models explicitly represent spatial dependence through tail-up and tail-down covariance components. However, the optimal combination of covariance structures and explanatory variables can vary dependent on the target water quality variables and observation periods. Therefore, evaluating alternative model structures is important for achieving reliable spatial prediction.

This study applies SSN models to evaluate water temperature, pH, dissolved oxygen (DO), and biochemical oxygen demand (BOD) in the Natori River network, Japan. By comparing candidate models with alternative fixed effects and covariance structures across monthly datasets and evaluating their predictive performance, this study aims to examine variations in selected model structures across water quality variables and observation periods, thereby establishing the applicability of SSN models for spatial river water quality estimation.

2 Materials and methods
2.1 Study area and monitoring data
The study was conducted in the Natori River network, in Miyagi Prefecture, Japan. Monthly water quality observations from April 2023 to March 2025 were compiled for four variables: water temperature, pH, dissolved oxygen (DO), and biochemical oxygen demand (BOD). The dataset covered 24 months, with 25–28 monitoring sites available per variable and month. Multiple observations at the same site within a month were averaged.

2.2 Spatial stream network models
For each variable and month, water quality at stream locations was expressed as the sum of a fixed-effect mean, spatial random effects, and a nugget component:

$$Y(s,t) = \beta_{0,t} + \beta_{1,t}H(s) + U(s,t) + D(s,t) + \varepsilon(s,t)$$

where $Y(s,t)$ represents the water quality variable at location s and month t, $H(s)$ represents elevation, $U(s,t)$ and $D(s,t)$ are spatial random effects associated with tail-up and tail-down covariance structures, respectively, and $\varepsilon(s,t)$ is the nugget component.

Tail-up covariance describes spatial dependence between flow-connected locations, incorporating weights derived from upstream contributing area obtained from the Japan Flow Direction Map (J-FlwDir) [3]. Tail-down covariance also allows spatial dependence between flow-unconnected locations. The nugget component represents residual variation not captured by the fixed effects or spatial covariance components.

Two fixed-effect specifications (intercept only and elevation) and nine covariance structures were considered. The covariance candidates included a nugget-only model, exponential and spherical tail-up-only and tail-down-only models, and four combinations of tail-up and tail-down components, yielding 18 candidate models in total. Euclidean covariance was not included.

2.3 Model selection and validation
For each water quality variable and month, the 18 candidate models were fitted by maximum likelihood (ML) using the

SSN2 package [2]. The corrected Akaike information criterion (AICc) was used to select the model with the lowest AICc.

Predictive performance was evaluated using leave-one-out cross-validation (LOOCV). For each withheld monitoring site, all candidate models were refitted using the remaining observations, and the model with the minimum AICc was used to predict the withheld value. This procedure evaluates the predictive performance of the complete model selection and prediction process.

Prediction accuracy was assessed using root mean square error (RMSE), mean absolute error (MAE), and mean error (ME). The performance metrics were calculated by pooling all valid LOOCV predictions across the 24-month period for each variable.

2.4 Spatial prediction

As an example of spatial estimation, the AICc-selected model for water temperature in June 2023 was applied to the river network using all available monitoring observations for that month. Spatial predictions were generated at 207 predefined locations with available elevation data and visualized to illustrate the estimated water temperature distribution along the river network.

3 Results and discussion

AICc-based model selection showed differences in the selected fixed effects and covariance structures among water quality variables and months (Table 1). Elevation was selected as a fixed effect in 17, 23, 2, and 17 of the 24 months for water temperature, pH, DO, and BOD, respectively. Tail-up-only covariance structures were selected for pH in 15 months, whereas nugget-only structures were selected for DO in 19 months. For water temperature, nugget-only and tail-up-only structures were each selected in 10 months. For BOD, nugget-only and tail-down-only structures were selected in 13 and 7 months, respectively.

LOOCV yielded 2,591 valid predictions across the 96 variable-month cases. The pooled RMSE values were 2.381 °C for water temperature, 0.342 for pH, 0.676 mg L^{-1} for DO, and 0.222 mg L^{-1} for BOD (Table 2). The corresponding MAE and ME values are also presented in Table 2.

As an example of spatial estimation, Fig. 1 shows the predicted water temperature distribution in the Natori River network for June 2023.

The frequent selection of tail-up covariance for pH suggests that flow connectivity may contribute to explaining its spatial variation. In contrast, the predominance of nugget-only structures for DO indicates that network-based covariance components were less frequently favored under the tested model specifications. Overall, these results suggest that the suitability of fixed effects and spatial covariance structures may vary among water quality variables and observation periods, emphasizing the importance of considering these differences when modeling spatial water quality distributions.

4 Conclusions

This study applied SSN models to four water quality variables in the Natori River network using AICc-based model selection and LOOCV. The selected fixed effects and covariance structures varied among water quality variables and observation periods, with tail-up covariance frequently selected for pH and nugget-only structures predominating for DO. Spatial prediction of water temperature further illustrated the application of SSN models to unmonitored river locations. These findings highlight the importance of considering variable- and time-specific spatial characteristics when selecting SSN models and evaluating their predictive performance.

Table 1. Frequency of selected fixed effects and covariance structures based on AICc.

Model component	Temp.	pH	DO	BOD
Elevation	17	23	2	17
Nugget only	10	9	19	13
Tail-up only	10	15	5	3
Tail-down only	4	0	0	7
Tail-up + Tail-down	0	0	0	1

Note: Values indicate the number of months (out of 24). Elevation represents the selected fixed effect, while the remaining rows represent covariance structures.

Table 2. Pooled LOOCV performance of SSN models selected using AICc.

Variable	n	RMSE	MAE	ME
Water temperature	648	2.381	1.647	-0.029
pH	648	0.342	0.247	-0.013
DO	647	0.676	0.472	-0.004
BOD	648	0.222	0.152	0.002

Note: Metrics were calculated by pooling all valid LOOCV predictions across 24 months. n denotes the number of predictions; ME denotes mean error. Error metrics are in °C for water temperature, mg L^{-1} for DO and BOD, and dimensionless for pH.

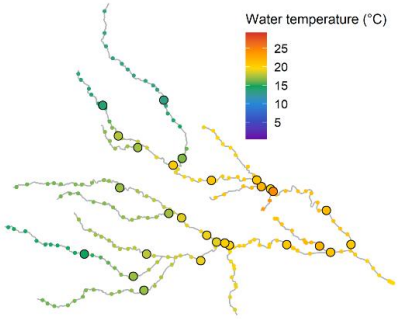


Fig. 1. Spatial distribution of predicted water temperature in the Natori River network in June 2023. Large circles indicate observed values, while small circles indicate predicted values.

References

[1] Ver Hoef, J. M., Peterson, E. E., Clifford, D., and Shah, R., SSN: An R package for spatial statistical modeling on stream networks, J. Stat. Softw., 56(3) (2014) 1–45.

[2] Dumelle, M., Peterson, E. E., Ver Hoef, J. M., Pearse, A., and Isaak, D. J., SSN2: The next generation of spatial stream network modeling in R, J. Open Source Softw., 9(99) (2024) 6389.

[3] Yamazaki, D., Togashi, S., Takeshima, A., and Sayama, T., High-resolution flow direction map of Japan, Journal of JSCE, 8(1) (2020) 234–240.

Reframing Anammox Biofilm Development and Carrier Design from a Mechanobiological Perspective

○ WANG RUMENG[1*], KONG QIUYUE[1], SONG JIANCHEN[1], LIU SIJIA[1] & HAO TIANWEI[1]
[1]Department of Civil and Environmental Engineering, Faculty of Engineering, University of Macau, Macau, 999078, China
[*]E-mail: wangrm21@163.com.

Abstract

The transition to low-carbon and energy-efficient wastewater treatment has become a central priority for modern wastewater treatment plants. Anaerobic ammonium oxidation (anammox) offers a transformative autotrophic pathway for nitrogen removal. However, despite the use of carrier-based biofilm systems to retain slow-growing anammox bacteria (AnAOB), reactor start-up commonly requires 150-300 days or longer, constraining large-scale implementation. To overcome this bottleneck, carrier development requires a shift from empirical trial-and-error screening to mechanism-guided rational design. Our preliminary studies were the first to demonstrate that AnAOB can actively respond to carrier stiffness as a mechanical cue, thereby translating it into a AnAOB retention and biofilm growth advantage, with preliminary validation achieved at pilot scale. Importantly, this provides a quantifiable and manufacturable route for mechanobiology-driven carrier design while reducing potential risks associated with chemical modification.

In engineered bioflim reactors, carrier stiffness, evolving extracellular matrix stiffness, and hydrodynamic shear jointly shape the mechanical environment experienced by microbial communities; yet their mechanic cues-responsive mechanisms remain largely unresolved. Mechanobiology provides a novel perspective and a mechanistic basis for linking dynamic mechanical environments to bacterial adhesion and community organization. However, whether and how AnAOB sense and transduce these mechanical cues, which community members respond, and how these responses regulate cell adhesion and biofilm development require more rigorous mechanistic investigation.

Building on these findings, this Perspective reexamines anammox biofilm development through the potential processes of mechanosensing, mechanotransduction, intracellular responses, and cellular adaptation. Integrating principles of cellular biomechanics and carrier structural mechanics with advances in bacterial mechanobiology over the past two decades, we propose three central perspectives: **(1)** Surface properties shape mechanical cues and seed biofilm heterogeneity; **(2)** Substrate stiffness governs dynamics and self-organization of nascent biofilms; and **(3)** Matrix viscoelasticity mediates mechanobiological feedback and biofilm adaptation.

This Perspective aims to bridge fundamental bacterial mechanobiology and engineered anammox carrier design, providing a mechanistic framework for understanding AnAOB biofilm development and an application-oriented strategy to shorten reactor start-up, enhance biomass retention, and facilitate the broader implementation of anammox technology.

Keywords: anaerobic ammonium oxidation; biofilm; mechanobiology; surface adhesion; carrier stiffness.

1 Introduction

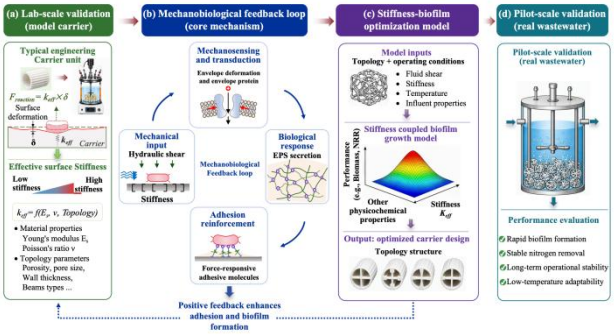


Fig. 1. Conceptual framework and multiscale design-validation pathway for translating bacterial mechanobiology into tunable carrier design parameters for engineered anammox biofilm reactors. (a) Carrier unit stiffness regulation and lab-scale validation; (b) Mechanobiological feedback loop; (c) Stiffness coupled with biofilm growth model; (d) Pilot-scale validation of optimized carriers

2 Acknowledges

The authors would like to thank the Science and Technology Development Fund of Macao S.A.R (FDCT) (0103/2024/AMJ and 0030/2024/AGJ), Research Committee of University of Macau (MYRG-GRG2025- 00166-FST), and Shenzhen-Hong Kong-Macau Science and Technology Project (grant no. EF2023-00072-FST) for their supports.

Salinity-Dependent Nitrifier Adaptation Governs Partial Nitritation Stability

○ Yun-Jing Wang[1], Wei-Kang Qi[1*]
[1] National Engineering Laboratory for Advanced Municipal Wastewater Treatment and Reuse Technology, Engineering Research Center of Beijing, Beijing University of Technology, Beijing 100124, China.
[*]E-mail: qiweikang10@163.com

Abstract

Salinity stress is a promising strategy for establishing partial nitritation (PN). Nevertheless, the adaptation of nitrifiers and its implications for PN stability under dynamic saline conditions remain poorly understood. In this study, a continuous-flow self-circulating up-flow fluidized bed reactor (AOA_N-Zier) was employed to systematically investigate the effects of salt loading rate (SLR) fluctuations on nitrifier functional responses and PN resilience under different salinity backgrounds. PN was rapidly established within 7 d under salt-free conditions, achieving a nitrite accumulation ratio (NAR) of 96% on day 9. Subsequent responses to SLR reduction differed depending on salinity history. At 10 g/L salinity, reduced SLR alleviated nitrite-oxidizing bacteria (NOB) inhibition and resulted in PN deterioration. In contrast, after long-term exposure to 30 g/L salinity, the system maintained an average NAR of 99% despite SLR reduction, owing to the sustained loss of NOB functional activity. Activity assays, microbial succession, and metagenomic analyses revealed that PN resilience was primarily determined by NOB absolute activity rather than the relative activity balance between AOB and NOB. Long-term saline selection promoted functional divergence among nitrifiers, with salt-adapted Nitrosomonas maintaining ammonia oxidation capacity through coordinated osmotic regulation, nitrogen metabolism, oxidative stress defense, and energy conservation. Moreover, the salt-adapted sludge retained high AOB activity after desalination under mainstream-like low-ammonium conditions. This study provides new insights into salinity-dependent nitrifier adaptation and advances the understanding of microbial mechanisms underlying PN resilience under dynamic saline conditions.

Keywords: Partial nitritation; Dynamic saline conditions; Nitrifier adaptation; Absolute activity; *Nitrosomonas*.

1 Introduction

Anthropogenic activities have intensified ammonium pollution, particularly in high-ammonium, carbon-deficient wastewaters. Conventional nitrification–denitrification is energy-intensive and often requires external carbon, increasing operational costs and emissions. In contrast, nitrite is a valuable feedstock for chemical synthesis and energy-storage applications [1]. Given the large nitrogen loads discharged in wastewater worldwide, recovering nitrite offers both environmental and economic benefits.

Salinity can selectively inhibit nitrite-oxidizing bacteria (NOB) while retaining ammonia-oxidizing bacteria (AOB), facilitating PN establishment [2]. However, PN performance varies considerably under similar salinity conditions, suggesting that salinity alone cannot explain system stability. Salt loading rate (SLR) may further influence microbial selection, yet its effects under different salinity histories remain poorly understood.

This study operated a continuous-flow, three-stage self-recirculating reactor (AOA_N-Zier) for 623 days to investigate PN performance under dynamic saline conditions. Specifically, we evaluated SLR effects on nitrifier activity, explored the mechanisms underlying divergent AOB and NOB responses, and assessed the feasibility of maintaining PN after desalination under high- and low-ammonium conditions.

2 Materials and methods

A lab-scale three-column AOA_N-Zier reactor was operated continuously for 623 days to investigate PN under dynamic salinity. It comprised an anoxic column (Zier-A_N), an aerobic column (Zier-O), and an aeration column (Zier-A), interconnected by circulation pipes. Aeration generated an airlift-driven up-flow velocity of 8–16 m/h, while liquid-level and pressure gradients sustained internal circulation. Aeration rate restricted sludge retention to Zier-A_N and Zier-O, whereas Zier-A provided oxygen and circulation only. The effective working volume was 6 L, and temperature was maintained at 25.1 ± 1.5 °C. Synthetic wastewater was fed into Zier-A_N and discharged from Zier-O. The detailed operating conditions for each operational phase are summarized in Table 1.

Table 1. Detailed operating parameters for the AOA_N-Zier.

Period		Days	HRT h	NaCl g/L	NLR kg/m^3/d
Start-up	P1	1-43	18-36	0	0.66
	P2	44-111	30	10	0.66
Salinity shock	P3	112-244	36	10	0.53
	P4	245-337	36	30	0.54
	P5	338-463	45	30	0.42
Resilience	P6	464-623	45-5	0	0.54

3 Results and discussion

PN was established within 7 days under salt-free conditions, with NAR stabilizing at 98 ± 2%, likely due to synergistic FA/FNA inhibition of NOB. At 10 g/L NaCl, PN remained

stable at SLR 12 kg/m³/d (NAR 97 ± 3%) but deteriorated when SLR fell to 10 kg/m³/d (NAR 9%), indicating residual NOB recovery. Increasing salinity to 30 g/L restored PN (NAR 100%), which remained stable after SLR decreased to 24 kg/m³/d (NAR 99.7 ± 0.8%). After desalination and restart, NAR reached 88% on day 1 and averaged 92 ± 8%, remaining above 90% at mainstream-like ammonium levels, demonstrating resilience.

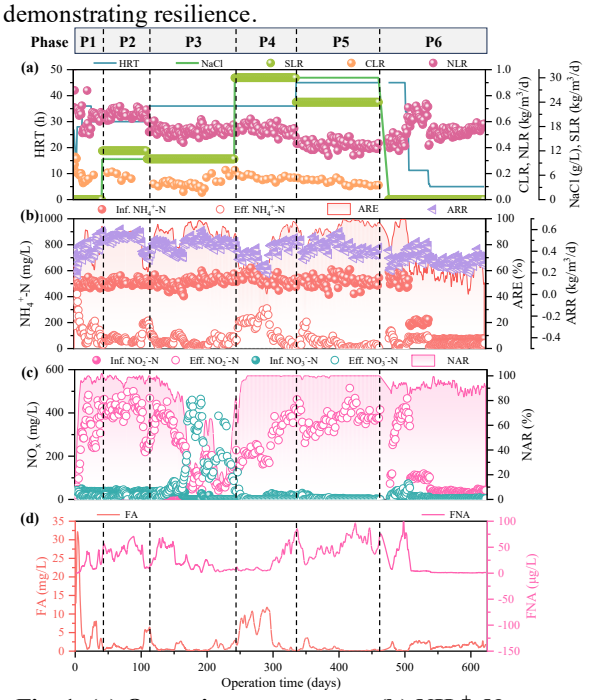


Fig. 1. (a) Operating parameters. (b) NH_4^+–N removal. (c) Profiles of nitrogen species (NO_2^-–N, and NO_2^-–N). (d) Free ammonia (FA) and free nitrous acid (FNA).

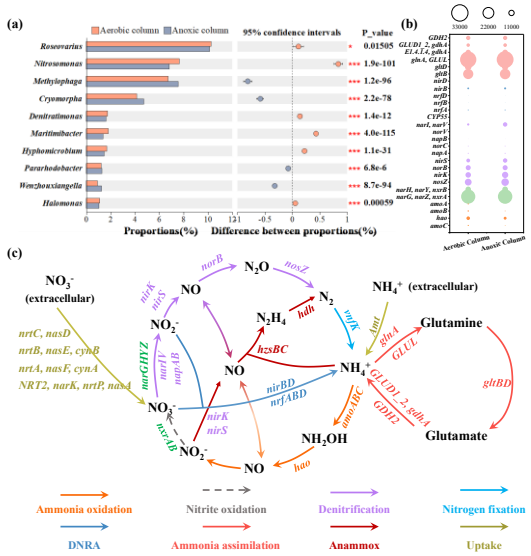


Fig. 2. (a) Significance test of genus-level differences and (b) comparison of nitrogen metabolism gene abundances between aerobic and anoxic columns on day 450; (c) Overall nitrogen metabolic cycle of the AOAN-Zier system under salt shock.

Metagenomics revealed spatial niche differentiation under high salinity. Zier-AN enriched salt-adapted heterotrophs. In contrast, *Nitrosomonas* was enriched in Zier-O, where gene abundance was approximately 1.6-fold higher. Salt-adapted *Nitrosomonas* carried genes associated with osmotic regulation (Na^+ extrusion, K^+ uptake, and compatible-solute metabolism), antioxidant defenses, proton transport, and ATP synthesis. Genes involved in NO production and detoxification suggested mechanisms for managing nitrogen-intermediate stress. Conversely, *Nitrospira* was undetected after prolonged high-salinity exposure, consistent with the absence of NOB recovery. Overall, spatial organization and differential salt adaptation maintained AOB activity while suppressing NOB, supporting stable nitrite accumulation.

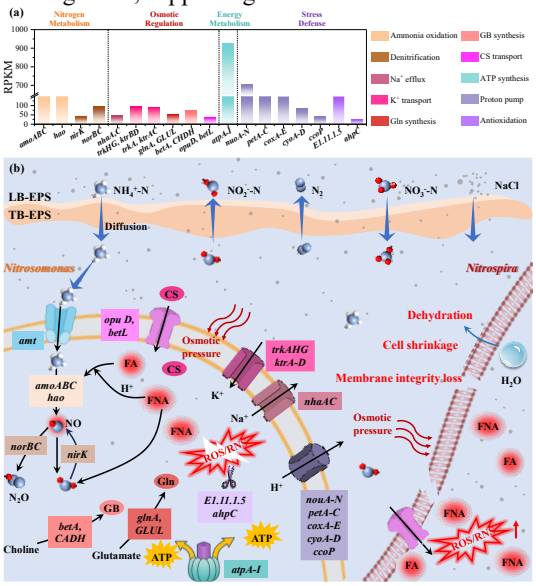


Fig. 3. (a) RPKM expression values of key response genes in *Nitrosomonas*; (b) Schematic mechanism of AOB and NOB responses under salinity stress.

4 Conclusions

PN was established within 7 days under non-saline conditions, reaching an NAR of 96% on day 9. At 10 g/L salinity, reducing the SLR weakened NOB inhibition, increased the nitrite oxidation rate (SNOR) by 232%, and destabilized PN. Conversely, at 30 g/L, NAR remained approximately 99% despite a threefold greater SLR reduction, highlighting the importance of absolute NOB activity rather than relative AOB–NOB activity in determining PN stability. After desalination, salt-adapted sludge sustained high AOB activity and stable PN under mainstream-like low-ammonium conditions. Salinity promoted sludge densification and granulation, while spatial compartmentalization established microbial niches. Metagenomic analysis suggested that *Nitrosomonas* tolerance involved coordinated osmotic regulation, nitrogen metabolism, oxidative stress defense, and energy conservation. These findings inform resilient PN system development through controlled saline selection.

Reference

[1] Zhou, Z., Lv, X., Chen, G., Ma, Z., Lin, B., Li, J., Jiang, L., An, Y. and Tang, R., Salinity propels inward HNO_2 transport to robustly suppress nitrite oxidizers with implications for nitrite recovery. npj Clean Water, 8(1) (2025) 88.

[2] Lin, C., Liu, Y., Li, Y. and Liu, J., Achieving rapid start-up of mainstream partial nitritation by sludge treatment using high salinity. Chem. Eng. J. 483 (2024) 149290.

Machine learning-based prediction of continuous anaerobic digestion performance in palm oil mill effluent treatment

○ Yemei LI[1*], Tao MOTOMURA[1], Adeline Seak May CHUA[2,3], Satoshi OKABE[1] & Mamoru OSHIKI[1]

[1]Division of Environmental Engineering, Hokkaido University, Hokkaido 060-8628, Japan.
[2]Department of Chemical Engineering, Universiti Malaya, Kuala Lumpur 50603, Malaysia
[3]Sustainable Process Engineering Center, Universiti Malaya, Kuala Lumpur 50603, Malaysia.
[*]E-mail: li.yemei@eng.hokudai.ac.jp.

Abstract

Palm oil mill effluent (POME) is a high-strength wastewater generated during palm oil production. It contains high concentrations of organic matter, suspended solids, and residual oil, posing significant environmental risk if discharged without sufficient treatment. Anaerobic digestion (AD) offers a promising approach for POME treatment through organic matter removal and energy recovery. Machine learning (ML) has increasingly been applied in AD performance prediction. This study used random forest models to examine how different types of input information affect the prediction of continuous POME digestion performance. Five feature sets were developed to predict four AD performance indicators. Model accuracy and stability were evaluated using cross-validation and repeated random train-test splits. Among four indicators, methane production rate showed the highest prediction accuracy, with a cross-validation R^2 of 0.863, while methane content remained difficult to predict reliably. Furthermore, combining different types of input information improved prediction accuracy for some indicators, but not for others. These results suggest that different AD performance indicators may require different types of input information for reliable prediction.

Keywords: Anaerobic digestion; POME; Machine learning; methane production; data-driven analysis.

1 Introduction

Palm oil is one of the most widely produced and consumed vegetable oil worldwide, with extensive application in food products, cosmetics, and biofuels. Global palm oil production reached approximately 81 million tonnes in the 2025/2026 marketing year, with Indonesia and Malaysia accounting for the majority of production. Palm oil processing, including fruit sterilization, oil clarification, and hydrocyclone separation, generates substantial quantities of wastewater known as palm oil mill effluent (POME). Approximately 2.5-3.5 tonnes of POME are generated per tonne of crude palm oil produced [1]. POME is characterized by high-strength concentrations of organic matter, suspended solids, and residual oil, which can cause severe environmental pollution if discharged without adequate treatment. Anaerobic digestion (AD) offers a promising approach for POME treatment by simultaneously removing organic pollutants and recovering energy through methane production. However, the performance of continuous AD systems is influenced by organic loading, substrate characteristics, and reactor conditions, making reliable prediction of treatment efficiency and methane production challenging.

Machine learning (ML) has increasingly been applied to predict AD performance by capturing complex relationship between operational parameters and process outputs. Compared with conventional empirical approaches, ML models offer greater flexibility in describing nonlinear relationships and interactions among multiple process variables. However, their predictive performance strongly depends on the quality and availability of experimental data. The selection of input variables remains an important consideration, particularly when experimental data are limited. Therefore, this study applied a random forest (RF) model to continuous POME digestion data to evaluate the influence of input information on the prediction of different AD performance indicators.

2 Materials and methods

2.1 Data source and preparation

The dataset was obtained from a published study by Khemkhao et al. [2], which investigated the continuous anaerobic treatment of raw POME using a modified continuous stirred-tank reactor. The reactor was operated at 55°C with a working volume of 5.8 L and a hydraulic retention time of 3.3 days. During the experimental period, the organic loading rate was progressively increased from 2.0 to 19.0 g-COD/L/d to evaluate reactor performance under different loading conditions. Operational performance data were extracted from the published figures and organized into a dataset comprising approximately 46 observations. Data quality assessment and exploratory analysis were conducted before model development.

2.2 Machine learning modeling and evaluation

Random forest (RF) is an ensemble learning algorithm that combines multiple decision trees to generate predictions. Each tree is constructed using bootstrap samples and randomly selected input features, while the final regression prediction is obtained by averaging the outputs of individual trees. RF can capture nonlinear relationships and interactions among variables, making it suitable for modeling complex anaerobic digestion processes. In this study, RF regression was employed to predict four performance indicators: methane content, methane production rate, total chemical oxygen demand (tCOD) removal efficiency, and soluble chemical oxygen demand (sCOD) removal efficiency. Five

feature sets (F1-F5) were established to evaluate different categories of input information. F1 included organic loading information, while F2 and F3 additionally incorporated substrate characteristics and liquid-phase parameters, respectively. F4 combined these three categories, and F5 further included operational time. The dataset was randomly divided into training (80%) and testing (20%) subsets. Model hyperparameters were optimized using five-fold cross validation. Predictive performance was evaluated using the coefficient of determination (R^2) and root mean squared error (RMSE).

3 Results and discussion

3.1 Prediction performance and feature-set comparison

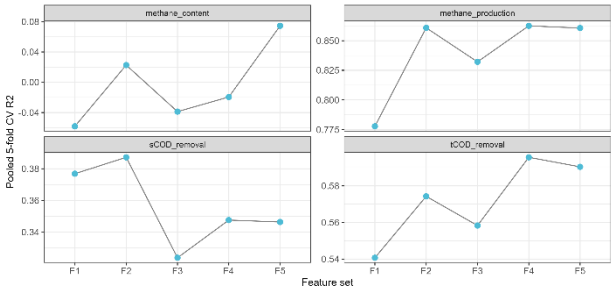


Fig. 1. Five-fold cross-validation performance (R^2) of random forest models using different feature sets for four anaerobic digestion performance indicators.

Fig. 1 compared the five-fold cross-validation (CV) performance of RF models using different feature sets. Methane production rate showed the highest prediction accuracy, with CV R^2 increasing from 0.778 (F1) to 0.863 (F4). The clear improvement from F1 to F2 suggested that adding substrate characteristics provided useful information beyond organic loading alone. While further adding liquid-phase parameters led to only a small improvement, indicating that a relatively simple feature set was sufficient to achieve good prediction accuracy for methane production. For tCOD removal efficiency, the highest CV R^2 of 0.596 was obtained using F4, showing that combining substrate characteristics with liquid-phase parameters improved prediction accuracy. In contrast, sCOD removal efficiency achieved its highest CV R^2 of 0.387 using F2, while more comprehensive feature sets showed no further improvement. This difference may be related to the distinct degradation characteristics of soluble and particulate organic matter in POME. The original reactor study reported relatively stable sCOD removal efficiency but declining tCOD removal efficiency with increasing organic loading, suggesting that the degradation of particulate organic matter become a limiting factor at higher loading rates. Methane content was more difficult to predict than the other indicators, with CV R^2 ranging from approximately -0.06 to 0.08. Its relatively limited variation during reactor operation may explain the poor prediction accuracy. Overall, these results showed that the additional input information does not always improve model performance, and that different performance indicators may require different types of input information.

3.2 Prediction stability and feature interpretation

The stability of RF models was further evaluated using 100 repeated random train-test splits (Fig. 2). For methane production rate, the mean test RMSE decreased from 2.31 (F1) to 1.96 (F5), corresponding to a 15.2% reduction. For tCOD removal efficiency, F4 achieved the lowest mean RMSE of 3.69, representing an 8.6% improvement over F1. In contrast, only a small improvement was observed for sCOD removal efficiency, while methane content remained difficult to predict reliably despite a decrease in RMSE. These results showed that adding more input variables did not always improve prediction accuracy and the benefits varied among different performance indicators.

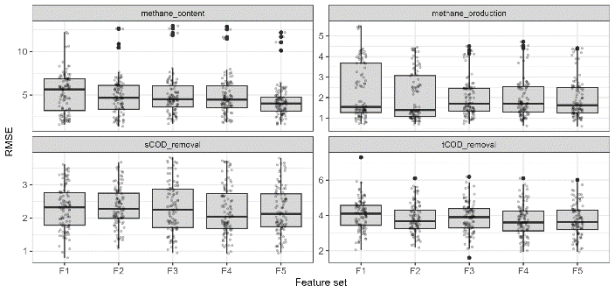


Fig. 2. Distribution of test RMSE obtained from 100 repeated random train-test splits for random forest models using five feature sets.

SHAP analysis of the F4 model showed that influent sCOD and OLR were the most influential variables for methane production prediction, followed by alkalinity. Higher values of these variables generally had positive effects on model predictions, while total volatile acids, substrate composition, and effluent pH had smaller contributions. These results indicated the correlations among input variables should be considered when interpreting their individual contributions.

4 Conclusions

This study showed that the predictive performance of random forest models differed among different performance indicators of continuous POME anaerobic digestion. Methane production rate was predicted most accurately, while methane content remained difficult to predict reliably. Adding substrate characteristics and liquid-phase parameters improved prediction accuracy for some indicators, although increasing the number of input variables did not consistently enhance model performance. SHAP analysis further showed the importance of influent substrate characteristics and organic loading in methane production prediction. Overall, the results indicated that input information requirements should be considered separately for different anaerobic digestion performance indicators.

Acknowledgements

The authors acknowledge financial support from the JST-NEXUS Program under Grant Number JPMJNX25F3.

Reference

[1] Debbie Dominic, Siti Baidurah, Recent developments in biological processing technology for palm oil mill effluent treatment-A review, Biology, 11 (2022) 525.

[2] Maneerat Khemkhao, Somkiet Techkarnjanaruk, Chantaraporn Phalakornkule, Simultaneous treatment of raw palm oil mill effluent and biodegradation of palm fiber in a high-rate CSTR, Bioresource Technology, 177 (2015) 17-27.

Life Cycle Assessment of Down-flow Hanging Sponge for Small-scale Wastewater Treatment Plants

○ Shota UCHIZONO[1*], Kengo KUBOTA[1]
[1]Department of Frontier Science for Advanced Environment, Graduate School of Environmental Studies, Tohoku University, Miyagi 980-8572, Japan.
[*]E-mail: uchizono.shota.t6@dc.tohoku.ac.jp

Abstract

This study applied Life Cycle Assessment (LCA) to evaluate the environmental impacts in the operational phase of two Down-flow Hanging Sponge (DHS)-based systems, Primary Sedimentation Basin (PSB) + DHS and Up-flow Anaerobic Sludge Blanket (UASB) + DHS, and compared them with the Oxidation Ditch (OD), a predominant system for small-scale plants in Japan. A wastewater treatment plant treating 1,000 m³/day was assumed, with 1 m³ of treated water as the functional unit, and environmental impacts were assessed using ReCiPe 2016 and LIME3. DHS-based systems were advantageous for resource damage owing to lower electricity use and sludge generation, but caused greater ecosystem damage because of inferior nutrient removal, particularly phosphorus. In UASB+DHS, volatilization of dissolved methane dominated the damage to human health. The assessment by LIME3 ranked OD lowest (0.125 USD), followed by PSB+DHS (0.143 USD) and UASB+DHS (0.152 USD). Incorporating biological filtration (BF) and greenhouse gas recovery (GR) reduced the impacts of the DHS-based systems below that of OD (PSB+DHS+BF: 0.120 USD; UASB+DHS+GR: 0.105 USD; UASB+DHS+GR+BF: 0.081 USD). These results indicate that, with advanced nutrient removal and methane recovery, DHS-based systems can outperform OD.

Keywords: DHS; LCA; small-scale wastewater treatment plant; PSB; UASB

1 Introduction

Wastewater treatment aims to improve water quality by removing pollutants from wastewater, thereby protecting public health and preserving the water quality of water bodies. Although wastewater treatment is essential for aquatic environmental protection, it also generates environmental impacts through the consumption of electricity and resources associated with the construction and operation of treatment plants, as well as sludge treatment [1]. To achieve a sustainable society, it is necessary to evaluate these environmental impacts throughout the entire life cycle using Life Cycle Assessment (LCA).

Down-flow Hanging Sponge (DHS) is an energy-saving wastewater treatment system that utilizes microorganisms retained on sponge media hung or packed in a reactor. DHS has been evaluated through long-term continuous wastewater treatment tests and implemented in small-scale wastewater treatment plants in Kochi Prefecture, India, and Egypt, demonstrating superior removal performance [2]. In addition to its low energy consumption, DHS is considered to have a low environmental impact because the extended retention of biomass in the sponge promotes self-digestion, thereby reducing sewage sludge production. However, no studies have comprehensively evaluated and compared the environmental impacts of DHS-based systems. In Japan, most wastewater treatment plants are small-scale, with Oxidation Ditch (OD) being predominant [3]. Although OD offers stable treatment performance, it requires continuous aeration, presenting a major drawback of high electricity consumption.

Therefore, this study evaluated the operational environmental impacts of two DHS-based wastewater treatment systems—Primary Sedimentation Basin (PSB) + DHS and Up-flow Anaerobic Sludge Blanket (UASB) + DHS—using LCA. Furthermore, a comparative assessment was conducted against OD, which is widely used in small-scale wastewater treatment plants in Japan.

2 Materials and methods

In this study, we assumed a wastewater treatment plant with a capacity of 1,000 m³/day treating domestic wastewater, equipped with PSB+DHS, UASB+DHS, and OD systems, respectively, and evaluated the environmental impacts during the operation phase of the treatment plant. The system boundary of the LCA ranged from the treatment of domestic wastewater entering the plant to the discharge of treated water, sludge incineration, and the utilization of incineration ash. Influent water quality, removal efficiencies, and sludge generation rates were obtained from previous studies and reports. Emission factors for greenhouse gases generated during DHS water treatment were derived from experimental data, while AIST-IDEA ver. 4.0 was used as the background database for electricity, chemical consumption and transportation. The functional unit was defined as 1 m³ of treated water, and ReCiPe 2016 (H) and LIME3 (interest rate 2%, consumption countries, Japan) were adopted for life cycle impact assessment.

3 Results and discussion

3.1 Damage-based Assessment by ReCiPe2016

This study evaluated the damages to the three protection areas in ReCiPe 2016: human health, ecosystems, and resources. First, regarding damage to human health, all systems showed comparable damage amounts. By process, sludge incineration was the primary contributing factor in OD and PSB+DHS, accounting for 63.1% and 68.7% of the total, respectively. Sludge incineration causes emissions of

greenhouse gases (N_2O and CO_2) and air pollutants (SO_x and NO_x), serving as the major contributor to human health damage in these two systems. In UASB+DHS, which generates less sludge, the impact from sludge incineration was smaller. However, direct greenhouse gas emissions from wastewater treatment accounted for 73.7%. In this study, based on previous research, it was assumed that 53.5% of the methane generated in UASB dissolves into the effluent as dissolved methane and subsequently volatilizes in downstream processes, which resulted in this large contribution [4].

Next, regarding damage to ecosystems, OD showed the lowest damage, followed by PSB+DHS and UASB+DHS. In DHS-based systems, the damage from treated water discharge accounted for the largest proportion. This is because their nutrient removal performance is inferior to that of OD, and phosphorus removal is particularly difficult to achieve. Previous studies evaluated environmental impacts under different scenarios of river discharge and irrigation reuse of treated water, demonstrating that irrigation reuse of treated water can reduce damage to ecosystems [5]. For wastewater treatment systems using DHS, it is considered necessary to reduce ecosystem damage by discharging into areas less susceptible to eutrophication or by adding advanced treatment processes for nutrient removal.

Finally, regarding damage to resources, UASB+DHS showed the lowest impact, followed by PSB+DHS and OD. Electricity consumption and sludge incineration made significant contributions, giving an advantage to wastewater treatment systems using DHS, which feature lower power consumption and sludge generation. While DHS-based systems are superior from the perspective of resources, a trade-off with ecosystem impacts exists.

3.2 Single Score Assessment by LIME3

To make the comparison of environmental impacts clearer, each wastewater treatment system was evaluated using a single indicator (USD) with LIME3. This assessment revealed that OD had the lowest impact (0.125 USD), followed by PSB+DHS (0.143 USD) and UASB+DHS (0.152 USD). Because DHS-based systems exhibited higher environmental impacts compared to OD, improvement plans for these systems were examined. To reduce environmental impacts, a re-evaluation was conducted by assuming the installation of advanced treatment processes to enhance nutrient removal performance, as well as the implementation of direct methane gas recovery equipment from the water treatment process in UASB+DHS. The introduction of a biological filtration (BF) was considered for PSB+DHS, while greenhouse gas recovery (GR) from the DHS reactor and the introduction of BF were considered for UASB+DHS [4, 6]. As a result of system improvement, DHS-based systems achieved lower environmental impacts than OD (PSB+DHS+BF: 0.120 USD, UASB+DHS+GR: 0.105 USD, UASB+DHS+GR+BF: 0.081 USD).

4 Conclusions

This study evaluated the operational environmental impacts of DHS-based systems (PSB+DHS and UASB+DHS) against OD using LCA. While DHS-based systems offered resource conservation advantages through low energy use and sludge reduction, nutrients in treated water discharge increased ecosystem impacts. Incorporating biological filtration and greenhouse gas recovery resolved these issues, enabling DHS-based systems to outperform OD.

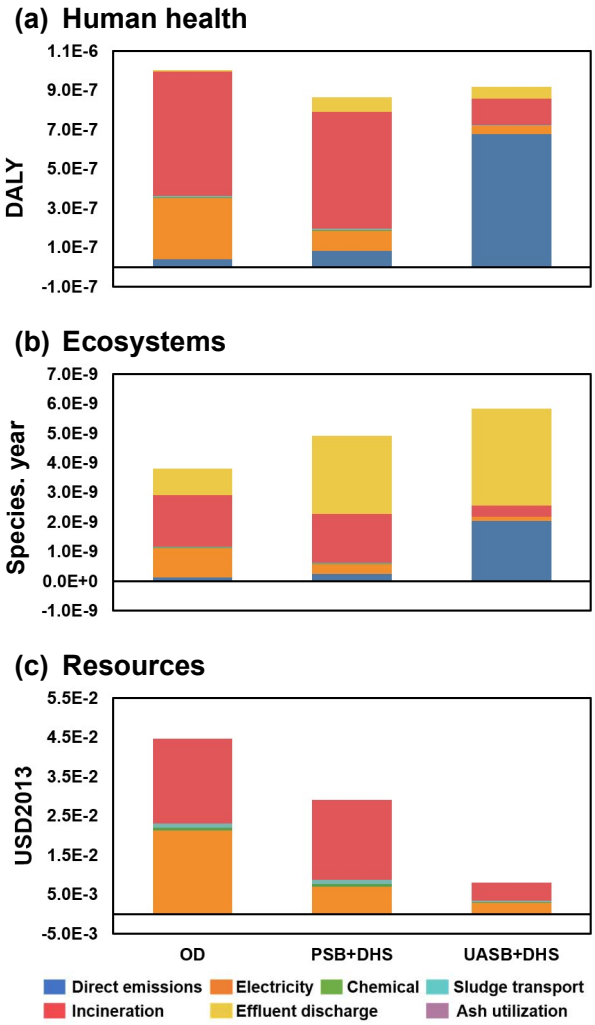


Fig. 1. Damage-based Assessment

Reference

[1] Corominas et al., Life cycle assessment applied to wastewater treatment: State of the art, Water Research, 47, 15 (2013) 5480-5492.

[2] Tyagi et al., Future perspective of energy saving down-flow hanging sponge (DHS) technology for wastewater valorization—a review, Reviews in Environmental Science and Bio/Technology, 20 (2021) 389-418.

[3] Japan Sewage Works Association, Sewerage Statics (2025).

[4] Matsuura et al., Recovery and biological oxidation of dissolved methane in effluent from UASB treatment of municipal sewage using a two-stage closed downflow hanging sponge system, Journal of Environmental Management, 151 (2015) 200-209.

[5] Tayyebi et al., Life cycle assessment, a decision-making tool in wastewater treatment systems: a case study wastewater treatment plant of Ahvaz, Iran, Applied Water Science, 13 (2023) 132-145.

[6] NILIM, Demonstration Project for Flow-Adaptive Water Treatment Technology Using the DHS System, (2024).

Development of a piezoelectrically actuated magnetostrictive biosensor for immunoglobulin A detection

○ Yilei WANG[1*], Ziwen ZHAO[1], Gen TAYAMA[1], Fumio NARITA[1], Atsushi SUENAGA[2] & Daisuke SANO[1]

[1]Department of Frontier Sciences for Advanced Environment, Graduate School of Environmental Studies, Tohoku University, Sendai, Japan.

[2]Meidensha Corporation, Tokyo, Japan.

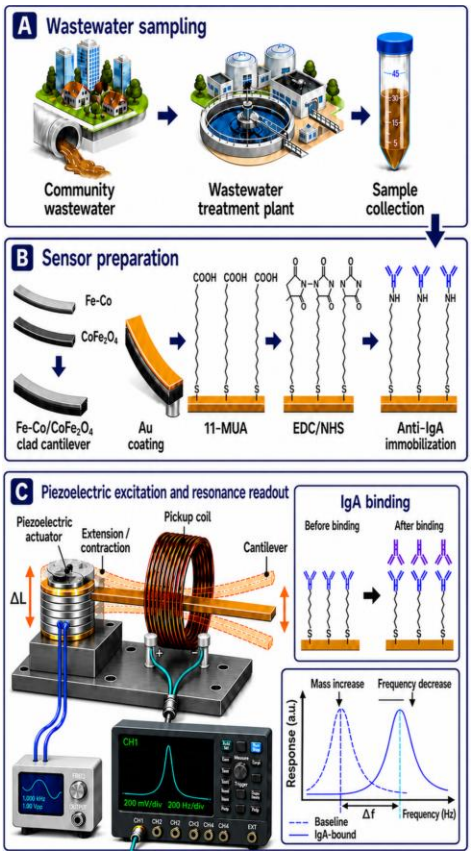
*E-mail: wang.yilei.q4@dc.tohoku.ac.jp

Abstract

Immunoglobulin A (IgA) is a mucosal antibody present in wastewater and a candidate marker of community immune responses. We developed an IgA biosensor based on an anti-IgA-functionalized Fe–Co/$CoFe_2O_4$ clad cantilever, with piezoelectric excitation and pickup-coil readout. Cantilevers of 10, 15, 18 and 20 mm were compared. Resonance frequency followed the inverse square of cantilever length (R^2 = 0.9996), and the 10 mm device showed the highest apparent response per introduced IgA mass, at 0.256 ± 0.055 mHz/ng. In separate PBS exposure experiments, the frequency decrease increased from 0.07 ± 0.06 Hz at 0.0144 mg/mL IgA to 0.33 ± 0.06 Hz at 1.44 mg/mL. Wastewater spiked with 0.144 or 1.44 mg/mL IgA also showed frequency decreases of 0.33 ± 0.06 Hz. The results support further development of a compact sensor for wastewater IgA measurement.

Keywords: immunoglobulin A; magnetostrictive biosensor; cantilever; piezoelectric actuation; wastewater surveillance.

Graphical abstract



Sensor workflow showing wastewater sampling, antibody immobilization, and piezoelectric excitation with magnetic readout.

1 Introduction

Wastewater surveillance measures biomarkers shed by a population to monitor infectious disease circulation [1]. Host-derived biomarkers could add information on community immune responses. Immunoglobulin A (IgA) is a major mucosal antibody released in bodily secretions and excreta. Its presence in wastewater makes it a candidate for monitoring immune activity in the contributing population.

Laboratory assays such as ELISA require several incubation and washing steps. Direct electrical detection of IgA capture could simplify measurement. Magnetostrictive resonators detect mechanical changes through magnetic signals [2]. We use an antibody-functionalized Fe–Co/$CoFe_2O_4$ cantilever to capture IgA and measure the resulting resonance-frequency change. Piezoelectric excitation and pickup-coil readout provide a basis for a compact instrument. This study examines cantilever size and IgA responses in PBS and spiked wastewater.

2 Materials and methods

Anti-IgA antibodies were immobilized on the Fe–Co/$CoFe_2O_4$ clad cantilever through a self-assembled monolayer and EDC/NHS coupling. A piezoelectric actuator excited the fixed end of the cantilever, and a pickup coil recorded the induced voltage during frequency sweeps. Resonance frequency was obtained from the voltage peak.

Cantilever lengths of 10, 15, 18 and 20 mm were compared in three independent experiments per size, with frequency decreases normalized by introduced IgA mass. The 10 mm device was tested with 0.00144–1.44 mg/mL IgA in PBS, successive IgA additions, and spiked wastewater. Each session included a PBS reference and three technical scans. The response was the PBS frequency minus the post-exposure frequency.

3 Results and discussion

Resonance frequency closely followed $1/L^2$, where L is cantilever length ($R^2 = 0.9996$). The 10 mm device gave the highest apparent response per introduced IgA mass, at 0.256 ± 0.055 mHz/ng (Fig. 1, left), supporting its selection for further measurements. IgA loading differed among size groups, and the normalization refers to introduced mass.

The PBS experiments showed frequency decreases of 0.00 ± 0.10, 0.07 ± 0.06, 0.20 ± 0.10 and 0.33 ± 0.06 Hz at 0.00144, 0.0144, 0.144 and 1.44 mg/mL IgA, respectively (Fig. 1, right). Larger decreases occurred at higher concentrations. The lowest-concentration response overlapped zero. Each concentration was measured in a separate session.

During successive additions on the same device, Cantilever 2 showed a 0.40 Hz decrease after the first exposure to 1.44 mg/mL IgA. This response was similar in magnitude to the 0.33 Hz decrease in the separate exposure experiment. Later measurements followed cumulative exposure to IgA.

Wastewater spiked with 0.144 and 1.44 mg/mL IgA showed frequency decreases of 0.33 ± 0.06 Hz at both spike levels (Fig. 2). At the lower additions of 0.00144 and 0.0144 mg/mL, the corresponding responses were −0.47 ± 0.23 and −0.80 ± 0.10 Hz, indicating increases in frequency relative to PBS. The wastewater measurements showed a different response pattern from PBS, with a change in direction across spike levels. This pattern will guide further work on sample preparation and matrix effects.

4 Conclusions

The 10 mm Fe–Co/$CoFe_2O_4$ cantilever showed the highest apparent response per introduced IgA mass and concentration-ordered frequency decreases in PBS. Frequency decreases were also observed at the two higher wastewater spike levels. Further development will address calibration and matrix effects for wastewater IgA measurement.

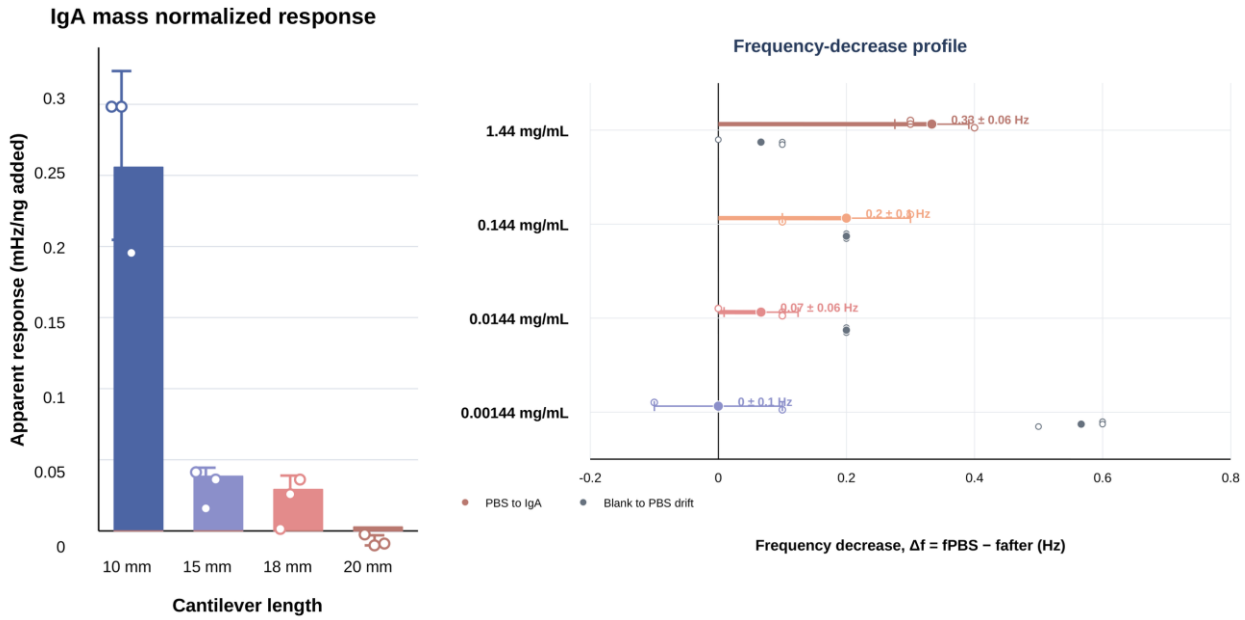


Fig. 1. Cantilever size comparison (left; mean ± SD, three independent experiments per size) and IgA response in PBS (right; mean ± SD, three technical scans). PBS-to-IgA decreases are shown with blank-to-PBS drift.

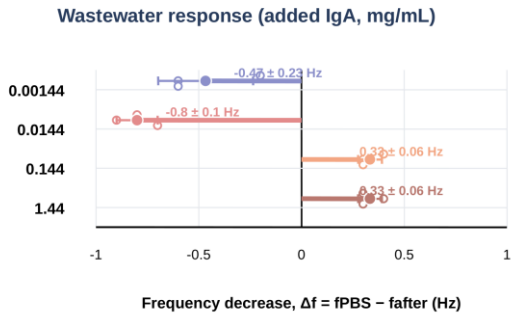


Fig. 2. Frequency response in spiked wastewater relative to PBS (mean ± SD, three technical scans). Positive values indicate frequency decreases.

References

[1] W. Lodder, A. M. de Roda Husman, SARS-CoV-2 in wastewater: potential health risk, but also data source, The Lancet Gastroenterology & Hepatology 5 (2020) 533–534.

[2] C. A. Grimes et al., Wireless magnetoelastic resonance sensors: a critical review, Sensors 2 (2002) 294–313.

Novel separate aeration self-circulating technology for continuous aerobic granular sludge process: Performance evaluation, hydrodynamic simulation and control strategy

○ Shi-Wei Gao[1], Wei-Kang Qi[1*]

[1] National Engineering Laboratory for Advanced Municipal Wastewater Treatment and Reuse Technology, Engineering Research Center of Beijing, Beijing University of Technology, Beijing 100124, China.

[*]E-mail: qiweikang10@163.com.

Abstract

Continuous-flow aerobic granular sludge (AGS) is a promising retrofitting technique for modern wastewater treatment facilities, while stable AGS cultivation and long-term maintenance are severely limited by unreasonable hydrodynamic distributions and complex structural design. The novel Zier system features ultra-high hydraulic parameters (upflow velocity >30 m/h, circulation multiplier >200), which provides sufficient hydraulic shear force for efficient continuous AGS granulation and stabilization. Computational fluid dynamics (CFD) simulations were innovatively applied to systematically optimize its internal hydrodynamics and geometric structure. The optimal superficial gas velocity of 1.3 cm/s, matched with a 1:2 column diameter ratio and a height-diameter ratio of 20, significantly improved the nitrogen removal capacity to over 1.6 kg N/(m³·d) and constructed synergistic CSTR-PFR hybrid flow fields within the reactor. Further experimental validations, including long-term municipal wastewater treatment (C/N = 5.9±1.0) and 110-day low-C/N (2.6) domestic sewage tests with anammox synergy, confirmed its stable granulation morphology and efficient pollutant removal performance. This CFD-based parametric optimization effectively reveals the intrinsic hydrodynamic mechanisms, providing targeted and reliable guidance for the structural design and intelligent operation of novel continuous-flow AGS reactors.

Keywords: Computational fluid dynamics; Aerobic granular sludge; Multiphase Flow Model; Process optimization; Expanded Sludge Bed.

1 Introduction

Computational fluid dynamics (CFD) is a cost-effective, high-resolution tool for characterizing bioreactor hydrodynamics and sludge properties such as particle diameter, density, and bed height [1–4]. Treatment performance relies heavily on suitable flow regimes, and series continuous stirred tank (CSTR) and plug flow (PFR) configurations are widely adopted to ensure sufficient mixing and pollutant removal [5, 6]. Nevertheless, how reactor geometry and sludge properties jointly govern internal flow patterns remains poorly understood. Consequently, CFD is well suited for this analysis. By resolving flow fields, CFD enables targeted operational optimization. Accordingly, we perform a systematic hydrodynamic characterization of the Zier reactor to support the development of its process control strategy [7].

Based on the above background, comprehensive investigations into the Zier reactor are urgently required. The objectives of this study were to (i) characterize hydrodynamic conditions and multiphase interactions considering aeration effects and structural optimization; (ii) explore the influences of granular sludge properties on flow regimes; (iii) validate simulation results with experimental data to clarify the underlying mechanisms; (iv) establish a framework covering optimization, control strategies and scale-up prospects for the Zier reactor. These findings will not only demonstrate the application potential of the Zier reactor but also provide new insights into continuous-flow AGS systems.

2 Materials and methods

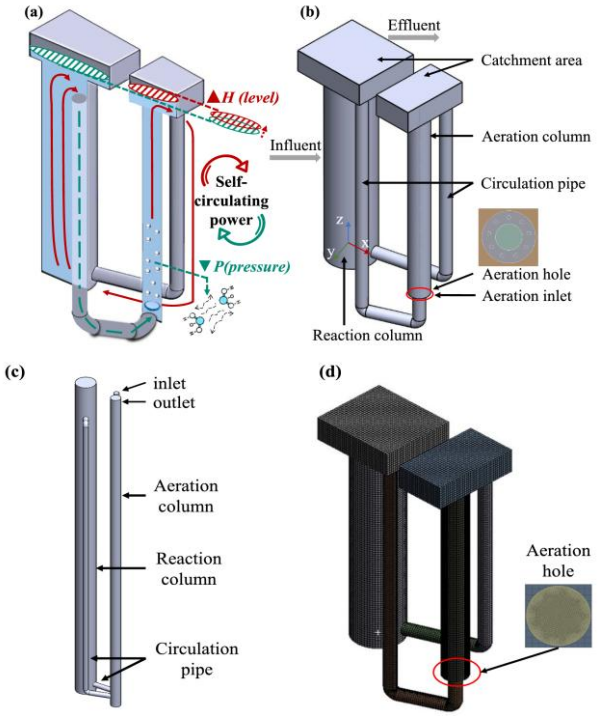


Fig. 1. Simulation model and meshing: (a) schematic diagram of Zier; (b) simulation model for optimization of superficial gas velocity and structure; (c) modified Simulation model for optimization of particle sludge properties; and (d) simulation mesh.

3 Results and discussion

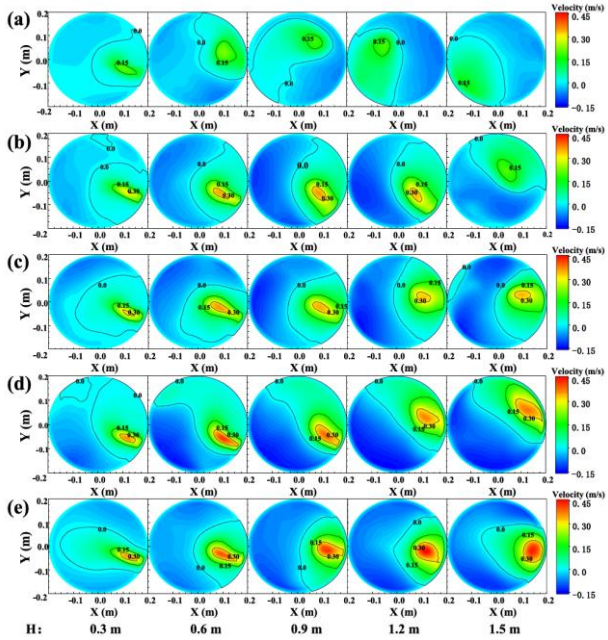


Fig. 2. Contours of liquid velocity at different height (horizontal profile from 0.3 m to 1.5 m) under superficial gas velocity (SGV) = (a) 0.4 cm/s; (b) 0.9 cm/s; (c) 1.3 cm/s; (d) 1.7 cm/s; (e) 2.1 cm/s.

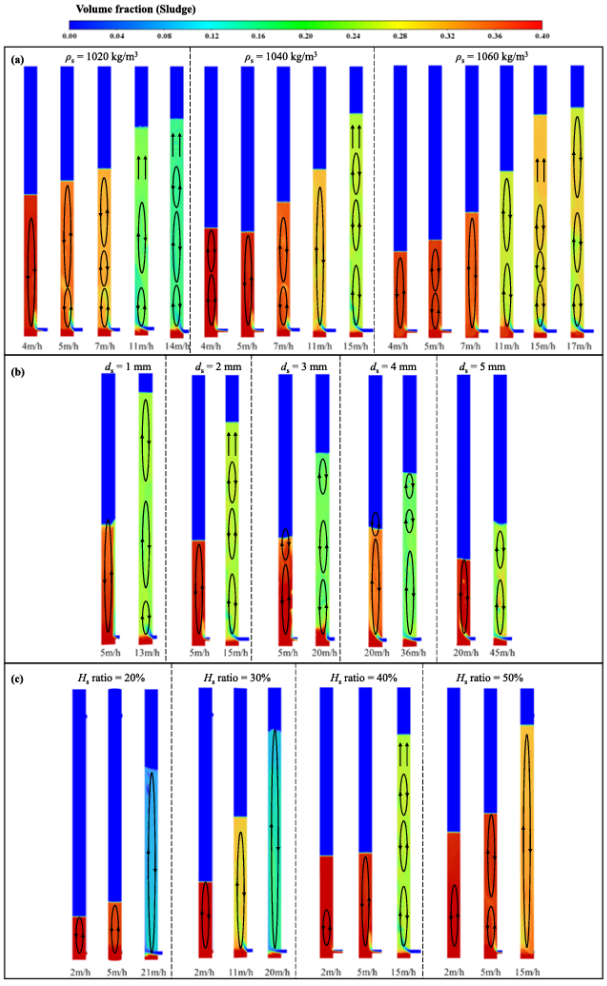


Fig. 3. The hydrodynamic effect of (a) particle sludge; (b) particle sludge diameter (ds); (c) initial sludge height (Hs) on the volume fraction and trace contours (y= 0 vertical profile).

4 Conclusions

This study aimed to develop and optimize a highly integrated Zier reactor by leveraging advanced aeration strategies, treatment performance, and fluidization behavior. Through a combined approach of CFD simulations and experimental validation, the reactor's efficiency in wastewater treatment was systematically investigated. The main findings and conclusions are summarized as follows:

(1) Aeration strategy optimization. The theoretical oxygen supply (ThOS) and theoretical oxygen demand (ThOD) were precisely matched based on influent and effluent characteristics. An appropriate superficial gas velocity (SGV) of 1.3 cm/s is recommended to achieve effective pollutant removal and sludge granulation.

(2) Structural parameter optimization. Reactor geometry predominantly governs the internal flow pattern. The optimal structural configuration of the Zier reactor was identified as a D_A/D_r ratio of 0.5, an H/D ratio of 20, and a D_C/D_A ratio of 0.5, which collectively maximize its treatment and granulation performance.

(3) Influence of sludge particle properties. The physical characteristics of sludge particles significantly affect the hydrodynamic behavior. The results demonstrate that ideal granular sludge properties—specifically, a density (ρ_s) of 1040 kg/m³, a particle size (d_s) of 1–3 mm, and a sludge bed height ratio (H_s) of 40%—optimize treatment efficiency and granulation by establishing multiple CSTR and PFR zones within the reactor.

Reference

[1] D'Bastiani C, Kennedy D, Reynolds A. CFD simulation of anaerobic granular sludge reactors: A review[J]. Water Research, 2023, 242: 120220.

[2] Sadino-Riquelme M C, Donoso-Bravo A, Zorrilla F, et al. Computational fluid dynamics (CFD) modeling applied to biological wastewater treatment systems: An overview of strategies for the kinetics integration[J]. Chemical Engineering Journal, 2023, 466: 143180.

[3] Ranganathan P, Pandey A K, Sirohi R, et al. Recent advances in computational fluid dynamics (CFD) modelling of photobioreactors: Design and applications[J]. Bioresource Technology, 2022, 350: 126920.

[4] Yao Y, Fringer O B, Criddle C S. CFD-accelerated bioreactor optimization: Reducing the hydrodynamic parameter space[J]. Environmental Science: Water Research & Technology, 2022, 8(3): 456-464.

[5] Wei P, Uijttewaal W, Spanjers H, et al. Optimising flow and mixing in a full-scale gas-mixed anaerobic digester by integrating sludge rheological data using computational fluid dynamics[J]. Chemical Engineering Journal, 2023, 468: 143647.

[6] Dabiri S, Kumar P, Rauch W. Integrating biokinetics with computational fluid dynamics for energy performance analysis in anaerobic digestion[J]. Bioresource Technology, 2023, 373: 128728.

[7] Xu Q, Wan Y, Wu Q, et al. An efficient hydrodynamic-biokinetic model for the optimization of operational strategy applied in a full-scale oxidation ditch by CFD integrated with ASM2[J]. Water Research, 2021, 193: 116888.

Long-term Nitrogen Removal Performance of an Anaerobic Ammonia Oxidation Membrane Bioreactor

○ Li-Jun Yin[1], Wei-Kang Qi[1*]

[1]National Engineering Laboratory for Advanced Municipal Wastewater Treatment and Reuse Technology, Engineering Research Center of Beijing, Beijing University of Technology, Beijing 100124, PR China

[*]E-mail: qiweikang10@163.com

Abstract

Anaerobic ammonium oxidation (anammox) has been recognized as a sustainable and energy-efficient biological nitrogen removal process, offering significant advantages over conventional nitrification-denitrification. However, its engineering application is severely constrained by the slow growth rate of anammox bacteria and the lack of long-term operational data for membrane-based configurations.. In this study, an anammox membrane bioreactor (MBR) was operated for 1453 days to investigate long-term nitrogen removal performance and biomass retention. Synthetic wastewater was fed with NH_4^+-N and NO_2^--N at a theoretical stoichiometric ratio of 1:1.32. Results showed that the startup phase (Days 1-60) exhibited substantial fluctuations, with an average TN removal efficiency of merely 8.3%. After prolonged acclimation, the average TN removal efficiency during Days 61-600 progressively improved to 50.3%. Upon entering the high-load phase after Day 600, the system maintained an average removal efficiency of 74.2% despite elevated influent TN concentrations (275.5 mg N/L). Upon shortening HRT to 6 h on Day 825, complete nitrite removal (100% NO_2^--N removal) was achieved and the effluent ammonium concentration dropped to 3.5 mg N/L on Day 843, corresponding to 94.2% ammonium removal; the maximum TN removal efficiency of 88.4% was recorded on Day 791. The membrane module effectively retained anammox biomass, with MLVSS peaking at 5932 mg/L on Day 781. During the extended post-operation phase (Days 871-1453), the average removal efficiency stabilized at approximately 65.0% without process failure. This study provides valuable long-term operational data and practical guidance supporting the engineering application of anammox-MBR technology.

Keywords: Anammox; Membrane bioreactor; Long-term operation; Nitrogen removal; Biomass retention; MBR.

1 Introduction

Conventional biological nitrogen removal processes based on nitrification and denitrification require substantial aeration energy for ammonium oxidation and external organic carbon sources for nitrate reduction, resulting in high operational costs and significant greenhouse gas emissions. Compared to traditional processes, anammox can achieve approximately 60% aeration savings, 100% elimination of external carbon demand, and 80% reduction in excess sludge production [1].

Despite these well-recognized advantages, the widespread engineering implementation of anammox technology faces two major bottlenecks: the extremely slow growth rate of anammox bacteria and their high sensitivity to environmental perturbations. The first full-scale anammox reactor was successfully commissioned in Rotterdam, Netherlands, demonstrating the practical feasibility of this technology [2]. Membrane bioreactors (MBRs), characterized by complete solid-liquid separation and absolute biomass retention capability, have been identified as an ideal reactor configuration for anammox cultivation. Additionally, the high biomass concentration achievable in MBRs enables higher volumetric nitrogen removal rates compared to conventional suspended growth systems.

To date, most studies on anammox-MBR systems have focused on short-term performance evaluation or startup optimization, while long-term operational data extending beyond one year remain scarce. This study presents a comprehensive investigation of an anammox-MBR operated continuously for 1453 days. The specific objectives are: (1) to characterize the long-term nitrogen removal performance evolution across different operational phases; (2) to evaluate biomass accumulation and retention characteristics provided by the membrane module; and (3) to assess the long-term stability and resilience of the system under varying operational conditions.

2 Materials and methods

A laboratory-scale anammox-MBR was constructed and operated at ambient temperature. The reactor was equipped with a hollow fiber membrane module with a nominal pore size of 0.1 micrometer. The reactor was inoculated with anaerobic digester sludge from a municipal wastewater treatment plant. During the entire operational period, the reactor temperature was maintained at 28-30℃, and pH was controlled within the range of 7.8-8.2 through alkalinity adjustment. Mixed liquor was continuously stirred to maintain complete suspension of biomass.

Synthetic wastewater was prepared using $(NH_4)_2SO_4$ and $NaNO_2$ as the sole nitrogen sources, supplemented with trace elements solution. The influent NH_4^+-N and NO_2^--N concentrations were adjusted according to different operational phases, maintaining a theoretical stoichiometric ratio of 1:1.32 as derived from the anammox reaction equation. The hydraulic retention time (HRT) was sequentially set at 12 h (Days 8-163), 24 h (Days 164-498), 12 h again (Days 499-824), and finally shortened to 6 h (Days

825-1453) to investigate the system response to varying loading rates.Table 1 summarizes the operational parameters (HRT, influent TN concentration) and the corresponding four operational phases defined in this study.

Table 1. Summary of operational parameters and nitrogen removal performance across the four operational phases.

Operational phase	Days	HRT (h)	Avg. influent TN (mg N/L)	Avg. TN removal efficiency (%)
Startup	1-60	12	208.8	8.3
Acclimation	61-600	12-24	232.8	50.3
High-load stable	601-870	12-6	275.5	74.2
Extended post-operation	871-1453	6	218.1	65.0

3 Results and discussion

Fig.1 illustrates the long-term nitrogen removal performance over 1453 days of continuous operation. As summarized in Table 1. During the startup phase, the nitrogen removal performance exhibited substantial fluctuations with negative removal values observed at certain points, reflecting the initially low abundance and unstable activity of anammox bacteria. Notably, discernible anammox activity was observed as early as Day 25, with a removal efficiency of 52.0%, indicating rapid initial establishment of the functional consortium despite overall instability.

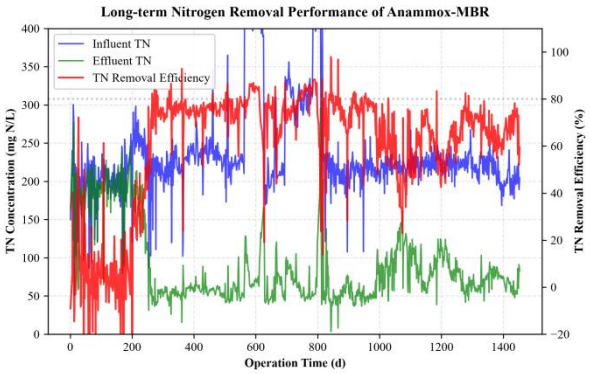


Fig. 1. Long-term nitrogen removal performance of the anammox-MBR system.

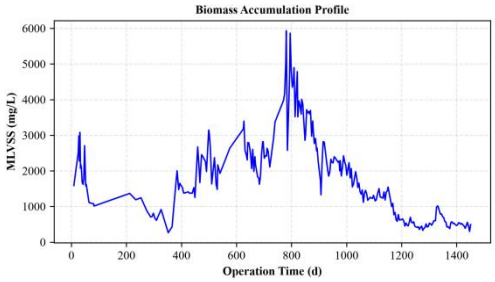


Fig. 2. Biomass accumulation profile (MLVSS) during long-term operation.

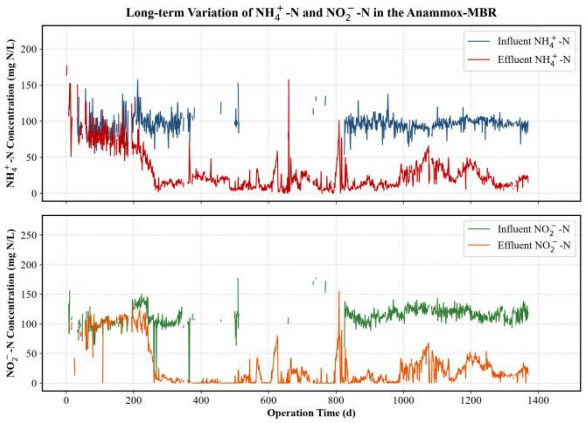


Fig. 3. Long-term variation of influent and effluent NH_4^+-N and NO_2^--N concentrations in the anammox-MBR.

Entering the high-load phase after Day 600, the influent TN concentration was elevated to an average of 275.5 mg N/L, while the system maintained a robust average removal efficiency of 74.2%. MLVSS continued to accumulate, reaching its maximum value of 5932 mg/L on Day 781. This significant biomass accumulation, made possible by the membrane retention, demonstrates the advantage of MBR configuration for anammox cultivation. Fig. 3 presents the long-term variation of influent and effluent NH_4^+-N and NO_2^--N concentrations, showing that effluent nitrite declined rapidly to near-zero levels after Day 600, while effluent ammonium stabilized at low values after the HRT was shortened to 6 h.

4 Conclusions

Based on the above experiments. The main conclusions can be summarized as follows: (1) The membrane module effectively retained the slow-growing anammox consortium, enabling MLVSS accumulation up to 5932 mg/L and facilitating successful reactor startup; (2) Following the startup and acclimation phases, the system achieved complete nitrite removal and an effluent ammonium concentration of 3.5 mg N/L on Day 843 under HRT of 6 h, with a maximum TN removal efficiency of 88.4% recorded on Day 791; (3) The anammox-MBR configuration proved to be technically feasible and robust, maintaining an average TN removal efficiency of 65.0% during the extended post-operation phase without process failure, providing essential empirical data and practical guidance for further engineering scale-up of sustainable anammox-based nitrogen removal technology.

Reference

[1] Yu, D., Zhang, W., Integration of anammox into the MBR process for main stream sewage treatment, AQUA — Water Infrastructure, Ecosystems and Society, 71(1) (2022) 193–210.

[2] Abdul Rahiman, S., Qiblawey, H., Anammox-MBR Technology: Breakthroughs and Challenges in Sustainable Nitrogen Removal from Wastewater, Membranes, 15(11) (2025) 337.

Four kinds of probability papers in flood frequency analysis

○ Toshikazu KITANO[1*]
[1]Department of Civil Engineering, Nagoya Institute of Technology, Nagoya, 466-8555, Japan.
[*]E-mail: kitano@nitech.ac.jp

Abstract

Probability papers help us make a diagnosis for the goodness of fit of the statistical model to the observed data. Log-Pearson type III (LP3) is employed for estimated flood discharge data in US, and various candidate distributions (LN3: three-parameter Lognormal, FT1: Fisher-Tippett type I, or known as Gumbel, GEV: Generalized extreme value, PE3, Pearson type III, ET2: Square root exponential type, proposed by prof. Etou, 1986) in Japan are applied to fit and select. Computer programs for flood frequency analysis can draw the curves of candidate models and data on the Log-Normal probability paper by default in both US and Japan, even though Hydrological Statistics Utility, developed by JICE (https://www.pwri.go.jp/icharm/special_topic/manual_hsu_en.html) has four kinds of probability papers equipped to be chosen. Each probability paper has its pros and cons. They are useful in their own way, and they should be utilized only after properly understanding their specific characteristics. For fair use of probability papers, we propose to give those names after the great pioneers in hydrology in honor of their respective works, and we hope that four kinds of probability papers become friendly to recognize the proper use.

Keywords: Skewness; Return period; Extreme value theories; Tail index; Africa=Greenland paradox.

1 Introduction

Bulletin 17C, a manual for calculating design flood flows for flood protection plan in the United States, introduces the Expected Moments Algorithm (EMA) as a unified method for incorporating historical information (data predating modern systematic records), outliers in the lower tail of the annual maximum flood distribution (low-magnitude floods), and regional characteristics. This represents one of the primary improvements against the previous version Bulletin 17B. The common important thing is that both methods employ the mean, standard deviation, and skewness.

2 Brief history of flood frequency analysis in US

The concept of "maximum flood discharge" was first introduced into flood control planning in the United States by Fuller (1914). Fuller proposed the relation of the maximum flood discharge Q in the periods T and the average flood one Q(Ave.) (= CA^0.8, A is the catchment area) in the form of $Q = Q(\text{Ave.})\ (1 + k \log T)$. Subsequently, Foster (1924) and Hazen (1930) and formalized this approach by defining the curve through the inverse function of a probability distribution, and the return period is defined by the reciprocal of exceedance probability. The probability distribution employed for this purpose was the Pearson Type III (PE3) distribution, because this is asymmetric, the parameter of skewness was introduced to characterize its shape. In this framework, the observed annual maximum flow records were linked to the theoretical distribution using the following parameters: the mean (expected value); the coefficient of variation Cv, defined as the ratio of the population standard deviation to the mean, and the skewness Cs, calculated by normalizing the third central moment (or third cumulant) by the cube of the standard deviation. Cs shows the deviation from the asymmetry of frequency curve, which is one of the important properties of maximum flood discharge, and regarded as a metric reflecting regional characteristics.

In 1967 Bulletin 15, compiled under the direction of the chairman Benson, proposed fitting the logarithms of estimated flow values to PE3. It is the Log-Pearson Type III (LP3) distribution to be applied to discharge data. This line of development eventually led to the subsequent Bulletins 17B and 17C. Fig 1 show an example of annual maximum discharge by Log-Normal plot, which is also demonstrated in Appendix 10 of Bulletin 17C. The order statistics of the data are checked to be placed in the serpentine curve of LP3 with Cs = 0.4 for log10 transformed discharge value. Fig. 2 shows the Normal plot for the original value of the same data. This plot is good to be checked if it is skewed from the Normal distribution, which is a special and limiting form of PE3.

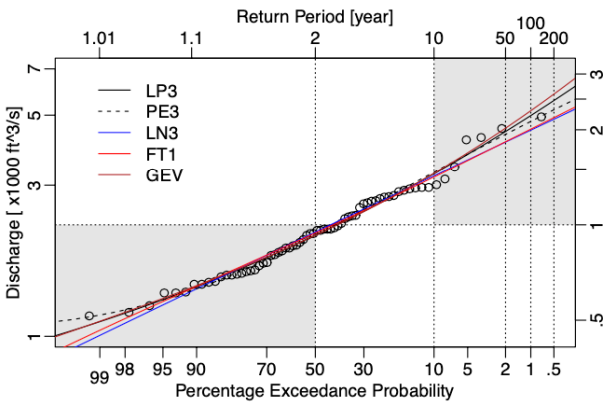


Fig. 1. Log-Normal plot (Hazen probability paper)

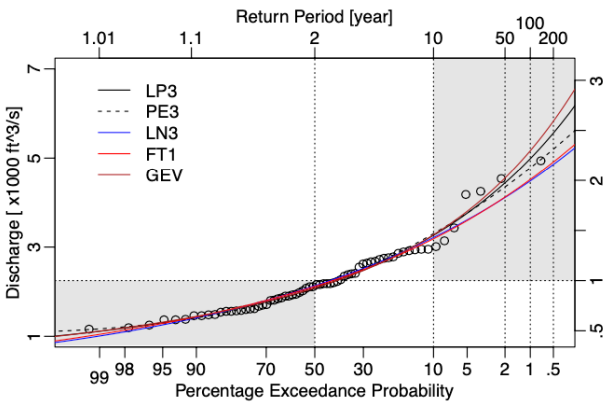


Fig. 2. Normal plot (Foster probability paper)

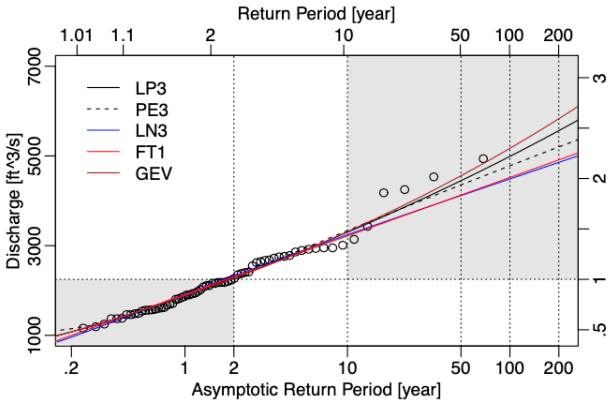


Fig. 3. Return level plot (Powell probability paper)

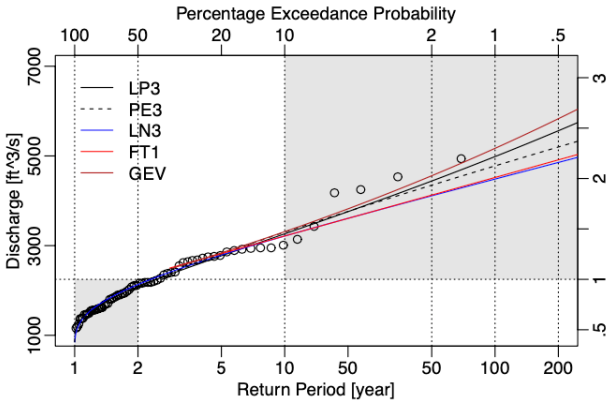


Fig. 4. Return period plot (Chow probability paper)

3 Extreme value theories

Fisher and Tippett (1928) derived the extreme value distribution as the stable distribution for the maximum values over a given period. The main consequence of extreme value theories is the cumulative probability of *n* year maximum value is given asymptotically by

$$F_n(y) = \{F_1(y)\}^n \approx \exp\left\{1 + \xi \frac{y - U(n)}{\sigma(n)}\right\}^{-1/\xi} \quad (1)$$

which is a GEV (Generalized Extreme Value distribution). Gumbel (1954) demonstrated a lot of examples that annual maximum flow data fits the Type I extreme value distribution (FT1, known also as Gumbel distribution). Both PE3 and LN3 (three-parameter lognormal distribution) approach to FT1, that is, GEV with the tail index $\xi = 0$, while LP3 approaches to GEV with $\xi > 0$, which is a decisive difference in the tail properties. Powell (1943) invented a probability paper based on FT1, shown in Fig.3, whose bottom horizontal axis taken by the asymptotic return period T, with the usually used return period T_1, attached to the axis at the top. The relationship of these two return periods is given by

$$F_n = (1 - 1/T_1)^n \approx \exp(-n/T) \quad (2)$$

which is intended as an alternative to the previously used log-normal probability paper to check the skew of distribution.

A joint division committee on floods (1953) acknowledges Gumbel's contributions as a collaborator, while the methods developed by Hazen and Foster continued to be utilized. In 1964, Handbook of Applied Hydrology was published. The editor-in-chief, Chow, described the hydrologic frequency analysis in section 8.1. One of Chow's remarks is the logarithmic tendency of the tail of distribution. Fig.4 is drawn by the log-scale of return period T_1 in the principal horizontal axis, which is related to the exceedance probability $1 - F_1$ in the sub axis at the top in the following:

$$\log T_1 = -\log(1 - F_1) \quad (3)$$

4 Africa=Greenland paradox

In Mercator projection, traditionally used for world maps, Africa, situated near the equator, is depicted as unfairly small while Greenland, located in the far north, appears dis-proportionately large. Africa seems to be the same size as Greenland, though Africa is actually 14 times as large as Greenland. (see Roiter Japan: Non-Mercator projection, Togo located in West Africa submits a resolution to UN, https://www.youtube.com/watch?v=BR9PjLYDb1c). This misunderstanding by the visual bias would be named as Africa=Greenland paradox to draw attention also in the use of probability paper. "How to lie with statistics" by Darrell Huff (1954) is a very famous book that explains the easy ways of misleading by examples. A similar phenomenon of distorted assessment can occur in probability papers. This is a critical perspective, as the phenomenon could be exploited to artificially inflate the apparent goodness-of-fit between observational data and a chosen probability distribution.

5 Discussion and conclusions

The vertical axes of all probability papers Fig.1 to 4 take the amount of discharge in left, and the corresponding multiple of the mean in right, which are graduated on a normal scale, except for Fig. 1 (Log-Normal plot) on a log scale. The bottom horizontal axes of both Fig. 1 and 2 is plotted by the percentage exceedance probability of normal distribution. PE3 is skewed from the normal distribution, depending on the value of the skewness *Cs* (= 2/square root of the shape parameter of PE3). Therefore we should examine how curved the central part (a big picture perspective, say, the range from 10% to 90% of exceedance probability) of the order statistics of the amounts of discharge itself or the log-transformed values are. It is not so good to look hard at the tail part. Especially the right tail, shaded region less than 10% of exceedance probability and bigger than the mean of discharge, is compressed to be unfairly small, while another shaded lower half region less than the mean discharge is disproportionately enlarged. If we focus on the right tail, the probability papers like as Fig. 3 and 4 work usefully.

These four kinds of probability papers should be utilized after properly understanding their specific characteristics. Foster (1924) introduced PE3 with Normal plot, like as Fig. 2, to be applied to the annual maximum discharge data, skewed to the right, and Hazen (1930) employed Log-Normal plot, like as Fig. 1, where the log-transformed discharge data on Normal plot, even though LP3 had not applied as the frequency distribution of the population. The probability paper invented by Powell (1943) is not intended always to be fitted well to FT1 but rather to examine the behavior of the right tail in comparison with the one of FT1. The probability paper like as Fig. 4 enlarges the tail to check the logarithmic tendency pointed out by Chow (1964). We propose to give those names after the great pioneers in hydrology, Hazen, Foster, Powell and Chow to their own probability papers.

For the additional information, the Japanese history in flood frequency analysis can be referred in Takara (2021).

Reference skipped due to space limitations

Drought and Flood Assessment in the Ubolratana Reservoir Basin in Northeastern of Thailand Using Using Coupled Water Balance and Flood Models

○ Weerayuth PRATOOMCHAI[1*]
[1]Department of Civil Engineering, Faculty of Engineering, King Mongkut's University of Technology North Bangkok, Bangkok, Thailand.
[*]E-mail: weerayuth.p@eng.kmutnb.ac.th

Abstract

The Huai Mong, Lam Phaniang and Upper Nam Phong basins in northeastern Thailand experience both drought and flooding. Dry spells interrupt the rainy season every year, and more than 85% of the cultivated area is rain-fed. Sub-district water-balance modelling and coupled one- and two-dimensional flood modelling were used to identify the most affected areas. Water demand is 5,466.6 million m³ per year, of which about 95% is agricultural, against an available supply of 1,595.1 million m³ per year from reservoirs, small water sources and groundwater. The simulated shortage is 147.8 million m³ per year for the main water uses and 867.2 million m³ per year when non-irrigated agriculture is included. The Choen (Part 2), Phrom and Mong sub-basins are the most severely affected, with shortages of 266.3, 211.4 and 124.4 million m³ per year, respectively. The simulated floods of 2006, 2008, 2010 and 2011 covered 1,027–1,228 km², with the largest extent in 2008, and were caused mainly by overbank flow. The results identify priority areas for sub-district drought and flood mitigation plans.

Keywords: Mathematical Models; Rainfed; Water Resources Management; Thailand.

1 Introduction

Drought and flooding are recurrent hazards in the Huai Mong–Lam Phaniang–Upper Nam Phong basin, part of the Nam Phong basin in northeastern Thailand. Dry spells interrupt the rainy season every year and reduce wet-season crop yields. Dry-season water storage is limited relative to the extensive agricultural area, and more than 85% of the cultivated area is rain-fed. Flooding is also frequent: according to the 2019 data on areas at risk of repeated flooding, areas flooded no more than 3 times in the preceding 10 years were mainly in the Lam Phaniang and Upper Nam Phong (Part 2) sub-basins, whereas areas flooded 8–10 times were mainly in the Mong and Phuai sub-basins.

Drought and flood mitigation plans are therefore needed at the sub-district level. This paper applies a sub-district water balance model and a coupled one- and two-dimensional flood model to identify the areas most affected by water shortage and flooding, as a basis for such plans [1].

2 Materials and methods

The study area (14,740 km²) lies in the upper Nam Phong River basin above the Ubolratana Reservoir and comprises nine sub-basins: Mong, Upper Nam Phong (Parts 1–3), Phuai, Lam Phaniang, Phrom and Choen (Parts 1–2) (**Fig.1**). Dry spells were defined as runs of more than 30 consecutive days with daily rainfall of 1 mm or less during June–November using 25 rain gauges over the period 1987–2019. Demand was estimated for agriculture (irrigated and non-irrigated, covering five crop groups), livestock, aquaculture, power generation, industry, domestic use, and ecosystems. Ecosystem demand was set at the flow equalled or exceeded 90% of the time on the monthly flow-duration curve. Supply comprised the mean active storage at the end of the rainy season (November) in large reservoirs (records for 1973–2020) and medium reservoirs (records for 2009–2020), 60% of the storage capacity of small water sources, and groundwater estimated from well records for 1999–2018. Natural runoff was calculated as rainfall minus infiltration and evaporation losses.

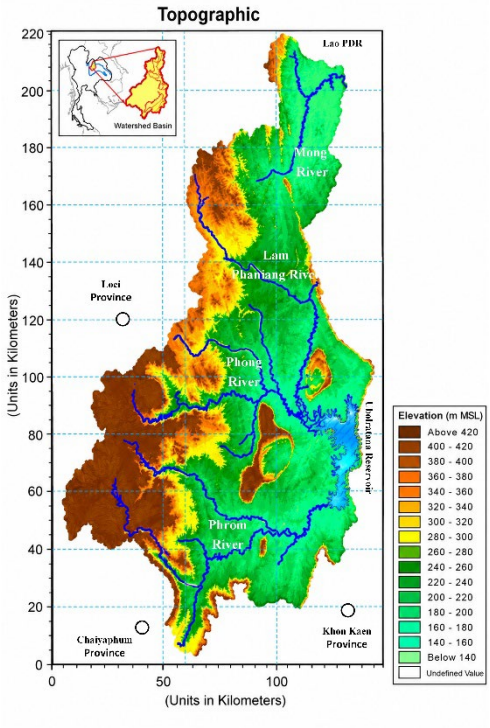


Fig. 1. Study area (Ubolratana reservoir basin)

Water balance was simulated at the sub-district level with MIKE HYDRO BASIN. The model represents the river system as branches and nodes (confluences, water-use points and output locations). Its inputs are sub-basin runoff time

series, reservoir characteristics and operating rules, meteorological time series and sectoral water demands. Runoff was generated for 28 sub-catchments with the rainfall–runoff model, using daily rainfall from 25 rain gauges, spatially averaged with Thiessen polygons, and daily evaporation from six climate stations. The model was calibrated with 2002 data and validated with 2011 data against observed streamflow at seven gauging stations.

Floods were simulated with MIKE FLOOD, which couples a one-dimensional hydrodynamic river model and a two-dimensional floodplain model. The model covers the Phrom, Choen, Upper Nam Phong, Lam Phaniang and Mong Rivers and their tributaries. Floodplain elevations derived from 1:4,000-scale topographic maps with a 2 m contour interval provided by the Land Development Department. Manning's roughness coefficients were calibrated.

3 Results and discussion

Mean annual rainfall over the study area is 1,326.2 mm, of which 74.2% falls in the rainy season (April–November) and 25.8% in the dry season (December–March). September has the highest mean monthly rainfall. Dry spells, as defined above, occurred in every year of the 1987–2019 record, on average 1–2 times per year, and were most frequent at six of the 25 rain gauges: Chum Phae, Ban Thaen, Na Klang, Kaset Sombun, Si Chomphu and Nong Wua-So stations.

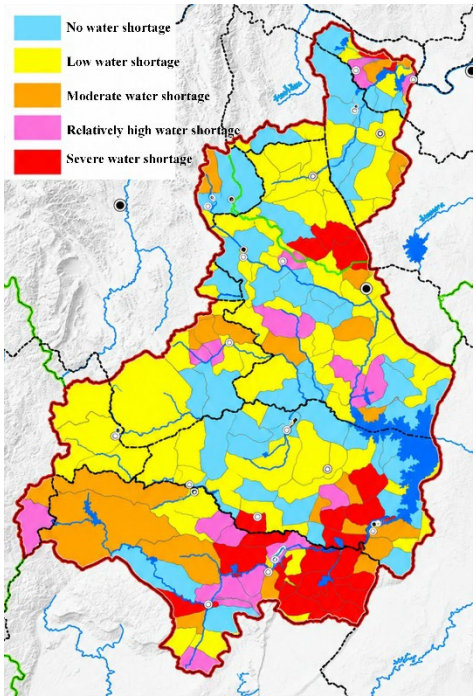


Fig. 2. Sub-district water shortage assessment

Total demand is 5,466.6 million m³ per year, of which about 95% is for agriculture, including about 90% for rainfed agriculture. Available supply (reservoir storage, small water sources and groundwater) is 1,595.1 million m³ per year, about 80% of which is held in the Upper Nam Phong (Part 3) sub-basin.

The total shortage for the main water uses (domestic supply, industry, irrigated agriculture, and livestock) is 147.8 million m³ per year, occurring mainly in the Mong, Choen (Part 1) and Phrom sub-basins (76.2, 66.7 and 22.5 million m³ per year, respectively). Non-irrigated agriculture adds a further 719.4 million m³ per year, about 83% of the total shortage of 867.2 million m³ per year. As shown in **Fig.2**, the most severely affected sub-basins are Choen (Part 2), Phrom and Mong (266.3, 211.4 and 124.4 million m³ per year, respectively), which together account for about 69% of the gross sub-basin deficits (602.1 of 867.8 million m³ per year; the net total of 867.2 million m³ per year is slightly lower because Upper Nam Phong (Part 2) shows a small surplus). Their available supply is small (45.2, 119.2 and 63.3 million m³ per year, respectively) relative to demands of 486.0, 677.1 and 1,248.2 million m³ per year, indicating a pronounced spatial mismatch between supply and demand.

The simulated floods of 2006, 2008, 2010 and 2011 covered 1,027–1,228 km², and the 2008 flood was the largest, at 1,228 km². Most of the flooded area was shallow: 67–74% of it had maximum flood depths below 0.5 m, whereas 8–11% had the depths above 2.0 m. Meanwhile, flood-flow velocities were below 0.5 m/s over at least 98% of the inundated area.

Flooding occurs when heavy rainfall on the surrounding uplands coincides with the arrival of runoff from the hillslopes in the river channels, causing the rivers to overflow their banks and inundate the floodplains. The study show flooding in the Phrom–Choen sub-basins (Kaset Sombun and Phu Khiao districts, Chaiyaphum Province; Chum Phae and Nong Ruea districts, Khon Kaen Province), in the Lam Phaniang sub-basin (Mueang Nong Bua Lamphu, Non Sang and Si Bun Rueang districts, Nong Bua Lamphu Province) and in the Upper Nam Phong (Part 1) sub-basin (Si Chomphu district, Khon Kaen Province).

4 Conclusions

Drought and flooding in the Huai Mong–Lam Phaniang–Upper Nam Phong basin are spatially distinct problems that call for different measures. Under current conditions, the simulated water balance indicates a total shortage of 147.8 million m³ per year for the main water uses and 867.2 million m³ per year when non-irrigated agriculture is included; the latter is concentrated in the Choen (Part 2), Phrom and Mong sub-basins. The simulated floods of 2006, 2008, 2010 and 2011, which covered 1,027–1,228 km², were caused mainly by overbank flow onto floodplains in the Phrom–Choen, Lam Phaniang and Upper Nam Phong (Part 1) sub-basins. These results identify the target areas for sub-district drought and flood mitigation plans. The following measures are proposed:

Domestic water shortage: securing new water sources, improving the storage efficiency of existing projects, and developing groundwater resources.

Agricultural drought: promoting the cultivation of crops with low water requirements, improving the storage efficiency of existing sources.

Flooding: developing or reassessing the operating rule curves of Ubolratana Reservoir to reduce peak flood discharges both for upstream and downstream.

Reference

[1] Office of the National Water Resources, 2021. Draft integrated master plan report for flood and drought mitigation: integrated master plan study for the Huai Mong–Lam Phaniang and Upper Nam Phong basin (in Thai).

Dynamic urban pluvial flood emulation with SegFormer: Input design and diagnostic evaluation

○ Hyuna WOO[1*], Bomi KIM[1] & Seong Jin NOH[1]
[1]Department of Civil Engineering, Kumoh National Institute of Technology, Gumi 39177, Republic of Korea.
[*]E-mail: hwoo@kumoh.ac.kr

Abstract

Deep-learning emulators offer a fast alternative to computationally demanding hydrodynamic simulations for urban pluvial flooding. However, overall performance metrics may overlook differences in accuracy over the course of a flood event and across the inundated area. This study develops a SegFormer-based emulator that predicts flood-depth maps from rainfall history, elevation and land-use information. The model was evaluated against 10 m hydrodynamic simulations of three historical events in Gunsan, South Korea, and compared with U-Net and 1D-CNN benchmarks. Alongside conventional metrics, prediction accuracy was examined across flood phases, inundation depths and flood boundaries. The proposed model achieved the highest CSI (0.947) among the three models. Accuracy was lower during the rising phase, depth errors generally increased with inundation depth, and models with relatively similar overall scores differed substantially in boundary accuracy. A 48 h flood sequence was emulated in approximately 5 s on a GPU. These findings demonstrate the value of examining temporal and spatial performance alongside overall metrics.

Keywords: urban pluvial flooding; deep learning; SegFormer; flood emulation; model evaluation.

1 Introduction

Urban pluvial flooding can develop rapidly during intense rainfall, particularly in densely built areas where runoff accumulates over short periods. Timely estimates of inundation extent and depth support flood risk management and emergency response [1]. Hydrodynamic models can represent these processes in detail, but repeated high-resolution simulations are computationally demanding, particularly when many rainfall conditions must be considered. Deep-learning emulators have therefore been explored as efficient alternatives for reproducing simulated flood behaviour [2, 3].

Model performance is commonly reported using overall measures such as the critical success index (CSI) and root mean square error (RMSE). These measures are useful for comparison, but similar scores do not necessarily indicate that two models reproduce flood evolution or spatial inundation patterns equally well. In particular, errors can vary between the rising and recession phases, between shallow and deep inundation, and at the margins of the inundated area.

This study develops an emulator based on SegFormer [4] for urban pluvial flooding and compares it with U-Net [5] and 1D-CNN benchmarks. Alongside overall scores, temporal and spatial prediction characteristics are examined by flood phase, inundation depth and boundary location.

2 Materials and methods

The study area covers approximately 12.6 km² of the urban Gyeongpocheon watershed in Gunsan, South Korea. Reference inundation maps were generated using the H12 hydrodynamic model [6, 7] on a 10 m grid at 10 min intervals for 48 h events. Ninety synthetic rainfall events covering a wide range of rainfall totals, durations and temporal patterns were used for training and validation. Three historical rainfall events from 2022, 2023 and 2024, which were not included in training, were used for independent testing.

The proposed emulator combines a SegFormer-based spatial encoder [4] with a module that processes rainfall history. Elevation and land-use maps provide spatial information, while recent and accumulated rainfall describe storm evolution. The two sources of information are combined to predict inundation extent and depth at each time step, without relying on previously predicted flood maps. For comparison, a U-Net [5] using the same spatial inputs and a rainfall-only 1D-CNN [3] were evaluated as benchmark models.

Inundation extent was evaluated using CSI, probability of detection (POD) and false alarm ratio (FAR) at a 10 cm depth threshold, while depth accuracy was assessed using RMSE. The overall metrics were complemented by analyses across flood phases, reference inundation-depth ranges and inundation boundaries. Flood phases were identified from rainfall and changes in reference inundation volume. Boundary accuracy was assessed from the separation between predicted and reference inundation margins, considering both additional inundated areas and missed areas. Together, these analyses describe aspects of performance that may not be apparent from overall scores.

3 Results and discussion

All three emulators showed high aggregate inundation-extent skill, with event-averaged CSI values ranging from 0.909 to 0.947 and domain-wide RMSE values from 0.73 to 1.50 cm (Table 1). The proposed model achieved the highest CSI and lowest RMSE, although its CSI exceeded those of the benchmarks by only a few hundredths. These relatively small differences in overall performance nevertheless masked differences in where and when the models erred, as revealed by the analyses of inundation boundaries, flood phases and depth ranges.

Table 1. Performance averaged over the three historical events (RMSE: cm; Bd.: mean predicted-to-reference boundary displacement, m; Time: s per 48 h event).

Model	CSI	POD	FAR	RMSE	Bd.	Time
Proposed	0.947	0.966	0.020	0.73	0.65	5.1
U-Net	0.913	0.949	0.039	0.96	1.13	2.3
1D-CNN	0.909	0.958	0.054	1.50	2.32	0.64

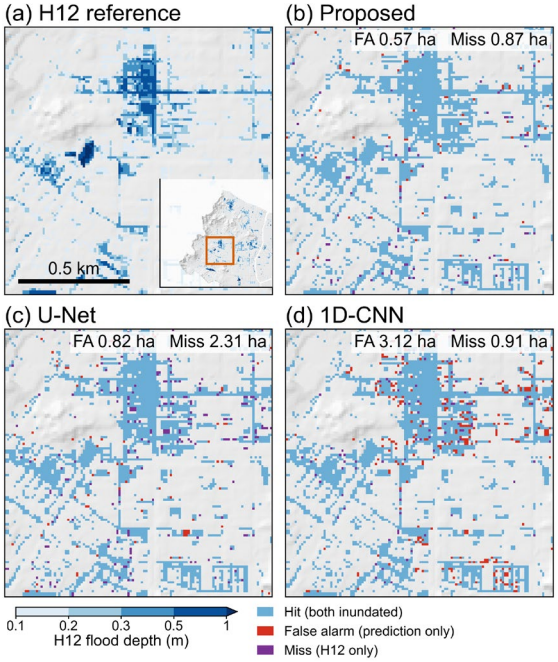


Fig. 1. Spatial comparison during the rising phase of the 2024 event (9 July, 23:30). (a) H12 reference flood depth, with the study subarea shown in the inset. (b–d) Correctly predicted inundation, false alarms (FA) and misses at the 10 cm threshold, with areas given in each panel.

The clearest differences emerged in inundation boundary prediction. The proposed model and the 1D-CNN differed in CSI by only 0.038, yet their mean predicted-to-reference boundary displacements were 0.65 m and 2.32 m, respectively, a 3.6-fold difference. Most of the proposed model's boundary cells coincided with the reference boundary or lay within one 10 m grid cell, whereas the 1D-CNN showed larger boundary errors during certain stages of the events. Measured in the reverse direction, from the reference boundary to the nearest predicted boundary, displacement was largest for the U-Net, indicating missed inundated areas. Together, these directional measures revealed different spatial error patterns: more false alarms for the 1D-CNN and more missed inundation for the U-Net. These patterns were not fully reflected in CSI alone and are illustrated for the rising phase of the 2024 event in Fig. 1.

Accuracy varied over the course of each event in ways that event-averaged scores did not fully capture. Inundation-extent accuracy was lowest during the rising phase for all three models and higher near the peak and during recession. During the rising phase, predicted inundation volume tended to lag the reference by tens of minutes, while false alarms and boundary errors were generally more pronounced, particularly for the rainfall-only 1D-CNN. Depth errors followed a different pattern from categorical scores: even when CSI values converged during recession, depth accuracy still differed among the models.

Depth errors generally increased with reference inundation depth. Areas with reference depths exceeding 1 m were almost always identified as inundated at the 10 cm threshold, but their depths tended to be underestimated, particularly during the rising phase. Thus, correctly detecting deep inundation did not necessarily imply an accurate estimate of its depth. Analysis across depth ranges provides information complementary to extent-based metrics, particularly for deeper flooding.

The proposed model generated a 48 h flood-depth sequence in 5.1 s on a GPU, compared with approximately 23 min for H12 on a multicore CPU. These runtimes were measured using different hardware and should not be interpreted as a hardware-normalised speed-up. Furthermore, performance was assessed against simulated flood depths for three historical events in a single catchment, rather than against field observations.

4 Conclusions

A SegFormer-based emulator was developed for urban pluvial flooding and generated a 48 h flood-depth sequence in approximately 5 s on a GPU. Although it achieved the highest overall scores among the three models, the margins were small, and the evaluation showed that these scores did not convey where and when the models erred. Models that differed in CSI by less than 0.04 differed more than threefold in boundary displacement, accuracy was lowest during the rising phase, and deep inundation was detected but underestimated. Considering temporal and spatial prediction characteristics alongside conventional metrics therefore provides a more complete basis for assessing flood emulators.

References

[1] K. Guo, M. Guan, D. Yu, Urban surface water flood modelling – a comprehensive review of current models and future challenges, Hydrol. Earth Syst. Sci. 25 (2021) 2843–2860.

[2] S. Kabir, S. Patidar, X. Xia, et al., A deep convolutional neural network model for rapid prediction of fluvial flood inundation, J. Hydrol. 590 (2020) 125481.

[3] H. Woo, H. Choi, M. Kim, S.J. Noh, Physics-guided deep learning for spatiotemporal evolution of urban pluvial flooding, Water 17 (2025) 1239.

[4] E. Xie, W. Wang, Z. Yu, et al., SegFormer: Simple and efficient design for semantic segmentation with transformers, Adv. Neural Inf. Process. Syst. 34 (2021).

[5] O. Ronneberger, P. Fischer, T. Brox, U-Net: Convolutional networks for biomedical image segmentation, MICCAI 2015, LNCS 9351 (2015) 234–241.

[6] S.J. Noh, J.-H. Lee, S. Lee, et al., Hyper-resolution 1D-2D urban flood modelling using LiDAR data and hybrid parallelization, Environ. Model. Softw. 103 (2018) 131–145.

[7] B. Kim, H. Ryu, S. Lee, et al., Portable multi-GPU urban flood modelling via MPI-OpenACC: evaluating acceleration, scaling, and workload-per-GPU, Environ. Model. Softw. 200 (2026) 106957.

[8] H. Woo, B. Kim, S.J. Noh, Dynamic urban pluvial flood emulation with SegFormer: Input design and diagnostic evaluation (under review).

Reservoir regulation and scale-dependent flood amplification under warming climates: a WRF-Hydro storyline of Typhoon Hinnamnor in the Nakdonggang basin

Yaewon LEE[1*], Bomi KIM[1] & Seong Jin NOH[1]
[1]Department of Civil Engineering, Kumoh National Institute of Technology, Gumi 39177, Republic of Korea.
[*]E-mail: yaewon99@kumoh.ac.kr

Abstract

Anthropogenic warming is expected to intensify tropical-cyclone rainfall, while recent storyline simulations suggest that the resulting increase in flood peaks may be greatest in low-order headwater reaches. However, how reservoirs modify this scale-dependent response during an individual flood event remains unclear. This study extends a WRF-forced WRF-Hydro pseudo-global-warming (PGW) storyline of Typhoon Hinnamnor (2022) over the Nakdonggang basin, South Korea, by representing four large multipurpose dams using level-pool routing. For four sea surface temperature (SST) states, paired simulations with and without reservoir routing are designed to evaluate reservoir effects across 312 river reaches. In the unregulated baseline, basin-mean runoff increased by 24–49% under future SST states. Under SST-2090, the median peak-flow increase reached 71.6% in first- and second-order reaches, compared with 44.9% across third- and fourth-order reaches. Since the dams control about 20% of the study area and most headwater reaches lie upstream of the reservoirs, we hypothesize that reservoir routing will primarily attenuate warming-induced peak-flow increases downstream of the dams, while much of the headwater amplification will remain. The paired simulations will quantify how this attenuation varies along the river network.
Keywords: WRF-Hydro; Pseudo-global warming; Tropical cyclone; Reservoir routing; Flood attenuation; Stream order.

1 Introduction

Anthropogenic warming is expected to intensify tropical-cyclone rainfall, and large-sample projections indicate that the relative increase in extreme streamflow tends to be largest in small catchments and to exceed the increase in rainfall [1]. Convection-permitting simulations combined with the pseudo-global-warming (PGW) storyline approach allow a historical storm such as Typhoon Hinnamnor (September 2022), which brought record rainfall to southeastern Korea, to be re-simulated under alternative climate states [2]. A WRF-forced WRF-Hydro storyline of Hinnamnor indicated that the warming-induced increase in peak flow was concentrated in low-order headwater reaches rather than on the main stem [3].

Many large rivers, however, are regulated by dams. Global assessments suggest that dams can substantially reduce the population exposed to future flooding [4], and for Korean multipurpose dams, multi-model projections indicate increases in released flood volume of more than 70% by the end of the century [5]. Their flood-mitigation capacity has been shown to depend on antecedent storage as well as on rainfall [6], and analytical studies indicate that the peak reduction at a downstream section is largely determined by the share of the upstream area that the reservoir controls [7]. However, how a single warming-intensified flood is modified by a set of dams along a river network has received little attention.

This study examines how the four multipurpose dams of the Nakdonggang basin modify the warming-induced increase in peak flow along the river network, by re-simulating Hinnamnor under four PGW sea surface temperature (SST) states with and without reservoir routing in WRF-Hydro. Here, the modelling framework, the unregulated baseline [3] and the hypotheses to be tested are presented.

2 Materials and methods

2.1 Study area, PGW storyline forcing and WRF-Hydro

The study basin (29,220 km^2) comprises the Nakdonggang basin and the adjacent coastal basins in southeastern Korea, where four large multipurpose dams (Andong, Imha, Hapcheon and Namgang) regulate the upper tributaries and together control about 20% of the basin. Typhoon Hinnamnor was re-simulated with a convection-permitting WRF configuration, and the PGW perturbation was applied to SST using the CMIP6 multi-model mean change under SSP2-4.5 [2], giving four SST states: SST-1860, SST-Current, SST-2050 and SST-2090. The WRF output drives WRF-Hydro [8] by one-way coupling on a 500 m grid with reach-based channel routing. The channel network comprises 312 reaches of Strahler order 1–4, of which orders 1–2 are referred to as headwater reaches and order 4 as the main stem. The model setup and calibration follow the earlier storyline study [3].

2.2 Reservoir representation and experimental design

The four dams are represented by the built-in level-pool scheme of WRF-Hydro, in which outflow is computed from pool elevation through weir and orifice discharge. Because explicit dam-operation rules are not included, the simulated attenuation represents the effect of idealized reservoir routing rather than actual operational flood mitigation. Two configurations, with reservoir routing (Res) and without (NoRes), are run under each SST state with identical forcing, parameters and initial states, so that the difference between them can be attributed to reservoir routing. The warming signal is defined as the change in peak flow relative to SST-

Current of the same configuration and is summarised by stream order; the effect of regulation is evaluated as the fraction of the warming-induced increase removed below the dams.

3 Results and discussion

3.1 Baseline: warming response without reservoirs

In the unregulated storyline [3], basin-mean rainfall increased by 26% and 36% under SST-2050 and SST-2090 relative to SST-Current, whereas runoff increased by 24% and 49%, so that the runoff ratio was higher under the warmest state (Table 1). At the reach scale (Fig. 1), the future states broadened the distribution of increases, with 37% and 43% of reaches exceeding +100% under SST-2050 and SST-2090, and the largest increases tended to appear in the upstream, low-order parts of the network. By stream-order group (Table 2), median peak-flow increases under SST-2050 were similar for first- and second-order reaches (52.7%) and third- and fourth-order reaches (51.0%). Under SST-2090, the corresponding increases were 71.6% and 44.9%, respectively. These results suggest that stronger warming may concentrate flood amplification in small headwater catchments [3].

Table 1 Basin-mean rainfall, runoff and runoff ratio (%), and changes relative to SST-Current [3].

SST state	1860	Current	2050	2090
Rainfall (mm)	101.5	106.8	135.0	144.7
Runoff (mm)	33.6	37.0	45.7	55.1
Runoff ratio	33.1	34.6	33.9	38.1
ΔRainfall (%)	−5.0	–	+26.4	+35.5
ΔRunoff (%)	−9.2	–	+23.5	+48.9

Table 2 Median and mean peak-flow change (%) relative to SST-Current by stream order [3].

Statistic, order	1860	2050	2090
Median, orders 1–2	−4.6	52.7	71.6
Median, orders 3–4	−10.1	51.0	44.9
Mean, order 1	2.6	236.1	534.6
Mean, order 2	−3.5	262.2	732.3
Mean, order 3	−9.4	192.6	282.0
Mean, order 4	−6.4	81.6	203.2

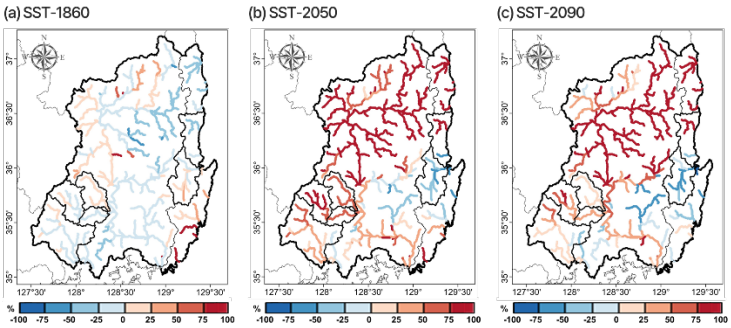


Fig. 1. Reach-scale change in peak flow (%) relative to SST-Current under (a) 1860, (b) 2050 and (c) 2090 [3].

3.2 Expected role of reservoir regulation

Based on network topology and attenuation theory [7], three outcomes are anticipated. First, headwater amplification is likely to remain largely unaffected by reservoir routing, because about three quarters of the headwater reaches lie upstream of the reservoirs. Second, reservoir routing is expected to attenuate warming-induced peak-flow increases immediately downstream of the dams. Third, the fraction of the warming-induced increase attenuated by reservoir routing is expected to decrease along the main stem as unregulated tributaries join the regulated flow.

4 Conclusions

In the unregulated baseline, the median peak-flow increase under SST-2090 was 71.6% in first- and second-order reaches, compared with 44.9% across third- and fourth-order reaches [3]. Since most headwater reaches lie upstream of the reservoirs, much of this amplification may occur beyond the direct influence of the four dams. The paired simulations will assess how reservoir routing modifies the spatial pattern of warming-induced peak-flow increases along the river network.

Reference

[1] M. Faghih, F. Brissette, Temporal and spatial amplification of extreme rainfall and extreme floods in a warmer climate, J. Hydrometeorol., 24 (2023) 1331-1343.

[2] Y. Hiraga, et al., Impacts of climate change on tropical cyclones and associated rainfall over South Korea: storyline and risk-based approaches, Atmos. Res., 331 (2025) 108685.

[3] Y. Lee, et al., Scale-dependent flood hazard amplification under warming climates: a tropical cyclone Hinnamnor storyline in South Korea, Geosci. Lett., 13 (2026) 56.

[4] J. Boulange, et al., Role of dams in reducing global flood exposure under climate change, Nat. Commun., 12 (2021) 417.

[5] S.J. Noh, et al., Climate change impact assessment on water resources management using a combined multi-model approach in South Korea, J. Hydrol. Reg. Stud., 53 (2024) 101842.

[6] U. Vegad, V. Mishra, Climate change and effectiveness of dams in flood mitigation in India, npj Nat. Hazards, 2 (2025) 63.

[7] E. Volpi, et al., Reservoir effects on flood peak discharge at the catchment scale, Water Resour. Res., 54 (2018) 9623-9636.

[8] D.J. Gochis, et al., WRF-Hydro Modeling System Technical Description v5.4, NCAR (2025).

Precipitation-type classification and deep-learning super-resolution of Radar-AMEDAS rainfall

○ Hyeonjin CHOI[1*], Yusuke HIRAGA[2] & Seong Jin NOH[3]
[1]Climate and Environmental Research Institute, Korea Institute of Science and Technology (KIST), Seoul 02792, Republic of Korea.
[2]Department of Civil and Environmental Engineering, Graduate School of Engineering, Tohoku University, Sendai 980-8579, Japan.
[3]School of Architecture, Civil and Environmental Engineering, Kumoh National Institute of Technology, Gumi 39177, Republic of Korea.
[*]E-mail: hjchoi@kist.re.kr, hyeonjinchoi21@gmail.com

Abstract

Kilometre-scale, hourly precipitation is essential for assessing localized heavy rainfall and urban floods, and deep-learning super-resolution (SR) has emerged as an efficient way to recover such detail from coarse precipitation fields. However, SR skill has been reported only as domain-wide scores that do not distinguish convective from stratiform rainfall, although the two differ fundamentally in spatial structure; this study therefore develops a convective/stratiform classifier for Radar-AMEDAS rainfall and evaluates SR performance separately for each type. Because Radar-AMEDAS, the 1-km radar–rain-gauge analysed precipitation of the Japan Meteorological Agency, contains no vertical reflectivity information, conventional radar-based classification cannot be applied. We therefore developed a random-forest model, trained on rain-type labels of the GPM Dual-frequency Precipitation Radar (DPR), that estimates the convective fraction of each rainfall patch from 13 rain-rate texture features, and used it to select confidently classified patches. Using about 2.2 million classified patches over Kyushu, ResUNet and WGAN models were trained to reconstruct 1-km fields from 10-km inputs. Preliminary results on 2021–2025 test data show that ResUNet reduced the RMSE of bicubic interpolation by 17–18% for both types. For convective rain, the WGAN performed best at moderate intensity (CSI at 10 mm h^{-1}: 0.47 vs. 0.34 for bicubic) but tended to show lower skill for the most intense rainfall (CSI at 30 mm h^{-1}: 0.43 vs. 0.49), which was not observed for stratiform rain. Type-specific and unified training gave similar results. These findings suggest that type-resolved evaluation can reveal differences in SR behaviour that domain-wide scores do not show.

Keywords: precipitation super-resolution; Radar-AMEDAS; convective/stratiform classification; GPM DPR; deep learning.

1 Introduction

Localized heavy rainfall in Japan is often produced by quasi-stationary convective bands (senjo-kousuitai) only 20–50 km wide [1], so flood assessment requires kilometre-scale, hourly precipitation. Climate projections such as the 20-km regional ensemble of d4PDF cannot resolve such systems and do not reproduce the observed distribution of local hourly precipitation [2].

Deep-learning SR offers an efficient alternative. A recent intercomparison showed that deterministic networks smooth fine-scale variability and suppress extremes, whereas generative adversarial networks (GANs) add realistic small-scale structure and better reproduce the heavy tail [3]. These models are usually evaluated with scores aggregated over all samples.

Such scores can hide differences between precipitation types. Convective rainfall consists of small, intense cells, whereas stratiform rainfall is widespread and smooth [4], so the information lost by coarsening should differ between them; yet, to our knowledge, SR skill has not been evaluated separately for the two types. One obstacle is that standard classification relies on reflectivity structure from ground or spaceborne radars [4,5], which gauge-adjusted rainfall products such as Radar-AMEDAS do not contain. This study (i) develops a GPM DPR-guided convective/stratiform classifier for Radar-AMEDAS rainfall and (ii) evaluates deterministic and adversarial SR models separately for each type.

2 Materials and methods

Data and classifier. Radar-AMEDAS analyses for June–November 2014–2025 over Kyushu (31–34°N, 129–132°E) were divided into 64 × 64-pixel patches (stride 32). DPR rain-type flags (2A.DPR V07 [5]) with near-surface rain rate ≥0.5 mm h^{-1} were collocated with the patches within ±25 min and 0.25°, giving 116,576 pixels in 8,658 patches on 543 days. Because a patch often contains both types, the target was the convective fraction of the matched pixels. A random-forest regressor used 13 features describing intensity (e.g., maximum, coefficient of variation), cell structure and Steiner-type background excess [4] for the whole patch and its central 16 × 16 pixels, and was validated by 5-fold cross-validation grouped by date to avoid temporal autocorrelation.

SR experiments. Only confidently classified patches, with predicted convective fraction ≥0.6 (convective) or ≤0.4 (stratiform), were used. High-resolution targets (60 × 60 pixels) were block-averaged to 6 × 6 inputs (×10). Data from 2014–2020 were used for training and 2021–2025 for testing (88,450 convective and 128,051 stratiform test patches). A residual U-Net (ResUNet) trained with a rain-weighted MAE and a WGAN sharing the same generator were trained for

each type (-T) and for both types (-U), and compared with bicubic interpolation using SSIM, RMSE and the pixel-pooled critical success index (CSI).

3 Results and discussion

Classifier. The DPR-trained regressor ranked patches consistently with the DPR convective fraction on independent dates (Spearman ρ = 0.64), and Steiner-type background-excess features further improved the classification. Typical cases show compact, intense convective cells that bicubic interpolation smears out, and broad, smooth stratiform fields (Fig. 1).

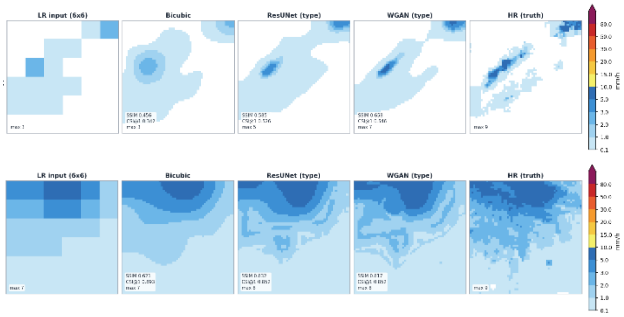


Fig. 1. Typical convective (top) and stratiform (bottom) test cases. From left: LR input, bicubic, ResUNet-T, WGAN-T and reference (mm h⁻¹); panel values are SSIM, CSI at 1 mm h⁻¹ and maximum.

Table 1 Test scores (2021–2025) for convective (C) and stratiform (S) patches. BI: bicubic; RU/WG: ResUNet/WGAN; -T: type-specific; -U: unified. RMSE in mm h⁻¹; CSI30: pooled CSI at 30 mm h⁻¹. Best in bold.

	BI	RU-T	WG-T	RU-U	WG-U
SSIM (C)	0.734	0.739	**0.807**	0.769	0.797
SSIM (S)	0.696	**0.740**	0.720	0.733	0.737
RMSE (C)	1.030	**0.854**	1.011	0.884	1.252
RMSE (S)	0.782	0.639	0.712	**0.637**	0.934
CSI30 (C)	0.488	0.544	0.428	**0.554**	0.302
CSI30 (S)	0.438	**0.583**	0.569	0.576	0.421

SR performance. ResUNet reduced RMSE by 17–18% for both types (Table 1). For convective rain, the WGAN produced the most realistic structure (SSIM 0.81) and the highest CSI at 10 mm h⁻¹ (0.47 vs. 0.34 for bicubic), but its CSI at 30 mm h⁻¹ tended to be lower than that of bicubic interpolation (0.43 vs. 0.49), whereas ResUNet raised it to 0.54. When a 4-pixel neighbourhood was allowed, the WGAN skill at 10 mm h⁻¹ was close to that of ResUNet (FSS 0.82 for both vs. 0.67 for bicubic), suggesting that its intense cells are slightly displaced and thus penalised twice by point-wise scores. For stratiform rain, both type-specific networks improved heavy-rain CSI (0.57–0.58 vs. 0.44). Type-specific and unified training gave similar results.

4 Conclusions

A GPM DPR-guided classifier enabled type-resolved SR evaluation for Radar-AMEDAS rainfall, which lacks reflectivity information. Preliminary results suggest that SR behaviour differs between types: an adversarial model with the highest structural similarity tended to show lower skill for the most intense convective rainfall, whereas a deterministic ResUNet improved most scores for both types. Type-resolved evaluation may therefore help in evaluating and selecting SR models, particularly for flood applications. Future work will refine the classifier, separate type and intensity effects and apply the framework to d4PDF.

Acknowledgements. Radar-AMEDAS and GPM DPR data were provided by JMA and NASA/JAXA, respectively.

References

[1] T. Kato, Quasi-stationary band-shaped precipitation systems, named "senjo-kousuitai", causing localized heavy rainfall in Japan, J. Meteor. Soc. Japan, 98 (2020) 485-509.
[2] T. Yoshikane, K. Yoshimura, A downscaling and bias correction method for climate model ensemble simulations of local-scale hourly precipitation, Sci. Rep., 13 (2023) 9412.
[3] S. Singh et al., Comprehensive inter-comparison of generative AI models for super-resolution precipitation downscaling across hydroclimatic regimes, Geosci. Model Dev., 19 (2026) 7545-7567.
[4] M. Steiner, R.A. Houze Jr., S.E. Yuter, Climatological characterization of three-dimensional storm structure from operational radar and rain gauge data, J. Appl. Meteorol., 34 (1995) 1978-2007.
[5] J. Awaka et al., Rain type classification algorithm module for GPM Dual-frequency Precipitation Radar, J. Atmos. Oceanic Technol., 33 (2016) 1887-1898.

Development of a Dynamic Flood Evacuation Model and Evacuation Strategies

○ Tzu-Hsien YU[1]*, Tsun-Hua YANG[1] & Kay-Yen CHIEN[1]

[1] Department of Civil Engineering, National Yang Ming Chiao Tung University, Hsinchu 300093, Taiwan.

*E-mail: yzx03625@gmail.com.

Abstract

Climate change is making extreme rainfall and sudden floods increasingly frequent, causing widespread impacts on communities and infrastructure. The evacuation of residents during emergencies is often undesirable but necessary to protect lives. Historical disaster events have shown that unexpected casualties can occur due to disruptions or failures in the evacuation process, whether because of delayed or inappropriate evacuation decisions or the selection of unsafe evacuation routes. Evacuation outcomes depend on the flood depth and velocity that residents encounter at their locations and along their routes, as well as on differences in mobility in floodwater among people of different ages and genders. Timely and effective evacuation is key to reducing casualties, yet how these factors jointly affect evacuation outcomes remains to be explored. This study drives an agent-based model (ABM) with flood inundation simulations to examine how flooding affects individual behavior and, in turn, overall evacuation. The model adopts the Belief-Desire-Intention (BDI) architecture: a flood model provides water depth at each time step (flow velocity is unavailable and set to zero); each agent updates its beliefs only according to the flooding it perceives, forms its risk perception from hazard, social, and neighbor information to decide when to evacuate, and adjusts its walking speed and evacuation route accordingly. Guangfu Township, Hualien, which was severely affected by the 2025 Matai'an landslide dam overflow, is used as the case study. Preliminary simulations with a representative population compare evacuation outcomes across age groups and villages. The framework developed in this study can provide a reference for township-scale flood evacuation assessment and emergency management decision-making.

Keywords: Agent-based modelling (ABM); Belief-Desire-Intention (BDI); Risk perception; Evacuation behavior; Flood evacuation.

1 Introduction

Flood evacuation success depends not only on the flood itself but also on when residents decide to act and whether they can move safely through floodwater. Regarding evacuation decisions, previous studies indicate that residents' willingness or risk perception to evacuate is influenced by socioeconomic characteristics, hazard information, social networks, and neighbors' behavior, and that risk perception is updated progressively as information arrives [1]. The Belief-Desire-Intention (BDI) architecture formalizes human reasoning: beliefs represent an agent's knowledge of its environment, desires are the goals it wants to achieve, and intentions are the actions it selects and carries out [2]. This architecture suits situations in which residents judge from local, incomplete information and adjust their actions as conditions change. This study develops an agent-based model (ABM) built on the BDI architecture: each agent updates its beliefs from the flooding it perceives, forms a risk perception that determines whether to evacuate, and adjusts its walking and route in floodwater. The authors aim to integrate residents' risk perceptions and actual movement patterns into a unified framework to simulate disaster evacuation behavior.

2 Materials and methods

2.1 Study area and data.

On 23 September 2025, the Matai'an Creek landslide dam overflowed and floodwater entered Guangfu's urban area in Hualien, Taiwan, causing severe casualties, many of them residents who could not evacuate in time. Flood depths for the Matai'an landslide dam overflow event were simulated with a cellular automata inundation model, provided as 20 m raster grids at 5-min intervals. The present study focuses on the effects of flood depth on evacuation behavior. Therefore, flow velocity is not considered in the current analysis but will be incorporated in future research. Population data are official village-level household registration statistics (single year of age and gender) from the Ministry of the Interior for September 2025 [3]. For the baseline simulation, all 5,933 residents are synthetically allocated to real, geocoded household-registry address points while preserving each village's age and gender totals; addresses are snapped to the nearest road segment, and each multi-person household is assigned at least one adult. For the sensitivity analysis, 1,000 agents are instead sampled in proportion to village, age, and gender; children under 10 are assumed to evacuate with adults. Education, income, and household size are taken from village-level statistics; the number of household members with disabilities is estimated from the Hualien County rate; body height is sampled by age and gender from Taiwanese anthropometric statistics.

2.2 Evacuation decision and risk perception.

Each agent's evacuation tendency π is computed by a binary logit model of gender, age ≥65, education, income,

household size, and the numbers of household members aged ≥75 and with disabilities, estimated from a post-flood evacuation survey in Taiwan (SRDA D00225; N = 913 complete cases). π is converted to a personal risk tolerance τ by the equal-interval rule of Roy et al. [1]. Risk perception RP integrates three information sources:

$$I_{new} = \alpha_H I_H + \beta_S I_S + \gamma_N I_N \quad (1)$$

$$RP_t = (1 - \theta)\cdot RP_{t-1} + \theta \cdot I_{new} \quad (2)$$

where I_H = min(h/(0.30·H), 1) is the flood depth h at the agent's location normalized by its body height H, adapted from [1], using the 0.30 ratio; I_S is the mean RP of social contacts (3–8 per agent) from whom the agent receives information in that step, with a probability that decays with distance; and I_N is the fraction of neighbors within 300 m that were evacuating in the previous time step. The weights α_H, β_S, and γ_N represent each agent's trust in the three sources; they are sampled from normal distributions and normalized to sum to 1 [1] (each draw floored at zero before normalization), and their means are examined through sensitivity analysis. The learning rate θ and the information update probability are sampled from normal distributions following the settings of [1], each clipped to [0, 1]. An agent starts evacuating when RP > τ.

2.3 Perception, walking, and routing.

Following the BDI architecture, each agent keeps its own belief network and updates only the road segments within its 30 m sight distance. Dry-land walking speed is sampled from age- and gender-specific ranges. In floodwater, speed is unchanged for h < 0.2 m and, for h ≥ 0.2 m, follows

$$V_p = a\cdot M^b \cdot \quad M = V^2h/g + h^2/2 \quad (3)$$

with age-dependent (a, b), capped at the dry-land speed. The formula was derived for h = 0.2–0.7 m and is extrapolated beyond this range. Because V is set to zero, M reduces to $h^2/2$. For agents older than 68, speed is reduced by 1.6% per year. Routes minimize travel time on each agent's own belief network using Dijkstra's algorithm to the fastest of the four shelters, and an agent avoids and re-plans around a road segment ahead when its flood depth exceeds 0.30 of the agent's height (baseline scenario, approximately knee height). The model advances in 1-min steps, each containing sixty 1-s movement substeps, and the flood field is updated every 5 min.

3 Results and discussion

In the baseline simulation across six villages, 155 of 5,933 agents (2.61%) initiated evacuation. Among these evacuees, 56.1% reached a shelter and 43.9% became stranded with no viable route (Table 1). These results reflect agents' autonomous risk perception only, with no official evacuation warning modeled; they should be read as a counterfactual lower-bound scenario rather than a reconstruction of actual 2025 evacuation behavior. A sensitivity analysis shows the evacuation rate rising sharply and non-linearly with the hazard-trust weight αH (Fig. 1), with the increase accelerating as αH rises (the largest absolute increase occurs between αH = 0.8 and 0.9). Since this weight has no empirical basis in the literature, it remains the largest source of uncertainty in these results.

Table 1 Evacuation, arrival, and stranded (no-route) outcomes by village.

Village	N	Evacuees (n)	Evacuation rate (% of N)	Arrived (% of evacuees)	Stranded (% of evacuees)
Beifu	891	47	5.27	66.0	34.0
Dahua	1,308	9	0.69	88.9	11.1
Daping	940	13	1.38	61.5	38.5
Datong	1,025	63	6.15	39.7	60.3
Da'an	773	8	1.03	62.5	37.5
Dama	996	15	1.51	66.7	33.3
All	5,933	155	2.61	56.1	43.9

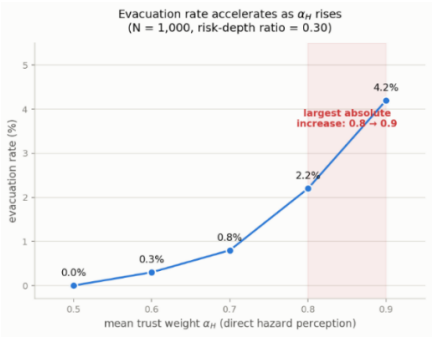


Fig. 1. Evacuation rate rises sharply with the hazard-trust weight αH, with the increase accelerating as αH rises (N = 1,000).

In addition, the questionnaire-based model used to predict each person's tendency to evacuate has very low explanatory power (pseudo-R^2 = 0.013), so the evacuation rates reported here (e.g., 2.61%) are indicative only and will be re-estimated with a local survey.

4 Conclusions

This study developed a BDI-based agent-based model that couples flood inundation data with individual evacuation decisions, risk perception, and floodwater mobility, and applied it to the 2025 Matai'an landslide dam overflow event in Guangfu Township, Hualien. Using real household-registry positions for 5,933 residents across six villages, the model produced marked spatial heterogeneity in evacuation outcomes, with villages nearest the flooded river channel showing both the highest evacuation rates and the highest rates of becoming stranded. A sensitivity analysis further showed that the evacuation rate is highly sensitive to each agent's trust in directly observed hazard information, accelerating as this trust rises — identifying it as a key parameter for future empirical validation.

References

[1] Roy, K.C., Hasan, S., Abdul-Aziz, O.I., Mozumder, P., Understanding the influence of multiple information sources on risk perception dynamics and evacuation decisions: An agent-based modeling approach, International Journal of Disaster Risk Reduction, 82 (2022) 103328.

[2] Moradi, H., Iskandar, R., Rodriguez, S., Singh, D., Dugdale, J., et al., Improving evacuation policies through agent-based modeling and stakeholder engagement in hazard-prone areas, International Journal of Disaster Risk Reduction, 119 (2025) 105280.

[3] Department of Household Registration, Ministry of the Interior (2025). Village-level household registration statistics by single year of age and gender, September 2025 (ODRP014). Open data API. https://www.ris.gov.tw/rs-opendata/api/v1/datastore/ODRP014/11409

Evaluating Levels of AI Agent in Hydrologic Modeling: A Comparative Analysis via Rainfall–Runoff Simulation

○ Yi-Fang WU[1*], Tsun-Hua YANG[1]

[1] Department of Civil Engineering, National Yang Ming Chiao Tung University, Hsinchu City, 300093, Taiwan.

[*]E-mail: 0218ca@gmail.com.

Abstract

AI agents driven by large language models (LLMs) can interpret user needs through natural language and autonomously chain together tools to complete multi-step tasks. They have increasingly been applied to software development, data analysis, and scientific research. Across these applications, AI agents differ in their degree of autonomy and in the way humans intervene. To clarify the differences among these autonomy levels, this study uses a simple rainfall–runoff (RR) model as an example and builds AI agents at levels L0 through L5. The RR modeling practice described in this research is intentionally straightforward. Areal-average rainfall is estimated using the Thiessen polygon method, effective rainfall is calculated using the SCS-CN method, and the resulting inflow hydrograph is derived using a synthetic unit hydrograph. All agent levels use the same input data, computational tools, model parameters, and hydrologic procedures. The primary difference among the levels lies in the degree of agent autonomy and the corresponding level of human involvement. This controlled setup allows the role and performance of the AI agent at each level to be compared while minimizing differences arising from the underlying hydrologic modeling framework. This study aims to clarify the differences in human–machine division of labor and in outputs across autonomy levels, and to highlight the role the knowledge base plays therein.

Keywords: AI agent; Large Language Model (LLM); Autonomy Levels; Rainfall–Runoff; Knowledge Base.

1 Introduction

AI agents driven by large language models (LLMs) can interpret natural-language requests and chain multiple tools to complete multi-step tasks. Such agents have recently entered hydrologic and water-system modeling: AQUAH performs end-to-end, language-based hydrologic modeling [1], and LLM-based multi-agent frameworks have been applied to water distribution networks [2]. These agents differ in their degree of autonomy. Yan et al. [3] classified hydrologic-modeling agents into six levels (L0–L5), from fully manual operation at L0 to full autonomy at L5, with progressively less human involvement. However, the differences among the levels in modeling results and human involvement, as well as the construction of the supporting domain knowledge base, have not been thoroughly discussed. This study builds agents at L0–L4 for a simple rainfall–runoff task with the same inputs, tools, and initial parameters, so that only the autonomy level varies. The study aims to clarify the differences in human–machine division of labor and in outputs across levels, and the role of the knowledge base.

2 Materials and methods

2.1 Case and model

To minimize the influence of observational uncertainties and inaccuracies in input parameters, this study focuses exclusively on an idealized case. The observed inflow was generated by the same RR model with CN = 78 and time to peak (Tp) = 4 hr, without noise, with a baseflow of 50 m³/s and a peak of 1051 m³/s. Initial inputs of all levels such as CN = 70, Tp = 6 hr, and the initial abstraction ratio = 0.2 are fixed. The RR modeling process consists of four main steps. First, rainfall observations from individual gauges are converted into catchment-averaged rainfall using the Thiessen polygon method. Second, effective rainfall is estimated using the Soil Conservation Service Curve Number (SCS-CN) method, with the curve number (CN) serving as the key parameter. Third, the effective rainfall is convolved with the SCS triangular unit hydrograph, characterized by its Tp, to generate the direct runoff hydrograph. Finally, a constant baseflow is added to obtain the total inflow hydrograph.

2.2 Implementation of the autonomy levels

Adapted from the six-level framework [3], one agent was implemented at each of L0–L4; L5 is not implemented because hydrologic results still require expert judgment and there is no automatous action can be applied in the synthetic study. Assumptions are made: all levels share the same inputs, model, and tools, the inputs being rainfall, gauge weights, and observed inflow, and the differences among the levels are summarized in Table 1.

Table 1 Comparison of the five implemented autonomy levels

Level	Input	Tools	Agent's role	Output
L0	Rainfall, gauge weights, and observed inflow	Thiessen, effective, hydrograph, plot	None	Hydrograph plot and metrics
L1			Executes specified steps	
L2			Parses the request and runs	
L3		Thiessen, effective, hydrograph, plot, advise and adjust with the knowledge base	Explanation and recommendation	+ recommen-dations with reasons
L4			Applications of recommendation and execute optimization	+ adjustment to the best results

2.3 Experimental design

The agent is powered by Claude Sonnet 4.6. Its advise_adjust_llm tool invokes the LLM to generate recommendations, which are subsequently validated for formatting compliance, the validity of cited knowledge-base entries, and adherence to predefined parameter ranges.

Recommendations that fail any of these validation checks are rejected. The knowledge base is stored as an inspectable, structured file with three types of content. The first is the role of each parameter, its admissible range, and the maximum change per recommendation: CN governs runoff volume, with a range of 30 to 98 and a maximum change of 10; Tp governs peak timing and hydrograph shape and also affects peak magnitude without changing total volume, with a range of 1 to 24 hr and a maximum change of 3 hr. The second is calibration principles: CN is aligned with volume and Tp with peak timing, and the direction and size of adjustments are derived from physical relations. The third is the model equations, including the SCS-CN effective-rainfall equations and their inverse, and the peak discharge and base time of the unit hydrograph.

2.4 Evaluation

Model performance is evaluated using the relative peak-flow error E_p and the Nash–Sutcliffe efficiency (NSE):

$$E_p = \frac{Q_{p,\mathrm{sim}} - Q_{p,\mathrm{obs}}}{Q_{p,\mathrm{obs}}} \times 100\% \quad (1)$$

$$\mathrm{NSE} = 1 - \frac{\sum_{i=1}^{n}\left(Q_{\mathrm{obs},i} - Q_{\mathrm{sim},i}\right)^2}{\sum_{i=1}^{n}\left(Q_{\mathrm{obs},i} - \overline{Q_{\mathrm{obs}}}\right)^2} \quad (2)$$

where $Q_{sim,i}$ and $Q_{obs,i}$ are the simulated and observed inflow at time step i, $Q_{p,sim}$ and $Q_{p,obs}$ are the simulated and observed peak flows, $\bar{Q}_{obs}$ is the mean observed inflow, and n is the number of time steps. An NSE of 1 indicates a perfect fit, and negative values indicate performance worse than using the observed mean.

3 Results and discussion

Fig. 1 shows the comparison between observations and simulations. L0–L3 produce the same result: the peak is 538 m³/s, which underestimates the observed 1051 m³/s by 48.8%, and the NSE is 0.239. L3 explains the reasons for the mismatch between simulation and observation and recommends parameter adjustments, but does not modify the parameters, so its simulated result is the same as that of L0–L2. In addition to the same recommendations, L4 applies them itself and re-runs the simulation, and the scenario adjusting both CN and Tp performs best, raising the peak to 1009 m³/s, close to the observation. Compared with the initial simulation, the absolute peak error decreases from 48.8% to 4.0%, a reduction of 44.8 percentage points or 92%, and the NSE increases from 0.239 to 0.996, a gain of 0.757.

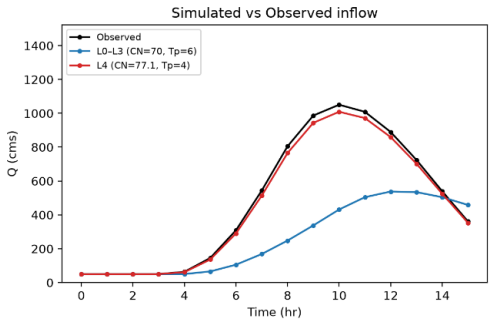


Fig. 1 Observed inflow, simulated inflow of L0–L3, and simulated inflow of the best L4 scenario.

Beyond accuracy, the agents at the different levels are evaluated by the human intervention count (HIC), Eq. (3), and the human intervention reduction (HIR), Eq. (4), which quantify how many times a human must intervene to complete a rainfall–runoff modeling task:

$$HIC = N_{intervention} \quad (3)$$

$$HIR_x = \left(1 - \frac{HIC_x}{HIC_0}\right) \times 100\% \quad (4)$$

where $N_{intervention}$ is the number of human interventions, HIC_x is the count at level x (L0–L4), and HIC_0 is the count at L0, the manual process. The counts refer to the interventions required to reach the final optimized results in terms of the performance indices in Eqs. (1) and (2). The counts are determined level by level from L0, with each tool execution counted as one intervention. Table 2 indicates that a higher agent level progressively reduces the number of required human interventions. Compared with the manual process at L0, L4 shows the greatest reduction, requiring only one intervention and achieving a 90.9% reduction relative to L0. The reduction stems mainly from two transitions: from L1 to L2, the organization and execution of the workflow shift from the user to the agent, and from L3 to L4, parameter judgment and adjustment are also taken over by the agent, turning the user from an operator into a reviewer.

Table 2 Comparison of HIC across the five implemented autonomy levels

Level	Human activities	HIC	HIR (%)
L0	Prepare the four tools and execute every modeling step	11	0.0
L1	Enter parameters, execute the four tools, end, and re-enter parameters	7	36.4
L2	Execute the predefined workflow, enter parameters, and view the plot	3	72.7
L3	Execute and modify parameters after reading the agent's recommendations	2	81.8
L4	Approve the final results	1	90.9

4 Conclusions

This study implemented AI agents at five autonomy levels on an identical RR workflow and compared them on an idealized case with known parameters. At L0–L2 the user decides the parameters and the initial simulation is identical; L3 explains the mismatch between simulation and observation and recommends adjustments, and L4 further applies them itself and re-runs the simulation, reducing the absolute peak error from 48.8% to 4.0% and raising the NSE from 0.239 to 0.996. The HIC decreased from 11 at L0 to 1 at L4, a reduction of 90.9%, showing that higher autonomy shifts the user from an operator to a reviewer. All experiments so far were conducted under an idealized condition, and the knowledge base was refined on this case, so the next step is to implement the approach in a real study area and to examine whether the HIC remains a reliable indicator when the parameters are unknown.

Reference

[1] S. Yan, Z. Li, S. Zhu, Y. Wen, M. Zhang, M. Chen, J. Cao, Y. Hong, AQUAH: Automatic Quantification and Unified Agent in Hydrology, Proceedings of the IEEE/CVF International Conference on Computer Vision (ICCV) Workshops (2025) 2926–2935.

[2] J. Wang, G. Fu, D. Savić, Leveraging large language models for automating water distribution network optimization, Water Research, 288 (2026) 124536.

[3] S. Yan, M. Chen, Z. Li, Y. Wen, S. Zhu, M. Zhang, D. Liu, J. Cao, X. Chen, C. Deng, T. Yang, Y. Hong, AI Agent for Hydrologic Modeling: Definition, Development, and Application, Geophysical Research Letters, 53 (2026) e2025GL119814.

Evaluation of the accuracy and applicability of 1m Resolution inundation analysis

○ Nanako INOKAWA[1*]& Satoru OISHI[2]
[1]Department of Civil and Environmental Engineering, Tohoku University, Miyagi 980-8579, Japan.
[2] Research Center for Urban Safety and Security, Kobe University, Hyogo 657-8501, Japan.
[*]E-mail: nanako.inokawa.d7@tohoku.ac.jp

Abstract
Inundation analysis is essential for predicting both pluvial and fluvial flood risk and for planning effective countermeasures. Inundation models have been developed over many decades, and their spatial resolution has become increasingly finer as computational capacity has grown. In recent years, high-resolution digital elevation models (DEMs) with grid spacings of 5 m or even 1 m have become available, enabling inundation analyses at 1–2 m resolution that can explicitly represent local features such as roads, canals, and buildings. However, such high-resolution analysis imposes a heavy computational load, making it impractical for large areas; it should therefore be applied selectively, only to areas where it is needed. In this study, we conducted 1 m and 5 m resolution inundation analyses, with and without building representation, of the Chikuma River flood caused by Typhoon Hagibis (Typhoon No. 19) in 2019, using DEMs published by the Geospatial Information Authority of Japan (GSI). The accuracy of each analysis was evaluated against field-surveyed inundation depths. As a result, the 5 m resolution analysis achieved sufficiently high accuracy at the regional scale, with an RMSE of 0.53 m. However, the 1 m resolution analysis showed higher accuracy around levee breach sites, roads, and canals, where the local topography changes abruptly. In addition, representing buildings in the 1 m analysis tended to improve accuracy near the levee breach site. These results suggest that selectively applying 1 m resolution analysis, including building representation, to areas with abrupt topographic changes can efficiently improve the accuracy of inundation analysis while keeping the computational cost manageable.
Keywords: inundation analysis; DEM; high-resolution; 1m resolution; fluvial flooding.

1 Introduction
High-resolution inundation analysis has become common in recent years for both pluvial and fluvial flooding. In urban areas, which contain many features such as buildings, roads, and other infrastructure, detailed analysis is necessary for accurate risk assessment, as shown at 2 m resolution by Fewtrell et al. (2008) [1] and at 1 m resolution for pluvial flooding by Lee et al. (2025) [2]. However, such high-resolution analysis is impractical for applications such as real-time flood forecasting and large-area analysis. The objective of this study is to clarify where 1 m resolution is necessary by comparing 1 m and 5 m resolution inundation analyses, with and without building representation.

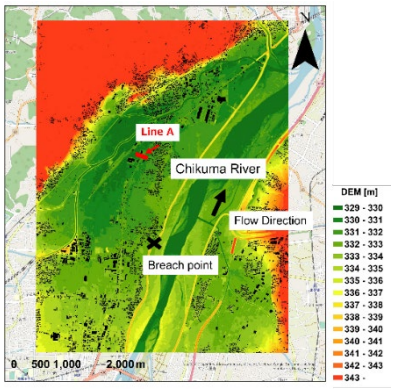
2 Materials and methods


Fig 1. Study Area (Chikuma River)

Figure 1 shows the study area along the Chikuma river with the 1m DEM published by GSI. This area was inundated in 2019 as a result of a levee breach, the width of which was estimated to be approximately 70m [3]. The study area is surrounded by mountains, with high elevations to the northwest and southeast.

We used an inundation model based on the two-dimensional shallow water equations. The governing equations are given as Esq. (1)-(3):

$$\frac{\partial h}{\partial t}+\frac{\partial M}{\partial x}+\frac{\partial N}{\partial y}=0 \quad (1)$$

$$\frac{\partial M}{\partial t}+\frac{\partial uM}{\partial x}+\frac{\partial vM}{\partial y}=-gh\frac{\partial H}{\partial x}-gn^2u\frac{\sqrt{u^2+v^2}}{h^{1/3}} \quad (2)$$

$$\frac{\partial N}{\partial t}+\frac{\partial uN}{\partial x}+\frac{\partial vN}{\partial y}=-gh\frac{\partial H}{\partial y}-gn^2v\frac{\sqrt{u^2+v^2}}{h^{1/3}} \quad (3)$$

Where h is the water depth (m), n is Manning's roughness coefficient ($m^{-1/3}\cdot s$), $M=uh$, $N=vh$, M,N are the discharge fluxes per unit width in the x and y directions, respectively (m^2/s), u,v are the flow velocities in the x and y directions, respectively (m/s), H is the water level (m), and g is the gravitational acceleration (m/s^2). Since the study area is dominated by agricultural land, Manning's roughness coefficient was set to 0.018 based on the Manual for preparing Flood inundation Hazard Map [4]. A staggered grid was adopted for the computational mesh, and the leapfrog scheme was used for time integration. For topography, the GSI 1m mesh DEM was used for the 1m resolution analysis, and the GSI 5m mesh DEM was used for the 5m resolution analysis. The inflow and drainage conditions were set with reference to Sato et al. [5], whose

settings were shown to reproduce the observed flood-mark depths. The simulation covered a 24-hour period before and after the levee breach, with the breach occurring 4 hours after the start of the computation. In this study, we conducted inundation analyses for three cases: 1 m resolution with buildings, 1 m resolution without buildings, and 5 m resolution without buildings. The building data were obtained from the 2018 building outline data in the Fundamental Geospatial Data published by GSI [6]; grid cells whose centers fell within a building polygon were treated as impermeable building cells.

3 Results and discussion

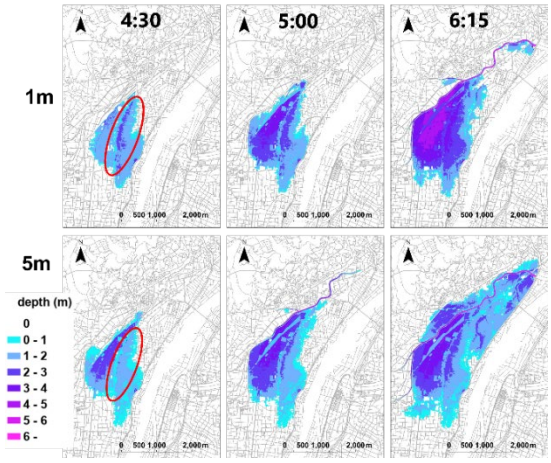


Fig 2. Temporal Change in inundation depth

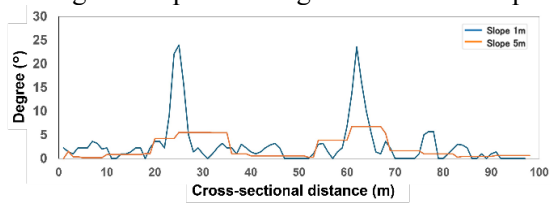


Fig 3. Cross-sectional slope angle profiles along line A in Fig 1.

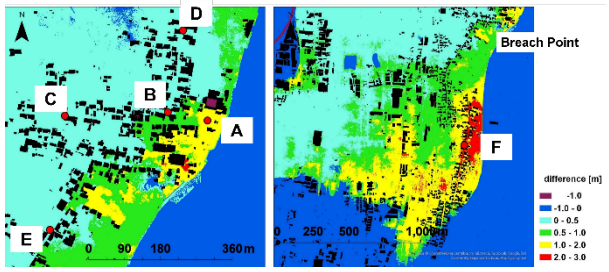


Fig 4. Differences in maximum inundation depth (1m with buildings – 1m without buildings)

Figure 2 shows the temporal change in inundation depth without buildings. At 4 h 30 min, the farmland along the Nagano Bypass (red circles) was inundated to 2–3 m in the 1 m analysis but only 1–2 m in the 5 m analysis, because the 1 m DEM represents the road-edge step as a slope of about 25°, whereas the 5 m DEM smooths it to below 7° (Fig. 3).

As shown in Fig. 4, the closer to the levee breach, the larger the maximum inundation depth tended to be in the 1 m resolution analysis with buildings than in the one without buildings. At Point A, which is located near the levee breach, the maximum inundation depth was 1.63 m without buildings and 2.71 m with buildings, compared with the field-surveyed depth of 2.40 m; the analysis with buildings overestimated the depth by 0.31 m, whereas the analysis without buildings underestimated it by 0.77 m. Thus, the analysis with buildings reproduced the maximum inundation depth more accurately near the levee breach. At Points B–F, which are farther from the levee breach, the values from the analysis without buildings were closer to the field-surveyed depths. However, the analysis with buildings yielded larger depths, which are on the safe side for risk assessment, suggesting that the flow-obstruction effect of buildings was reflected in the results.

Table 1 Maximum Depth of Point A-F

(m)	field-surveyed inundation depths	1m resolution without buildings	1m resolution with buildings
点 A	2.40	1.63	2.71
点 B	2.45	2.18	2.73
点 C	2.18	2.52	2.74
点 D	2.02	2.25	2.44
点 E	1.93	2.19	2.45
点 F	1.38	-	2.22

4 Conclusions

Future work will establish criteria for identifying where 1 m resolution analysis should be applied over wider areas and improve the model to represent flow between buildings, toward providing detailed flood risk information at the individual-house level.

Reference

[1] Fewtrell, T. J., Bates, P. D., Horritt, M., Hunter, N. M., Evaluating he effect of scale in flood inundation modelling in urban environments, Hydrological Processes, Vol. 22, No. 26, 5107‐5118, 2008.

[2] Lee, Jun-Hak, Lee, Seungsoo, Kim, Bomi, Choi, Hyeonjin, Noh, Seong Jin：Evaluating the Effects of Spatial Resolution on 2D Pluvial, Flood Modeling in Urban Built Environments, Journal of Flood Risk Management, Vol. 18, No. 3, e70105, 2025.

[3] Japan Society of Civil Engineers (JSCE) Committee on Hydroscience and Hydraulic Engineering, 2020.2019 Typhoon No.19 Heavy Rain Disaster Investigation Report – Volume of Chubu and Hokuriku Regions (in Japanese), JSCE, p.222

[4] Ministry of Land, Infrastructure, Transport and Tourism, Flood Inundation Assumption Area Mapping Manual(The forth edition), 2015

[5] Sato, D. and Takeda, M. and Kawaike, K and Toyota, M., Inundation analysis due to dike break of the chikuma river considering drainage process and house damage , Journal of the Japan Society of Civil Engineers B1, Vol.76, No.2, I_625-I_630, 2020

[6] Geospatial Information Authority of Japan, Basic mapping information download service, https://www.gsi.go.jp/kiban/

Sensitivity of simulated rice yield-loss events caused by irrigation-reservoir pre-release to the yield-loss threshold

○ Atsuya IKEMOTO[1*] & So KAZAMA[1]
[1]Department of Civil and Environmental Engineering, Tohoku University, Miyagi 980-8579, Japan.
[*]E-mail: ikemoto.atsuya.s1@dc.tohoku.ac.jp

Abstract
Pre-release from irrigation reservoirs before heavy rainfall creates flood-storage capacity but may reduce the water available for paddy rice. A yield-loss event is defined by a threshold of relative yield loss (RYL) that is not uniquely determined. AquaCrop-OSPy was coupled with a daily reservoir water-balance model for 931 grid cells across Japan and 20 d4PDF ensemble members, and paired simulations with and without pre-release were evaluated for thresholds of 10%, 20%, and 30%. Under complete drawdown, the event proportion decreased with an increasing catchment-to-irrigated-area ratio (X') at every threshold. Raising the threshold reduced the proportion by roughly one order of magnitude per 10-point step, more strongly at large X', so the contrast between the smallest and largest X' grew from a factor of 38 at 10% to the order of 10^2 at 30%. The mean RYL among events was almost independent of X'. The absolute event proportion depends strongly on the threshold, but the ranking of reservoirs by X' does not.
Keywords: pre-release; irrigation reservoir; paddy rice; AquaCrop; sensitivity analysis.

1 Introduction

In Japan, pre-release from irrigation reservoirs has been promoted as a measure to create flood-storage capacity before heavy rainfall [1, 2]. The flood-control effect is largest when a reservoir is emptied [1], but the water released is the water that would otherwise be supplied to paddy fields. The heading and flowering stage of rice, at which the crop is sensitive to water stress, overlaps with the season of typhoons and heavy rainfall in Japan. If the rainfall after the release does not restore the storage, the irrigation supply around heading may therefore be limited.

To screen reservoirs and regions for this risk, a simulated record can be classified as a yield-loss event when its relative yield loss (RYL) exceeds a threshold, and the proportion of such events can be compared among reservoir structures. The threshold, however, is not uniquely determined. In crop insurance for paddy rice in Japan, payment begins when the loss exceeds 10–40% of the standard yield, depending on the underwriting method and the coverage level [3]. A ranking obtained at one threshold may not hold at another.

This study examined whether the dependence of simulated yield-loss events on reservoir structure is robust to the choice of threshold. The occurrence and the magnitude of yield loss were evaluated separately for thresholds of 10%, 20%, and 30%.

2 Materials and methods

Rice growth and the field water balance were simulated with AquaCrop-OSPy (version 3.0.12) [4, 5] and coupled on a daily basis with the water balance of an irrigation reservoir. The daily minimum and maximum air temperatures, precipitation, and reference evapotranspiration were derived from 20 ensemble members of the historical experiment of d4PDF (20-km grid; 2000–2010) [6] for 931 grid cells in which irrigation reservoirs are distributed. Transplanting dates were set by prefecture, and the growing degree days required for each growth stage were set by grid cell; the crop parameters and a clay paddy soil with a plow pan were uniform across Japan. A paddy water-management rule with ponding, midseason drainage, and final drainage determined the daily irrigation requirement.

The reservoir storage was updated daily as $S(t) = S(t-1) + Q_{in}(t) - Q_{out}(t) - \mathrm{Spill}(t)$. The inflow Q_{in} was the product of the daily precipitation, the catchment-to-irrigated-area ratio X', and a reference irrigated area of 1.0 ha. The supply Q_{out} was the smaller of the irrigation requirement and the available storage, and water exceeding the full storage spilled. The reservoir was described by X' and the storage capacity per unit irrigated area Y, each with five levels at the 5th, 25th, 50th, 75th, and 95th percentiles of the reservoirs in Japan [1]: $X' = 0.04889$, 0.719, 5.354, 37.09, and 492.4, and $Y = 22{,}947$–$29{,}921$ m^3 ha^{-1}.

Pre-release was performed once a year on a day sampled within ±150 growing degree days around the onset of harvest-index formation. The same day was applied to all scenarios of the same grid cell, member, and year. The release lowered the storage to a fraction $R = 0$ (complete drawdown, a stress test), 0.25, 0.50, or 0.75 of the full storage, after which the ordinary water balance resumed. Each release simulation was paired with a baseline simulation without release under identical conditions, and RYL was calculated as $1 - Y_R/Y_{base}$, where Y_R and Y_{base} are the yields with and without release.

A record with RYL exceeding the threshold T (10%, 20%, or 30%) was defined as a yield-loss event. For each combination of X' and R, 1,006,100 paired records pooled over the five Y levels were used to calculate the yield-loss event proportion, with its 95% Wilson score interval [7], and the conditional mean RYL among the events. Because the release was not conditioned on precipitation, the proportion is not an annual probability of yield loss under actual operation.

3 Results and discussion

Yield-loss events occurred almost exclusively under complete drawdown. At R = 0.25, events occurred only for T = 10%, with 25, 13, and 1 records at the three smallest X' levels (at most 0.0025%), and no event occurred at $R \geq 0.50$ for any threshold. Retaining a quarter of the storage thus avoided almost all events; the following results are for R = 0.

Fig. 1. (a) Yield-loss event proportion (bars: 95% Wilson intervals) and (b) conditional mean RYL against X' for each threshold (R = 0).

Table 1 Yield-loss event proportion (%) at R = 0 for each threshold T.

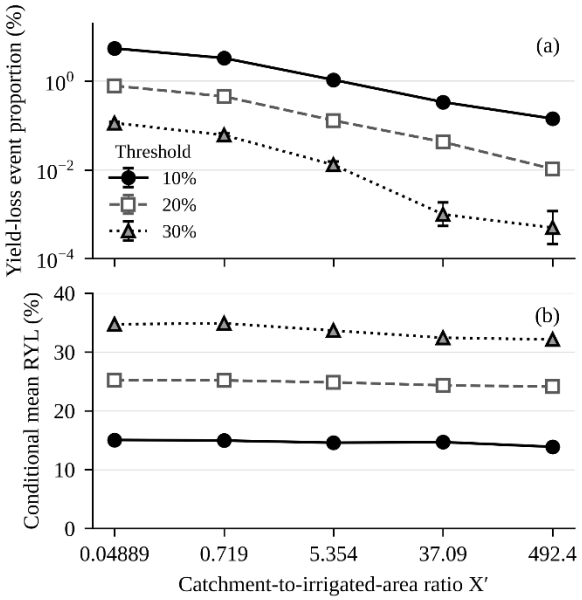
X'	T = 10%	T = 20%	T = 30%
0.04889	5.42	0.779	0.113
0.719	3.28	0.449	0.0603
5.354	1.06	0.129	0.0129
37.09	0.335	0.0422	0.00099
492.4	0.142	0.0104	0.00050
Ratio*	38	75	~230

*Proportion at X' = 0.04889 divided by that at X' = 492.4.

The yield-loss event proportion decreased monotonically with increasing X' at every threshold, and the ranking of the five X' levels did not change (Table 1; Fig. 1a). Raising the threshold reduced the proportion by roughly one order of magnitude per 10-point step. The reduction was larger at large X': from T = 10% to 30%, the proportion decreased by a factor of 48 at X' = 0.04889 and of approximately 290 at X' = 492.4. As a result, the ratio of the proportion at the smallest X' to that at the largest X' increased from 38 at 10% to 75 at 20% and to approximately 230 at 30%. At 30%, only 10 and 5 events occurred at the two largest X' levels, and the ratio ranges from approximately 90 to 560 within the confidence intervals; only its order of magnitude is meaningful. A reservoir with a large catchment refills quickly, so a severe loss requires an extended dry spell, which may explain the steeper decrease at large X'.

The conditional mean RYL among the events was almost independent of X' at every threshold: 13.9–15.1% at 10%, 24.1–25.2% at 20%, and 32.1–34.9% at 30% (Fig. 1b). The corresponding absolute yield losses were 1.07–1.13, 1.81–1.94, and 2.45–3.04 t ha^{-1}. The reservoir structure thus affected the frequency of yield loss but hardly its magnitude once a loss occurred, and this separation held at all three thresholds.

The sensitivity to the threshold therefore has two sides. The absolute value of the event proportion is highly sensitive: it changes by about one order of magnitude for a 10-point change in the threshold, so it must be reported together with the threshold and should not be read as a probability. In contrast, the ranking of reservoir structures by X' and the separation between frequency and magnitude are insensitive, and the contrast among X' levels becomes sharper at stricter thresholds. For screening, a strict threshold isolates the smallest X' more clearly, whereas a lenient one gives more events and narrower intervals. Thresholds above 30% could not be evaluated because events became too few, and the crop parameters were uniform across Japan.



4 Conclusions

The yield-loss event proportion under irrigation-reservoir pre-release decreased by roughly one order of magnitude per 10-point increase in the threshold, whereas its decrease with the catchment-to-irrigated-area ratio and the near independence of the conditional loss from this ratio held at 10–30%. Screening of reservoirs by this ratio is therefore not an artifact of the threshold choice.

Reference

[1] A. Ikemoto, S. Kazama, T. Yoshida, H. Yanagihara, Evaluation of an adaptation strategy for flood damage mitigation under climate change through the use of irrigation reservoirs in Japan, Water Resources Management, 37 (2023) 4159-4175.

[2] MAFF, Guidebook for strengthening the flood-control function of irrigation ponds (in Japanese), Tokyo (2018).

[3] MAFF, Overview of crop mutual aid under the Agricultural Insurance Act (in Japanese), Tokyo (2025).

[4] D. Raes, P. Steduto, T.C. Hsiao, E. Fereres, AquaCrop—The FAO crop model to simulate yield response to water: II. Main algorithms and software description, Agronomy Journal, 101 (2009) 438-447.

[5] T.D. Kelly, T. Foster, AquaCrop-OSPy: Bridging the gap between research and practice in crop-water modeling, Agricultural Water Management, 254 (2021) 106976.

[6] R. Mizuta et al., Over 5,000 years of ensemble future climate simulations by 60-km global and 20-km regional atmospheric models, Bulletin of the American Meteorological Society, 98 (2017) 1383-1398.

[7] E.B. Wilson, Probable inference, the law of succession, and statistical inference, Journal of the American Statistical Association, 22 (1927) 209-212.

Precipitation Characteristics at Different Spatial Resolutions Using a Large-Ensemble Climate Dataset

○ Ryotaro TAHARA[1*] & Yusuke HIRAGA[1]
[1]Department of Civil and Environmental Engineering, Tohoku University, Sendai 980-8579, Japan.
[*]E-mail: tahara.ryotaro.q7@dc.tohoku.ac.jp

Abstract

Reliable estimation of rare extreme precipitation requires large climate samples and high-resolution rainfall information for flood risk assessment. Because dynamical downscaling of large ensembles is computationally expensive, understanding changes between coarse- and high-resolution precipitation fields is important for developing statistical and machine learning-based alternatives. We analyzed precipitation from the 60-, 20-, and 5-km d4PDF datasets using 10 ensemble members during June–October of 1951–2010. Following temporal declustering and object identification, we matched precipitation objects across resolutions, focusing on one-to-one correspondences. At higher spatial resolutions, matched precipitation objects generally showed reduced areas (62–77% of pairs) and increased native-grid 95th-percentile intensities (70–80% of pairs). Nevertheless, substantial spatial displacement remained even for one-to-one matches, with median centroid displacements of 75–101 km.

Keywords: Large-ensemble climate dataset; Precipitation characteristics; Object-based analysis.

1 Introduction

Estimating rare extreme precipitation and associated flood magnitudes is essential for flood risk assessment. However, conventional extreme value analysis is constrained by observational records spanning only a few decades, leading to substantial uncertainty in estimates of rare events. Large-ensemble climate datasets help address this limitation by providing thousands of years of simulated climate data for statistical analysis.

Hydrological impact assessments and local flood risk management also require precipitation information at spatial resolutions of a few kilometers. Dynamical downscaling with regional climate models provides high-resolution precipitation fields while maintaining physical consistency. However, applying this approach to all members of a large ensemble over long periods requires substantial computational and storage resources.

Statistical and machine learning-based downscaling methods offer less computationally demanding alternatives [1]. Many such methods learn relationships between coarse-resolution precipitation fields and their dynamically downscaled high-resolution counterparts. Characterizing these relationships requires an understanding of changes in precipitation fields during dynamical downscaling.

Such changes are not limited to precipitation intensity. Some precipitation areas exhibit intensity changes with little spatial displacement. Others undergo substantial shifts in location or spatial structure. Large displacement may complicate the learning of local relationships between coarse- and high-resolution fields, potentially affecting downscaling performance.

This study aims to quantify changes in precipitation intensity and spatial structure across resolutions using a large-ensemble climate dataset. As a first step toward characterizing precipitation transformations during dynamical downscaling, we examine the area, intensity, and centroid displacement of matched precipitation objects at 60-, 20-, and 5-km resolutions.

2 Materials and methods

2.1 Datasets

This study uses the database for Policy Decision Making for Future Climate Change (d4PDF). We analyzed three datasets at different spatial resolutions: the 60-km global dataset (d4PDF60km; Mizuta et al., 2017), the 20-km regional dataset (d4PDF20km; Mizuta et al., 2017), and the 5-km regional dataset (d4PDF5km; Kawase et al., 2023). The d4PDF20km and d4PDF5km datasets cover Japan and its surrounding regions. We used hourly precipitation data from 10 ensemble members (HPB_m001–HPB_m010) common to all three datasets under present-day climate conditions. The analysis covered the wet season (June–October) over the 60-year period from 1951 to 2010.

2.2 Methodology

We applied an object-based approach to identify precipitation events and match precipitation objects across different spatial resolutions.

1. Precipitation Event Identification

To identify representative precipitation events and reduce temporal dependence between events, we calculated the hourly domain-mean precipitation from d4PDF60km over the common domain of the three datasets. The mean value across all ensemble members and the entire analysis period was used as the threshold for event detection. Consecutive hours exceeding this threshold were identified as event candidates, with the peak hour representing each candidate. To ensure temporal independence, we applied a 24-hour declustering procedure. Event candidates were ranked by peak precipitation, and candidates within ±24 hours of a higher-ranked event were excluded.

2. Precipitation Object Identification and Matching

The precipitation objects were identified using a threshold of 1.0 mm h^{-1} and eight-connected component labeling. The 20-km and 5-km precipitation fields were upscaled to the 60-km grid before object detection. Then objects at lower and higher resolutions were matched using following two criteria:

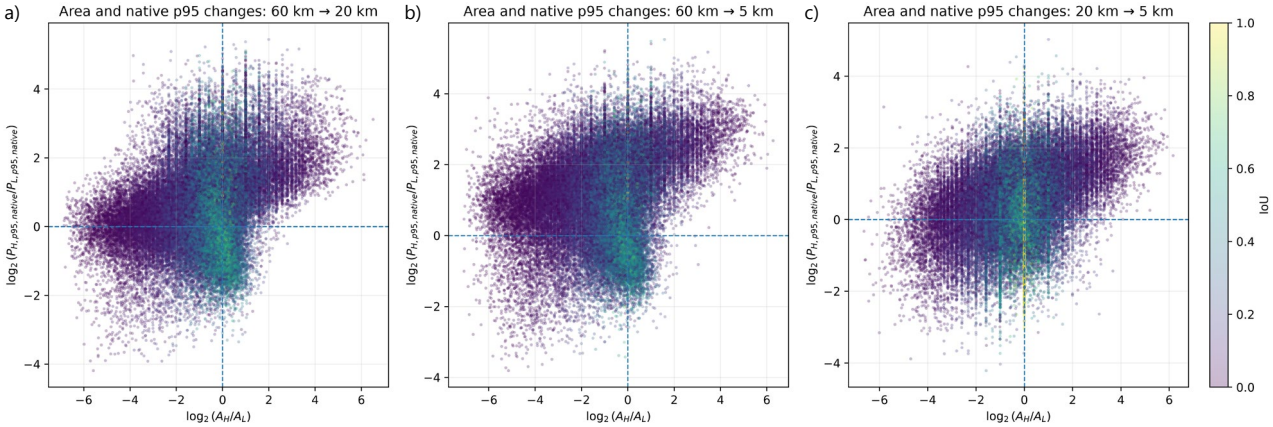


Fig.1. Relationship between changes in precipitation object area and native-grid 95th-percentile precipitation intensity (p95) for one-to-one matched objects across three spatial resolution pairs: (a) 60–20 km, (b) 60–5 km,

- Spatial overlap: All object pairs with any spatial overlap were linked (i.e. $IoU > 0$).
- Centroid distance: For objects without any overlap-based links, an additional link was established when the centroid distance satisfied following equation (Davis et al., 2006):

$$D^* = \frac{D}{(\sqrt{A_L} + \sqrt{A_H})/2} < 1$$

where D is the centroid distance and A_L and A_H are the areas of the two objects. This criterion allows spatially separated objects to be matched when their centroid distance is sufficiently small relative to their characteristic spatial scales.

In this study, we focused only on one-to-one object matches, excluding cases involving object splitting or merging.

3 Results and Discussion

Fig.1 shows the relationship between changes in precipitation object area and intensity for matched object pairs across different spatial resolutions. The analysis included 75,272 one-to-one (1:1) matches for 60–20km, 65,826 for 60–5km, and 81,194 for 20–5km. Across all three resolution pairs, precipitation objects tended to become smaller and more intense at higher spatial resolutions. The proportion of objects with reduced area was approximately 71%, 77%, and 62% for 60–20 km, 60–5 km, and 20–5 km, respectively. The 95th-percentile precipitation intensity calculated on each dataset's native grid (p95) increased in approximately 70%, 80%, and 74% of the matched pairs, respectively. These tendencies were most pronounced for the 60–5 km comparison. However, the wide scatter indicates substantial variability in the relationship between changes in object area and precipitation intensity.

Fig.2a shows the empirical cumulative distribution functions (ECDFs) of centroid displacement for 1:1 matched precipitation objects across the three resolution pairs. Fig.2b shows the corresponding distributions of size-normalized centroid displacement (D^*). Substantial spatial displacement was observed even for 1:1 matched objects. The median centroid displacement ranged from approximately 75 to 101 km, and more than half of the 60-to-5-km pairs exhibited displacements exceeding 100 km (Fig. 2a). Normalization by object size did not eliminate this displacement, with median

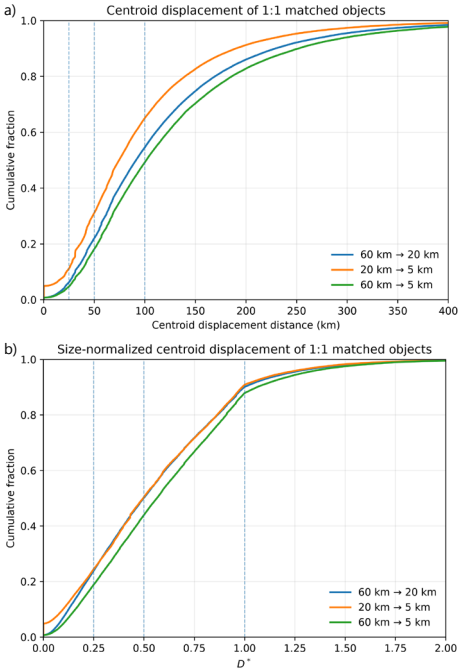


Fig.2. ECDFs of (a) centroid displacement distance and (b) D^*across three spatial resolution pairs.

D^* values of approximately 0.50–0.56 across the three resolution pairs (Fig. 2b). Approximately half of the matched pairs, and 56% for the 60-to-5-km comparison, had $D^* \geq 0.5$, indicating centroid shifts equivalent to at least half of the representative object length scale. Moreover, approximately 9–12% of the pairs exhibited $D^* \geq 1$, indicating cases in which the centroid displacement exceeded the characteristic length scale of the paired precipitation objects.

Reference

[1] Liu, Y., Wright, D. B., Quintero, F., England, J. F., Smith, J. A., & Yan, L. (2025). A nonstationary probabilistic approach for probable maximum precipitation estimation based on global climate model large ensembles. Journal of Hydrometeorology, 26(12), 1957-1980.

Correction of Precipitation Data for Long-Term Runoff Analysis

○ Ryuto UGAJIN[1*], Yoshiyuki YOKOO[2] & So KAZAMA[1]
[1]Graduate School of Engineering, Tohoku University, Miyagi 980-8579, Japan.
[2] Faculty of Symbiotic Systems Science, Fukushima University, Fukushima 960-1296, Japan.
[*]E-mail: ugajin.ryuto.q5@dc.tohoku.ac.jp

Abstract

Radar precipitation underestimation causes water balance discrepancies in snowy runoff modeling. To enable wide-area analysis using precipitation and temperature, we evaluate multi-factor correction partitioning rain and snow in a headwater catchment via the RRI model. Jointly correcting rain and snow improved temporal runoff reproducibility over snowfall-only correction. Doubling basal snowmelt to 4.0 mm day⁻¹ and setting the rain-snow threshold temperature to 0 °C corrected cumulative runoff slopes and mitigated early snowmelt overestimation.

Keywords: Long-term runoff analysis, Precipitation correction, Water balance discrepancy, Snowy mountainous basin, Distributed hydrological model.

1 Introduction

Long-term runoff analysis is essential for evaluating water resources. In large-scale rainfall-runoff modeling, radar-based gridded precipitation accounts for spatial rainfall distribution. However, water balance discrepancies occur where observed runoff depth exceeds gridded basin precipitation (Kashiwa et al., 2010; K. Suzuki, 2018), indicating non-negligible input errors. Previous studies adjusted snowfall only to balance water budgets, leaving rainfall uncorrected and summer streamflow unaddressed (Kashiwa et al., 2010). Because Radar-AMeDAS analyzed precipitation underestimates rainfall by approximately 10% at intensities of 1 mm h⁻¹ or higher (H. Suzuki et al., 2017), correcting rainfall is also crucial. Toward wide-area long-term modeling using only precipitation and temperature inputs, this study explores explaining year-round runoff by determining correction factors that align simulated and observed annual runoff in a small mountainous catchment through iterative data and parameter adjustments.

2 Materials and methods

Fig. 1 shows the target river system and study catchment. We selected the Nakamura gauging station catchment, located in a heavy snowfall zone dominated by snow accumulation and snowmelt. Selecting a high-elevation, low-temperature catchment minimizes evapotranspiration modeling errors.

For meteorological inputs, Radar-AMeDAS analyzed precipitation and estimated temperature distributions from the Japan Meteorological Business Support Center (JMBSC) were used (temporal resolution: 0.5 h, spatial resolution: 1 km). Evapotranspiration was simulated using the Thornthwaite method, and snow accumulation and snowmelt using the degree-hour method. The snowmelt factor was optimized so that calculated snow clearance dates matched station observations. Long-term runoff analysis was conducted by driving a runoff model with effective precipitation from this land surface model. The analysis period spans 2016 to 2024 (2016 as a spin-up period, evaluation from 2017 onward). Assuming multiplicative factors do not vary interannually, re-analysis used the multi-year mean of annual correction factors.

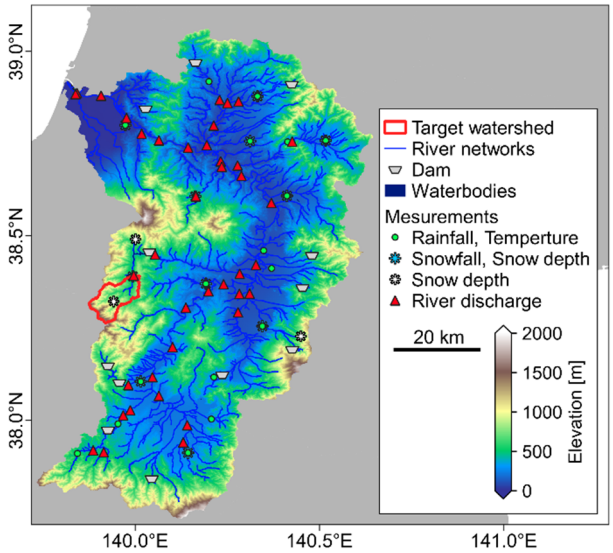


Fig. 1. Location of the study catchment and observation network within the Mogami River Basin

High spatiotemporal resolution analysis is required to reproduce Japan's long-term runoff characteristics, where steep topography creates high runoff coefficients. We applied the Rainfall-Runoff-Inundation (RRI) Model (Sayama et al., 2012), a distributed model simulating surface, subsurface, and groundwater flows. Calibration focused on August and September 2022—a snow-free period encompassing flood to low flows—to represent the rainfall-runoff process.

3 Results and discussion

Fig. 2 shows cumulative precipitation (partitioned into rain and snow), snowmelt, calculated and observed runoff, and snow water equivalent (SWE) for each correction scheme. **Fig. 2a)** represents the pre-correction state, where calculated

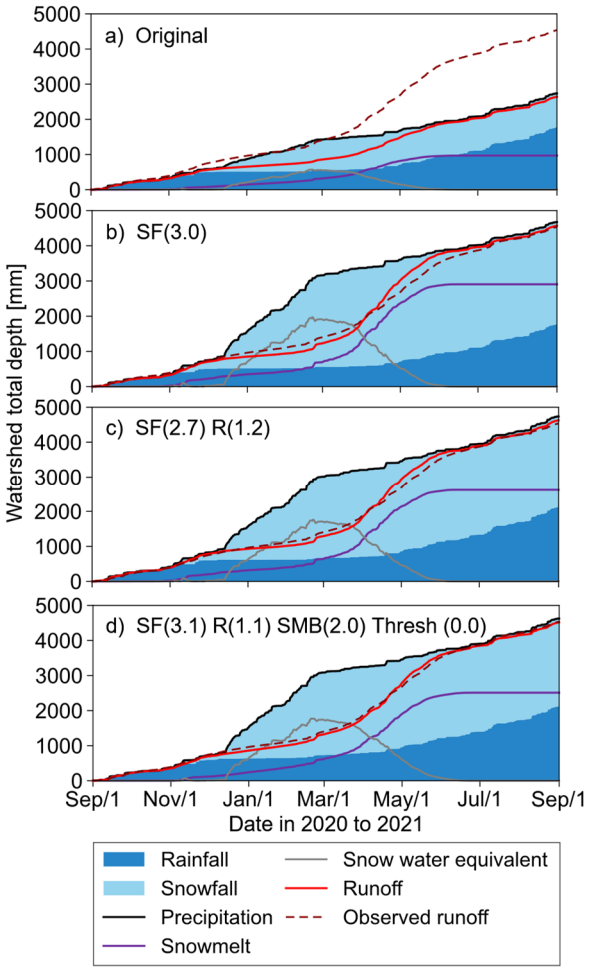


Fig. 2. Comparison of precipitation partitioning and runoff depth for (a) uncorrected, (b) snowfall-corrected, (c) rainfall- and snowfall-corrected, and (d) rainfall-, snowfall-, basal snowmelt-, and rain-snow threshold temperature-corrected conditions

annual runoff is deficient. To match annual total runoff, the snowfall multiplicative factor was set to 3.0 on average (**Fig. 2b**). Partitioning periods by snow accumulation and snowmelt presence, rainfall and snowfall multiplicative factors were calculated as 1.2 and 2.7, respectively (**Fig. 2c**). Although both match annual runoff, correcting rainfall reduced errors in runoff temporal variation. However, during the snowmelt period when SWE decreases, runoff depth is overestimated in early phases (April–May) and underestimated in late phases (June–July).

To improve accuracy, snow accumulation and snowmelt parameters were adjusted. In (c), during basal-snowmelt-dominated periods, the calculated cumulative runoff slope was half the observed slope; thus, the basal snowmelt rate of 2.0 mm day^{-1} was doubled to 4.0 mm day^{-1}. To reduce surface snowmelt overestimation, the rain-snow threshold temperature was set from 2 °C to 0 °C (**Fig. 2d**). Basal snowmelt underestimation was resolved, and reduced snowfall classification lowered SWE, mitigating early snowmelt overestimation.

Fig. 3 displays runoff depth temporal variations under each correction. Correcting rainfall reproduces summer flood peaks. Conversely, runoff depth remains overestimated

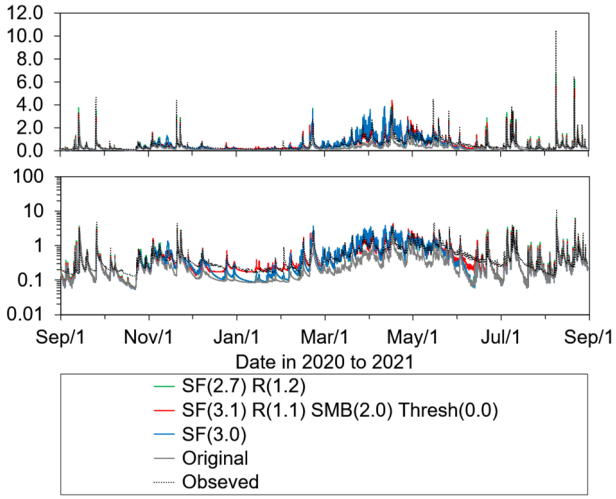


Fig. 3. Temporal variations of runoff depth under each correction scheme. SF, R, SMB, and Thresh denote snowfall, rainfall, basal snowmelt, and rain-snow threshold temperature, respectively; values in parentheses represent multiplicative factors.

during early snowmelt freshets and underestimated during late low flows. This occurs because the degree-hour method cannot model slope runoff delays caused by surface meltwater infiltration and refreezing within snowpacks. Incorporating solar radiation and wind speed for wide-area modeling remains challenging due to limited spatial representativeness; nevertheless, this study demonstrates the capabilities and limitations of temperature- and precipitation-based models.

4 Conclusions

To enable wide-area long-term runoff analysis using only precipitation and temperature inputs, this study corrected rain and snow data in a small catchment to match observed total runoff. Correcting both rainfall and snowfall improved temporal runoff reproducibility compared to correcting snowfall alone. Adjusting basal snowmelt and rain-snow threshold temperatures further enhanced performance during snow-dominated periods, demonstrating the potential and limits of temperature- and precipitation-based modeling. Determining the spatiotemporal distribution of multiplicative factors and model parameters (basal snowmelt rate and rain-snow threshold temperature) across wide areas remains a subject for future research.

Reference

[1] Kashiwa, S., Kazama, S., & Asaoka, Y. (2010). Estimation of Snowfall Distribution and Development of Distributed Snowmelt Runoff Model. *Advances in River Engineering*, *16*, 289–294.

[2] Sayama, T., Ozawa, G., Kawakami, T., Nabesaka, S., & Fukami, K. (2012). Rainfall–runoff–inundation analysis of the 2010 Pakistan flood in the Kabul River basin. *Hydrological Sciences Journal*, *57*(2), 298–312.

[3] Suzuki, H., Nakakita, E., & Takahashi, H. (2017). Accuracy of Radar-Raingauge Analyzed Precipitation: Analysis in Kanto, Koshin-Etsu, and Tohok Regions. *Journal of Japan Society of Civil Engineers, Ser. B1 (Hydraulic Engineering)*, *73*(4), I_13-I_18.

Global Classification of Extreme Precipitation Regimes

Irfans Maulana FIRDAUS[1*], Yusuke HIRAGA[1]
[1]Department of Civil and Environmental Engineering, Tohoku University, Miyagi 980-8579, Japan.
[*]E-mail: irfans.maulana.firdaus.d6@tohoku.ac.jp

Abstract

Extreme precipitation exhibits substantial spatial variability worldwide, posing challenges for understanding regional differences in the characteristics of extreme rainfall. Köppen–Geiger climate classification systems describe background climate conditions but do not explicitly characterize the statistical properties of precipitation extremes. This study develops a global classification of extreme precipitation regimes based on three characteristics of annual maximum daily precipitation: magnitude, interannual variability, and tail behavior. Daily precipitation data from MSWEPv2, CPC, and CHIRPSv2 are analyzed to examine the global distribution of extreme precipitation and classify regions according to these statistical properties. Return periods and corresponding return levels are estimated by fitting the generalized extreme value (GEV) distribution using the L-moments method. The results reveal spatial heterogeneity in extreme precipitation characteristics across the three datasets. The classification further identifies the Xe regime, characterized by erratic precipitation variability and an extreme tail, across parts of Asia, Africa, and South America. This regime accounts for 19.4% of the classified area in MSWEP, 15.7% in CPC, and 2.3% in CHIRPS2, demonstrating considerable dataset-dependent differences in its spatial extent. This classification complements the Köppen–Geiger climate classifications and provides a basis for investigating the spatial patterns of extreme precipitation and their potential changes under future climate scenarios.

Keywords: *Extreme precipitation, Return period, Return Level, Global regime map.*

1 Introduction

Extreme precipitation is a major component of the global hydrological cycle, with significant impacts on flooding, infrastructure, water resources, ecosystems, and society [1]. As climate change alters precipitation patterns, understanding the spatial and temporal characteristics of extreme precipitation has become increasingly important for hazard assessment and climate adaptation [2]. However, characterizing extreme precipitation at the global scale remains challenging due to its substantial spatial heterogeneity. Although the Köppen–Geiger classification [3] effectively represents background climate regimes based on temperature and precipitation patterns, it does not explicitly account for the recurrence characteristics of precipitation extremes. Therefore, a complementary classification framework is needed to better capture regional differences in extreme precipitation behavior.

This study aims to develop a global classification of extreme precipitation regimes based on the magnitude, interannual variability, and tail characteristics of annual maximum daily precipitation. By integrating these statistical properties into a unified framework, the proposed classification seeks to identify regions with distinct extreme precipitation behaviors and provide a more comprehensive understanding of their global distribution. This framework also provides a basis for investigating potential shifts in the spatial distribution and characteristics of extreme precipitation regimes under future climate change scenarios.

2 Materials and methods

2.1. Data

Daily precipitation over land is taken from (1) Multi-Source Weighted-Ensemble Precipitation, version 2 (MSWEP V2), (2) CPC Global Unified Gauge-Based Analysis of Daily Precipitation, and Climate Hazards Group InfraRed Precipitation with Station data (CHIRPS2) version 2 with specification of each dataset is presented in Table 1.

Table 1. Global coverage of daily precipitation.

Dataset	Version	Type	Temporal resolution	Grid resolution	Period	Source
1. MSWEP	v2.8	Gauge + Sat. + Rea.	Daily	0.1° × 0.1°	1979 – present	GloH2O
2. CPC	v1.0	Gauge	Daily	0.5° × 0.5°	1979 – present	NOAA CPC
3. CHIRPS*	v2.0	Gauge + Sat.	Daily	0.05° × 0.05°	1981 – present	UCSB/CHC

2.2. Return Period Calculation

We calculated the return period of each cell using the annual maximums series and it fitted to a GEV by L-Moments using approximation of Hosking [4]. The return period of a threshold z is $T = 1/[1 - F(z)]$.

2.3. Regime Classification

Each cell is calculated and described by three parameters: l_1, τ_2, τ_3 from L-Moments calculation. l_1 defines the magnitude of annual precipitation average, $\tau_2 = l_2/l_1$ defines the variability of each year, and $\tau_3 = l_3/l_2$ defines the tail extreme characteristic. We classify the regime by applying the threshold for each parameters. Table 2 shows the threshold that is used in this study.

Table 2. Regime classification threshold.

Parameter	Classes	Meaning	Threshold
l_1	Low, Medium, High	Magnitude	$25 < l_1 < 45$ $mm.day^{-1}$
τ_2	Steady, Intermediate, Erratic	Growth z_{100} from z_{10}	$1.45 < \tau_2 < 1.55$
τ_3	Moderate, Heavy, Extreme	Tail-shape	$0.236 < \tau_3 < 0.341$

3 Results and discussion

3.1. Return Period and Return Level

Figure 1 illustrates the global spatial distribution of the 50-

year return period (left panels) and the return level corresponding to a threshold $z = 50\ \mathrm{mm.day^{-1}}$ (right panels) across the three precipitation datasets. The return period maps show substantial spatial heterogeneity, with higher values generally occurring in tropical regions, while lower values dominate arid regions and high-latitude areas. The return level maps further reveal pronounced regional differences in the magnitude of extreme precipitation associated with a 50-year return period. Regions with higher return levels are represented by orange-to-red colors, whereas those with lower return levels are indicated by blue-to-green colors. These spatial contrasts suggest that regions with similar precipitation characteristics may exhibit substantially different extreme precipitation behavior, highlighting the importance of considering both precipitation magnitude and recurrence intervals when characterizing extreme events. Although the three datasets exhibit broadly consistent spatial patterns, differences in the local distributions of return periods and return levels indicate that dataset selection can influence the characterization of global precipitation extremes. Overall, these results underscore the importance of jointly examining return periods and return levels to obtain a more comprehensive understanding of global extreme precipitation patterns.

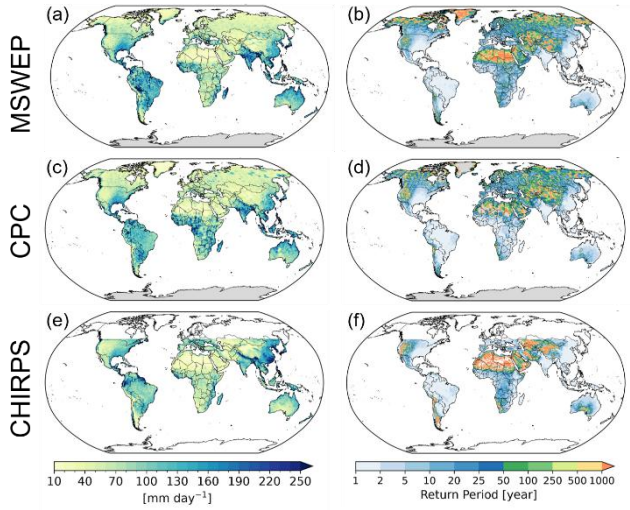


Fig. 1. (Left panel) Return period of 50 year for (a) MSWEP, (c) CPC, and (e) CHIRPS. (Right panel) Return level at $z = 50\ mm.day^{-1}$ for (b) MSWEP, (d) CPC, and (f) CHIRPS.

3.2. Regime Classification

Figure 2 presents the global classification of extreme precipitation regimes derived from (a) MSWEP, (c) CPC, and (e) CHIRPS, based on magnitude of annual precipitation average (l_1), variability (τ_2), and tail extreme characteristics (τ_3). Across the three datasets, the Xe regime, characterized by erratic precipitation variability and an extreme tail, exhibits distinct spatial patterns, particularly across parts of Asia, Africa, and South America. This regime accounts for 19.4% of the classified area in MSWEP, 15.7% in CPC, and only 2.3% in CHIRPS, highlighting substantial differences among datasets in their representation of regions with highly variable precipitation and pronounced extreme-tail behavior. The contrast is particularly evident in CHIRPS, in which the Xe regime occupies a considerably smaller proportion of the global classified area than in MSWEP and CPC. These differences indicate that dataset selection can affect the identification and spatial extent of extreme precipitation regimes, particularly those characterized by erratic variability and an extreme tail. By integrating precipitation magnitude, interannual variability, and tail characteristics, this classification identifies regions where extreme precipitation is not only intense but also varies considerably from year to year and exhibits a greater propensity for exceptionally large events. Thus, the proposed classification provides complementary information on extreme precipitation characteristics that may not be adequately represented by Köppen–Geiger climate classifications.

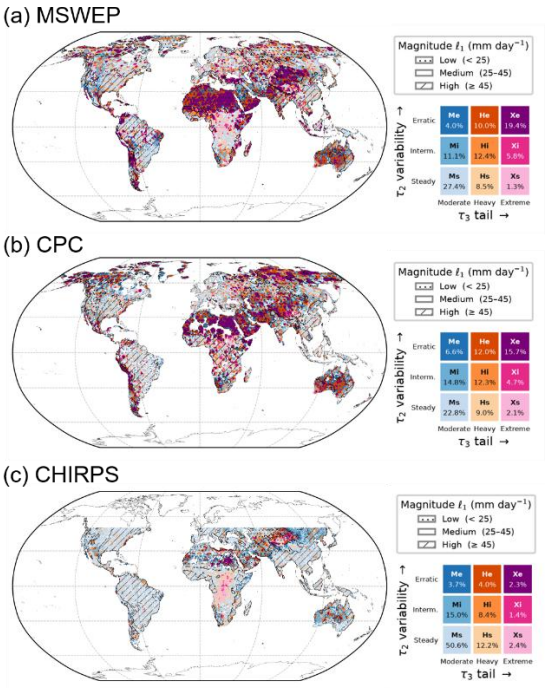


Fig. 2. Regime classification of (a) MSWEP, (c) CPC, and (e) CHIRPS.

4 Conclusions

This study presents a global classification of extreme precipitation regimes based on magnitude, interannual variability, and tail characteristics. The results reveal substantial spatial heterogeneity and differences among MSWEP, CPC, and CHIRPS, particularly in the extent of the Xe regime. This classification complements conventional climate classifications and provides a framework for understanding global extreme precipitation patterns and their potential changes under future climate scenarios.

Acknowledgement

This work was supported by JST FOREST Program, Japan Grant Number JPMJFR251Q.

Reference

[1] N. Teale and J. M. Winter, "The Relationship between Extreme Precipitation and Damaging Floods in the Northeastern United States," *J. Appl. Meteorol. Climatol.*, vol. 63, no. 9, pp. 1035–1047, 2024.

[2] H. Tabari, "Climate change impact on flood and extreme precipitation increases with water availability," *Sci. Rep.*, vol. 10, no. 1, p. 13768, 2020.

[3] M. Kottek, J. Grieser, C. Beck, B. Rudolf, and F. Rubel, "World Map of the Köppen-Geiger climate classification updated," *Meteorologische Zeitschrift*, vol. 15, no. 3, pp. 259–263, Oct. 2006.

[4] J. R. M. Hosking, "L-Moments: Analysis and Estimation of Distributions Using Linear Combinations of Order Statistics," *Journal of the Royal Statistical Society: Series B (Methodological)*, vol. 52, no. 1, pp. 105–124, Sep. 1990.

What Controls the Rainfall–Discharge Relationship? The Roles of Basin and Rainfall Characteristics Across Japan

○ Monton Methaprayun[1*], Yusuke Hiraga[1]
[1]Department of Civil Engineering, Tohoku University, Sendai, Japan.
[*]E-mail: methaprayun.monton.d7@tohoku.ac.jp.

Abstract

Rainfall is the primary driver of river discharge, yet similar rainfall amounts can produce markedly different discharge responses across catchments. These differences arise from basin properties, such as catchment area, slope, shape, and land use, and from rainfall spatial distribution. Understanding how these factors act, individually and in combination, is essential for identifying the mechanisms that govern catchment response. This study investigates how basin and rainfall characteristics control the rainfall–discharge relationship across Japan. Catchments were delineated for 1,226 discharge stations, from which 304 natural (dam-free) basins were selected. Hourly Radar-AMeDAS data from 1988 to 2024 were used to derive basin-averaged rainfall and to quantify its spatial variability. A Self-Organizing Map (SOM) was applied to the rainfall and discharge of each station to classify basins into groups with similar rainfall–discharge patterns. Each group was then interpreted using basin characteristics (catchment area, slope, basin shape, and land use) and rainfall spatial variability. This links the identified response patterns to their physical controls. A key focus is given to non-linear interactions between basin and rainfall characteristics, to identify the conditions under which rainfall produces amplified, proportional, or damped discharge responses. The findings advance understanding of the physical controls on rainfall–discharge relationships and the variability of flood responses, supporting improved hydrological prediction and flood risk assessment.

Keywords: rainfall-discharge relationship; catchment characteristics; rainfall spatial characteristics

1 Introduction

Rainfall is the primary driver of river discharge, yet the same amount of rainfall can produce very different flood responses in different catchments. Some basins produce sharp, high peaks. Others smooth out and delay the response. This variability makes flood prediction and design flood estimation harder, especially in ungauged basins. The response is shaped by static basin properties. Catchment area controls how much runoff is aggregated and attenuated, slope controls flow velocity, basin shape affects how flows from different parts of the catchment arrive together [1], and urban land use reduces infiltration. It is also shaped by the spatial distribution of each storm, that is, where rainfall falls relative to the outlet and how concentrated it is [2, 3]. These factors rarely act alone. The effect of rainfall spatial variability, for example, depends on catchment size and shape, so their combined effects are likely to be non-linear.

Catchment classification is a useful way to organize this diversity and link response behavior to physical controls [4]. The Self-Organizing Map (SOM) [5] is an unsupervised neural network that groups similar patterns without fixing their form in advance, and it has been widely applied in water resources [6]. Japan is a strong test case for this approach. Its rivers are short and steep, its basins vary widely, and its rainfall regimes produce contrasting spatial patterns. Long-term Radar-AMeDAS rainfall and a dense network of discharge stations make a nationwide analysis possible. This study uses SOM to classify 304 natural basins across Japan by their rainfall–discharge patterns. It then interprets each group using basin characteristics and rainfall spatial variability, to identify the conditions under which rainfall produces amplified, proportional, or damped discharge responses.

2 Materials and methods

Study area and data. Catchments were delineated for 1,226 discharge stations across Japan from the MERIT DEM [7], which has a resolution of 90 m. Of these, 922 basins regulated by dams were excluded, leaving 304 natural basins for analysis as shown in Fig. 1. Hourly discharge records were obtained from the Water Information System of the Ministry of Land, Infrastructure, Transport and Tourism (MLIT). Rainfall data came from the Radar-AMeDAS precipitation analysis of the Japan Meteorological Agency (JMA) for 1988–2024. The rainfall was averaged over each catchment to obtain hourly basin-averaged rainfall.

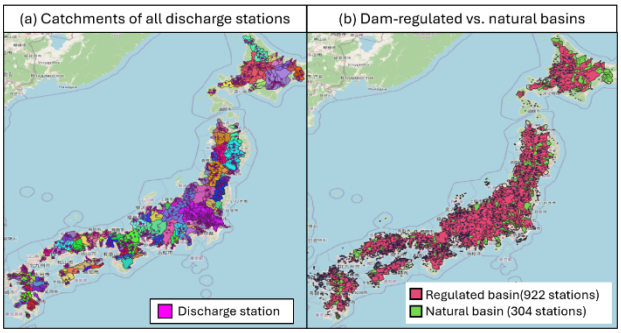


Fig. 1. (a) Catchments delineated for 1,226 discharge stations across Japan. (b) The 304 natural basins were selected for analysis.

Rainfall–discharge events. For each station, rainfall–discharge event pairs were extracted from the annual maximum discharge series. For each event, rainfall was accumulated over a window equal to the basin response time

preceding the discharge peak. Discharge was converted to specific discharge (discharge divided by catchment area) so that basins of different sizes could be compared directly.

Basin and rainfall characteristics. Four basin characteristics were calculated for each catchment: catchment area, mean slope, basin shape (Gravelius compactness coefficient, GC) [8], and land use. Rainfall spatial variability was characterized for each event using two indices based on the spatial moments of catchment rainfall [9]. D1 describes the location of rainfall relative to the basin outlet, and D2 describes the spatial dispersion of the storm.

SOM classification. A Self-Organizing Map (SOM) was used to classify stations by their rainfall–discharge behavior. Each station was represented by the normalized joint distribution of event rainfall and peak specific discharge. The SOM was trained on a network grid, and its nodes were grouped into clusters. Each cluster represents a distinct type of response.

3 Results and discussion

Specific peak discharge increases with rainfall depth, but at a given rainfall depth it varies by more than an order of magnitude (Fig. 2a). Much of this scatter reflects differences in climate between stations, since wetter stations produce both larger storms and larger floods. Normalizing each event by its station mean removes this effect, and the events then cluster around a near-proportional trend (Fig. 2b).

The SOM identified three response types (Fig. 3). In Group 1 (damped), large storms produce relatively smaller floods. In Group 2 (proportional), discharge scales almost one-to-one with rainfall. In Group 3 (amplified), a storm twice the station mean produces a peak discharge about three times the mean.

A single rainfall–discharge scaling therefore cannot represent all Japanese basins. Ongoing work is examining the non-linear interactions among basin and rainfall characteristics that control these response types.

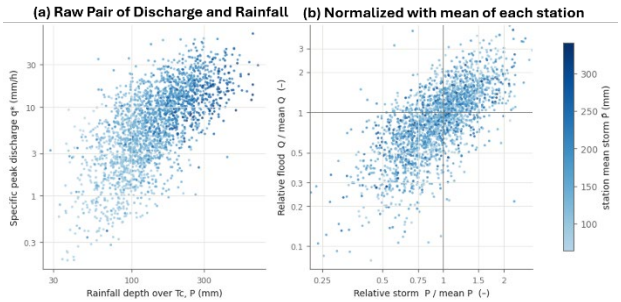


Fig. 2. Annual maximum rainfall–discharge event pairs. (a) Specific peak discharge and rainfall depth accumulated over the basin response time. (b) The same pairs, each normalized by its station mean.

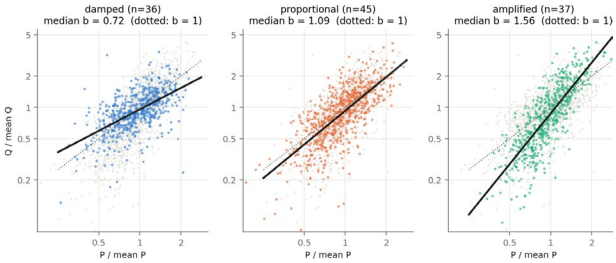


Fig. 3. Rainfall–discharge response types identified by the SOM classification: (a) damped, (b) proportional and (c) amplified.

4 Conclusions

Using SOM and Radar-AMeDAS rainfall, this study classified natural basins across Japan into three rainfall–discharge response types: damped, proportional, and amplified. These results indicate that flood magnitude does not scale uniformly with rainfall, which challenges the proportional assumption underlying design-storm practice. In amplified basins in particular, extreme rainfall may produce floods considerably larger than proportional scaling would predict. Ongoing work will quantify how basin and rainfall characteristics interact to control these response types, providing a basis for improved flood estimation and a better understanding of catchment response.

Reference

[1] Sassolas-Serrayet T, Cattin R, Ferry M, The shape of watersheds, Nature Communications, 9 (2018) 3791.

[2] Zoccatelli D, Borga M, Viglione A, Chirico GB, Blöschl G, Spatial moments of catchment rainfall: rainfall spatial organisation, basin morphology, and flood response, Hydrology and Earth System Sciences, 15 (2011) 3767-3783.

[3] Giani G, Rico-Ramirez MA, Woods RA, Are moments of rainfall spatial variability useful for runoff modelling in operational hydrology?, Hydrological Sciences Journal, 67 (2022) 1466-1479.

[4] Wagener T, Sivapalan M, Troch P, Woods R, Catchment classification and hydrologic similarity, Geography Compass, 1 (2007) 901-931.

[5] Kohonen T, Self-organized formation of topologically correct feature maps, Biological Cybernetics, 43 (1982) 59-69.

[6] Kalteh AM, Hjorth P, Berndtsson R, Review of the self-organizing map (SOM) approach in water resources: analysis, modelling and application, Environmental Modelling & Software, 23 (2008) 835-845.

[7] Yamazaki D, Ikeshima D, Tawatari R, Yamaguchi T, O'Loughlin F, Neal JC, Sampson CC, Kanae S, Bates PD, A high-accuracy map of global terrain elevations, Geophysical Research Letters, 44 (2017) 5844-5853.

[8] Sassolas-Serrayet T, Cattin R, Ferry M, The shape of watersheds, Nature Communications, 9 (2018) 3791.

[9] Zoccatelli D, Borga M, Viglione A, Chirico GB, Blöschl G, Spatial moments of catchment rainfall: rainfall spatial organisation, basin morphology, and flood response, Hydrology and Earth System Sciences, 15 (2011) 3767-3783.

Delineating Rainfall Homogeneous Regions for Japanese Class-A Watersheds Using the Spatial L-Moments (SLAM) Method: A Comparison with MLIT-Defined Regions

○ Wasitha DILSHAN[1*], Yusuke HIRAGA[1] & Daniel B. WRIGHT[2]
[1]Department of Civil and Environmental Engineering, Tohoku University, Miyagi 980-8579, Japan.
[2]Department and Environmental Engineering, University of Wisconsin-Madison, USA.
[*]E-mail: c4td9605@dc.tohoku.ac.jp

Abstract

Stochastic Storm Transposition (SST) estimates watershed-scale rainfall frequency by relocating observed storms within a transposition domain that is assumed to be homogeneous in extreme rainfall. In Japan, the regions defined by the Ministry of Land, Infrastructure, Transport and Tourism (MLIT) offer a ready-made domain, but they were drawn by expert judgement along administrative boundaries rather than tested for homogeneity. This study applies the Spatial L-Moments of Annual Maxima (SLAM) procedure to delineate a statistically homogeneous transposition domain for the Arakawa watershed using Radar-Rain Gauge Analyzed (RA) (1989–2025, March–November) and compares the resulting SST-based 48-hr rainfall frequency estimates with those obtained using the MLIT Hokuriku region. The SLAM domain (11,235 km^2, 9.7 times the watershed area) is about one quarter the size of the MLIT domain (40,660 km^2); 76.6% of it lies within the MLIT domain, but this shared area covers only 21.2% of the MLIT domain. The SLAM-based curve reproduces the observed annual maxima closely, whereas the MLIT-based curve is 12–17% lower for annual exceedance probabilities (AEPs) between 10^{-1} and 10^{-2}. At rare AEPs, the MLIT-based estimate reaches ~547 mm at AEP 10^{-4}, about 41% above the SLAM-based estimate (~388 mm). The two largest observed annual maxima lie above both curves but are consistent with the sampling variability of a 37-year record. SLAM thus offers an objective, reproducible and watershed-specific alternative to subjectively defined regional domains.

Keywords: Stochastic storm transposition; transposition domain; spatial L-moments; rainfall frequency analysis

1 Introduction

Rainfall estimates for rare events (AEP ≤ 10^{-2}) underpin flood-control planning and dam safety, yet at-site records are too short to constrain them. Stochastic Storm Transposition (SST) addresses this by randomly relocating observed storms from a surrounding region over the target watershed [1, 2]. Its central assumption is that the transposition domain is homogeneous, i.e., any storm observed within it could plausibly have occurred over the watershed [2]. In practice, domains are usually drawn by expert judgement, which is hard to reproduce.

In Japan, MLIT divides the country into regions with similar heavy-rainfall characteristics to set the maximum possible rainfall for inundation mapping [3]. These regions are natural SST domain candidates, but they are large, follow administrative boundaries, and were not designed as homogeneous regions in the sense of regional frequency analysis. A recent study, based on spatial L-moments [4] has tested the homogeneity of extreme-rainfall statistics around a target watershed and delineates the domain objectively. This study compares SLAM) domain for the Arakawa watershed, and the resulting SST rainfall frequency estimates, with those based on the MLIT-defined region.

2 Materials and methods

2.1 Study area and data.

The Arakawa watershed (≈1,160 km^2) drains the Iide and Asahi mountains into the Sea of Japan across Yamagata and Niigata prefectures, at the north-eastern edge of the MLIT Hokuriku region (Fig. 1). Hourly RA precipitation for 1989–2025 (37 years) was used. Only March–November was analyzed, excluding the snowfall-dominated winter months (December–February).

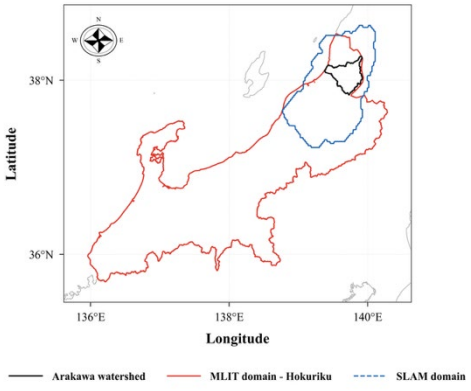


Fig. 1. Arakawa watershed, MLIT Hokuriku domain and SLAM-derived transposition domain.

2.2 SLAM domain.

For each candidate grid cell, the watershed polygon was centered on that cell, and the annual maxima of 48-hr watershed-average rainfall were computed. Their L-moment ratios were compared with those of the Arakawa watershed through a hypothesis test, with the false discovery rate controlled at a global significance level of 0.05 [4]. The

contiguous set of non-rejected cells around the watershed forms the SLAM domain.

2.3 SST rainfall frequency analysis.

Storm catalogs of the largest 48-hr storms were built from the same data for the SLAM domain and the MLIT Hokuriku domain and used in the RainyDay SST framework [1, 2]. Annual storm counts were drawn from a Poisson distribution, and storms were transposed uniformly within each domain over 100 realizations. Frequency curves (mean and range across realizations) were compared with the observed annual maximum series (AMS) at Weibull plotting positions.

3 Results and discussion

3.1 Shared domain area.

The SLAM domain covers 11,235 km^2 ($A_D/A_W = 9.7$), about 28% of the MLIT Hokuriku domain (40,660 km^2). The common area is 8,604 km^2, i.e., 76.6% of the SLAM domain but only 21.2% of the MLIT domain (Fig. 1). The domains agree on the core area around the watershed but differ in two respects. First, 23.4% (≈2,630 km^2) of the SLAM domain lies outside the MLIT boundary, to the north and east of the watershed, i.e., homogeneity extends across the Hokuriku–Western Tohoku administrative boundary. Second, almost 80% of the MLIT domain, extending up to ~400 km south-west to the Noto Peninsula and the Toyama–Fukui coast, was not identified by SLAM as homogeneous with Arakawa.

3.2 Rainfall frequency estimates.

For AEPs from 1 to 10^{-1}, the SLAM curve follows the bulk of the observed AMS (~200 mm at AEP 10^{-1}, against 207–211 mm observed), whereas the MLIT curve is lower (~176 mm, −12%) (Fig. 2). The gap widens to ~17% at AEP 2×10^{-2} (300 vs. 248 mm) and ~15% at 10^{-2} (332 vs. 283 mm), as storms from less intense, remote parts of Hokuriku dilute the local climatology. The curves cross at AEP ≈ 2.6×10^{-3} (~360 mm). Beyond this point, the MLIT estimate rises steeply to ~472 mm at 10^{-3} and ~547 mm at 10^{-4} (+25% and +41% relative to SLAM, ~377 and ~388 mm). The ranges across realizations are narrow (within ~±4%), so the differences reflect domain choice; the MLIT tail is dominated by a few intense remote storms.

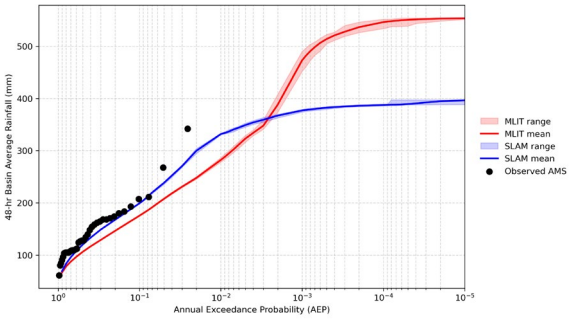


Fig. 2. 48-hr basin-average rainfall frequency curves for the Arakawa watershed from SST with the SLAM and MLIT domains (lines: mean; shading: range across realizations) and the observed AMS.

The two largest observed annual maxima (342 in 2022 and 268 mm in 2011; plot above both curves at Weibull AEPs of 1/38 and 2/38. The true AEP of the largest value in a 37-year record is highly uncertain: its 90% interval spans ~1.4×10^{-3} to 7.8×10^{-2}. The SLAM curve assigns 342 mm an AEP of ~7×10^{-3} (≈140-yr), well within this interval; the probability of at least one such event in 37 years is ~23%. The MLIT curve assigns it ~3×10^{-3} (≈300-yr; probability ~11%). Both events are thus rare but plausible outcomes of a short record, more consistent with SLAM. Such events may also reflect quasi-stationary rainbands aligned with the watershed, which random transposition rarely reproduces.

3.3 Strengths of SLAM over the MLIT classification.

First, SLAM is objective and reproducible: its domain results from an explicit hypothesis test at a stated significance level [4], not expert judgement. Second, SLAM is watershed-specific: one MLIT region serves all watersheds within it, so for Arakawa, at the region's edge, most of the domain is remote; SLAM centers the domain on the watershed and crosses administrative boundaries where rainfall statistics are homogeneous. Third, SLAM agrees better with observations, whereas the MLIT domain underestimates moderate and inflates rare quantiles. Finally, SLAM makes the trade-off between homogeneity and sample size explicit: its smaller catalog limits the rare-event tail (~400 mm), and the significance level can be tuned accordingly.

4 Conclusions

A SLAM-based transposition domain was delineated for the Arakawa watershed from 37 years of RA data and compared with the MLIT Hokuriku region. The SLAM domain is about one quarter the size of the MLIT domain, shares only 21.2% of it, and extends across the regional boundary where rainfall is homogeneous. It better reproduces the observed annual maxima, whereas the MLIT estimates have under-estimated RA based annual maxima at their lowest AEPs, showing that domain choice is a first-order source of uncertainty. Other Class-A watersheds and durations will be examined further.

Acknowledgement

This study was supported by the Kajima Foundation

References

[1] D.B. Wright, J.A. Smith, G. Villarini, M.L. Baeck, Estimating the frequency of extreme rainfall using weather radar and stochastic storm transposition, Journal of Hydrology, 488 (2013) 150–165.

[2] D.B. Wright, G. Yu, J.F. England, Six decades of rainfall and flood frequency analysis using stochastic storm transposition: Review, progress, and prospects, Journal of Hydrology, 585 (2020) 124816.

[3] Ministry of Land, Infrastructure, Transport and Tourism (MLIT), Method for setting the assumed maximum external force for preparing inundation assumptions (flood and inland water) (in Japanese), MLIT Water and Disaster Management Bureau, Tokyo (2015).

[4] B. FitzGerald, D.B. Wright, L. Yan, A. Hendricks Dietrich, A. Sebastian, An L-moments-based hypothesis test to identify homogeneous storm transposition regions, Journal of Hydrology, 675 (2026) 135617.

Quantifying the Climate Sensitivity of Atmospheric-River-Induced Extreme Precipitation Events

○ Francisco GIVOVICH[1*] & Yusuke HIRAGA[1]
[1]Department of Civil and Environmental Engineering, Tohoku University, Miyagi 980-8579, Japan.
[*]E-mail: givovich.diaz.francisco.antonio.s6@dc.tohoku.ac.jp

Abstract

Atmospheric rivers (ARs) are the dominant source of precipitation in the extratropical Andes of central Chile, yet how a changing climate affects their characteristics remains poorly understood. This study investigates the response of AR-driven heavy precipitation over central Chile to warming using the Pseudo Global Warming (PGW) method. Ten historical heavy precipitation events were simulated with the Weather Research and Forecasting (WRF) model forced by CFSR reanalysis, and perturbed with temperature and sea surface temperature changes from four CMIP6 models under SSP5-8.5 for mid-future (2041-2060) and late-future (2081-2100) periods. Events were divided into two equally sized groups according to the peak integrated water vapor transport (IVT) of their associated AR, and precipitation warming rates were compared with thermodynamic (precipitable water) and dynamic (vertical velocity) proxies. Mean precipitation warming rates followed Clausius-Clapeyron scaling in both groups, whereas variance was considerably larger in the Low IVT group, a pattern consistent with shifts in AR dynamics rather than moisture availability.

Keywords: climate modeling, atmospheric rivers, Pseudo Global Warming, extreme precipitation

1 Introduction

Atmospheric Rivers (ARs) are elongated, narrow corridors of enhanced water vapor and heat transport that predominantly originate over oceanic regions. They constitute a fundamental component of the global hydrological cycle and represent the primary mechanism for poleward moisture flux from the tropics to mid-latitude regions (Zhu & Newell, 1998). In the extratropical Andes of south-central Chile, landfalling ARs serve as the dominant source of precipitation, contributing approximately 50% of total annual accumulation (Viale et al., 2018).

The relationship between ARs and extreme precipitation events has been extensively documented across diverse geographical regions (Lavers & Villarini, 2013; Aguilera et al., 2019; Pradhan et al., 2025). These studies have consistently demonstrated the capacity of ARs to produce high-intensity rainfall and subsequent hydrometeorological hazards, underscoring their relevance as drivers of hydrological extremes at both regional and global scales.

However, despite the well-established understanding of climate change as an amplifying factor in heavy precipitation dynamics (Groisman et al., 1999), a notable gap remains in the literature regarding the implications of a changing climate on the characterization of ARs.

In this study, we propose a systematic ensemble modeling approach to investigate the effects of climate change on ARs over central Chile, employing the Pseudo Global Warming (PGW) method applied to a set of historical heavy precipitation events. Through the analysis of their properties, we seek to establish a relationship between AR characteristics and their susceptibility to changing climatic conditions.

2 Study area and data

Numerical experiments were conducted over the western slopes of the Andes using a three-domain nested configuration for the regional climate simulations. This modeling framework follows the domain configuration established by Hiraga & Meza (2025). A total of ten heavy precipitation events were selected from historical records derived from the CR2MET gridded precipitation product (Boisier et al., 2018). Event selection was based on a combination of 72-hour accumulation, temporal variability, and documented societal impact.

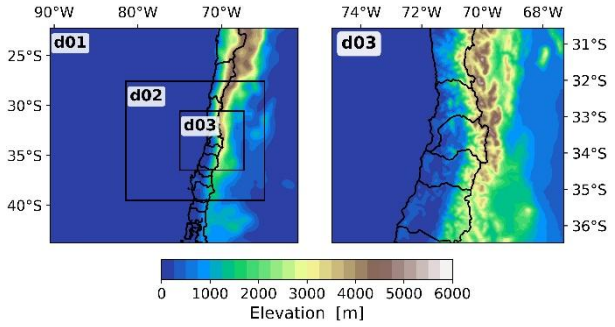


Fig. 1. Study area and nested domains considered.

All simulations were performed using the Advanced Research version of the Weather Research and Forecasting Model (WRF; Skamarock et al., 2008). Each simulation covers a 72-hour event period followed by a 72-hour post-event period, with nine spin-up configurations of 48, 54, 60, 66, 72, 78, 84, 90 and 96 hours considered to assess initialization sensitivity. Initial and boundary conditions were prescribed from the National Centers for Environmental Prediction (NCEP) Climate Forecast System Reanalysis (CFSR; Saha et al., 2010).

3 Methods

To simulate climate change conditions, the Pseudo Global Warming (PGW) method was employed, defined as:

$$X_{i,j,k} = X_{0_{i,j,k}} + \Delta X_{i,j,k}$$

where $X_{0_{i,j,k}}$ represents a grid-point value of a meteorological forcing variable (in this case, air temperature (T) and sea surface temperature (SST)), from CFSR, and $\Delta X_{i,j,k}$ denotes the perturbation term, calculated as the difference between a baseline and a target period. The baseline period corresponds to the recent historical climate (1991–2010), while two future target periods were considered: mid-future (2041–2060) and late-future (2081–2100). All climate projections were derived from four models presented in the Sixth Phase of the Coupled Model Intercomparison Project (CMIP6; Eyring et al., 2016), namely CMCC-CM2-SR5, EC-Earth3-Veg-LR, FGOALS-f3-L, and IPSL-CM6A-LR, under the high-emission Shared Socioeconomic Pathway SSP5-8.5.

4 Results and discussion

We divided the simulated precipitation events into two equally sized groups according to the peak integrated water vapor transport (IVT) intensity of their associated AR: a low IVT group and a high IVT group.

Figure 2 shows how the precipitation (P) warming rates differ between the two groups. We chose two variables as proxies for the components of the warming rate: vertical velocity (ω) as a proxy for dynamics, and precipitable water (PW) as a proxy for thermodynamics.

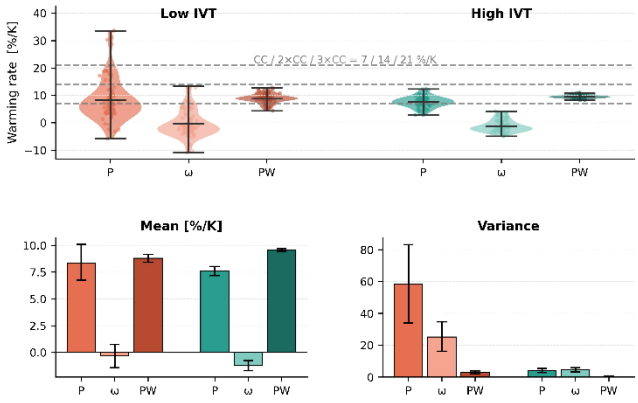


Fig. 2. Warming rate distributions of precipitation (P), vertical velocity (ω) and precipitable water (PW) for each IVT intensity group.

Although the mean P warming rates of both groups are similar and closely follow Clausius-Clapeyron (CC) scaling (~7%/K), the variance of the P warming rates in the Low IVT group is considerably higher than in the High IVT group. Mean PW warming rates show similar behavior, slightly exceeding CC scaling, but with little variance in either group. In contrast, mean ω values are slightly negative in both groups, and, like P, show a larger variance in the Low IVT group than in the High IVT group.

From these results, we attribute the difference between the PW and P warming rates to a dampening effect of dynamics in both IVT groups. Following this reasoning, we infer that the larger variance of P warming rates in lower-intensity events is better explained by the dynamic component of the associated AR events than by changes in available moisture. However, the large P variance also suggests that broader underlying processes may be involved.

5 Conclusions and future work

Following the premise of this study, we examined the effect of changing climatic conditions on AR characteristics, particularly peak IVT. We found that the Low IVT group has considerably more variance in its precipitation warming rates than the High IVT group, which could be explained by shifts in AR dynamics. However, to account for the influence of the complex topography of the Andes on the climate response, further analysis of the impacts on orographic precipitation and precipitation phase partitioning is needed.

References

[1] Aguilera, R., Gershunov, A., & Benmarhnia, T. (2019). Atmospheric rivers impact California's coastal water quality via extreme precipitation. *Science of the Total Environment, 671*, 488-494.

[2] Boisier, J. P., Alvarez-Garretón, C., Cepeda, J., Osses, A., Vásquez, N., & Rondanelli, R. (2018, April). CR2MET: A high-resolution precipitation and temperature dataset for hydroclimatic research in Chile. In *EGU General Assembly Conference Abstracts* (p. 19739).

[3] Eyring, V., Bony, S., Meehl, G. A., Senior, C. A., Stevens, B., Stouffer, R. J., & Taylor, K. E. (2016). Overview of the Coupled Model Intercomparison Project Phase 6 (CMIP6) experimental design and organization. *Geoscientific Model Development, 9*(5), 1937-1958.

[4] Groisman, P. Y., Karl, T. R., Easterling, D. R., Knight, R. W., Jamason, P. F., Hennessy, K. J., ... & Zhai, P. M. (1999). Changes in the probability of heavy precipitation: important indicators of climatic change. *Climatic Change, 42*(1), 243-283.

[5] Hiraga, Y., & Meza, J. (2025). Extreme precipitation modeling and probable maximum precipitation (PMP) estimation in Chile. *Journal of Hydrology: Regional Studies, 58*, 102274.

[6] Lavers, D. A., & Villarini, G. (2013). The nexus between atmospheric rivers and extreme precipitation across Europe. *Geophysical Research Letters, 40*(12), 3259-3264.

[7] Pradhan, S., Wasko, C., & Peel, M. C. (2025). Atmospheric rivers intensify extreme precipitation and flooding across Australia. *Weather and Climate Extremes*, 100812.

[8] Saha, S., Moorthi, S., Pan, H. L., Wu, X., Wang, J., Nadiga, S., ... & Goldberg, M. (2010). The NCEP climate forecast system reanalysis. *Bulletin of the American Meteorological Society, 91*(8), 1015-1058.

[9] Skamarock, W. C., Klemp, J. B., Dudhia, J., Gill, D. O., Liu, Z., Berner, J., ... & Huang, X. Y. (2019). A description of the advanced research WRF version 4. *NCAR Tech. Note NCAR/TN-556+STR, 145*(10.5065).

[10] Viale, M., Valenzuela, R., Garreaud, R. D., & Ralph, F. M. (2018). Impacts of atmospheric rivers on precipitation in southern South America. *Journal of Hydrometeorology, 19*(10), 1671-1687.

[11] Zhu, Y., & Newell, R. E. (1998). A proposed algorithm for moisture fluxes from atmospheric rivers. *Monthly Weather Review, 126*(3), 725-735.

Effects of Low-intervention Channel Management on Aquatic Insect HSI under Future Climate

○ Keita KUBO[1*], So KAZAMA[1] , Kei NUKAZAWA[2]

[1]Department of Civil Engineering, Tohoku University, Miyagi 980-8579, Japan.
[2]Department of Civil and Environmental Engineering, University of Miyazaki, Miyazaki, Japan
[*]E-mail: kubo.keita.r6@dc.tohoku.ac.jp.

Abstract

Low-intervention channel management has been proposed for depopulating small river basins in Japan, but its effects on river biota under future climate remain unclear. We coupled a distributed runoff–water temperature model with a habitat suitability index (HSI) model for 23 aquatic insect families and compared two management scenarios, an unmanaged vegetated channel and bank removal, under RCP2.6 and RCP8.5 in 2090. In the Sukawa River basin, annual maximum water temperature exceeded the upper limit of the suitable range of the model (21 °C), and the mean number of families with HSI > 0 decreased from 3.45 under the current climate to 0.22–0.26 under RCP8.5. For 14 families with wide occurrence temperature ranges in a warmer region (Kyushu), a non-thermal HSI indicated that bank removal retained more suitable habitat than the unmanaged channel by moderating flood depth.
.

Keywords: aquatic insects, habitat suitability index, climate change, thermal tolerance range

1 Introduction

Depopulation in upstream areas of Japan is making the maintenance of small river facilities increasingly difficult. Chiba and Kazama[1)] proposed low-intervention management, in which channel maintenance is deliberately abandoned and the storage effects of forests and floodplains are exploited. Although this can be regarded as ecosystem-based adaptation, its benefit to river biota is uncertain: our previous study[2)] showed that increased flood depth under such management can reduce habitat suitability for aquatic insects even under the current climate. Under future climate, warming and more intense floods may act simultaneously. This study evaluates how aquatic insect habitat suitability responds to low-intervention management under future climate, and which families may retain habitat when the thermal range of an existing HSI model is exceeded.

2 Materials and methods

2.1 Study basins and climate data

The study basins are the Sukawa (72.6 km^2), Ohtani (48.6 km^2) and Dangosawa (3.1 km^2) rivers in Yamagata and Fukushima Prefectures (Fig. 1), where the population is projected to approach zero after 2080; 2090 was therefore selected as the target year. Hourly 2-km outputs of the regional climate model NHRCM-2km for RCP2.6 and RCP8.5 (four members each) were bias-corrected by quantile mapping against AMeDAS observations. The models were run for each member and the results were averaged. The year 2022 was used as the current climate.

2.2 Hydrological model and management scenarios

Discharge, depth, velocity and water temperature were simulated at 100-m and hourly resolution using a distributed runoff model[1)] coupled with a heat-budget water temperature model[2)]. Assuming that the depopulated basins become fully forested, two low-intervention scenarios were set (Fig. 2): an unmanaged channel (UC), in which vegetation encroachment

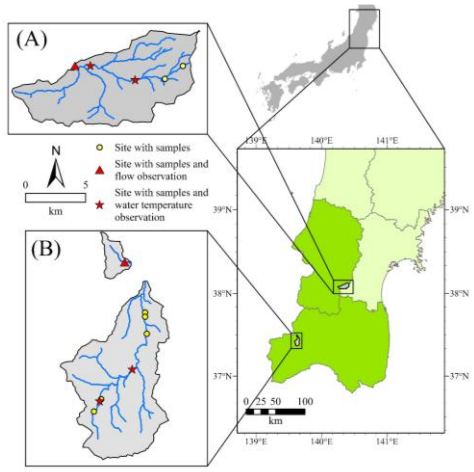


Fig. 1 Study basins.(A)Sukawa, (B)Ohtani and Dangosawa.

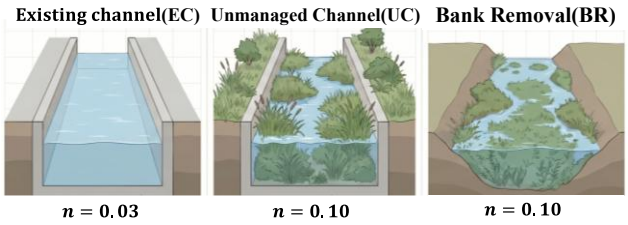


Fig. 2 Channel management scenarios.

raises Manning's roughness from 0.03 to 0.10 while the rectangular revetted section is retained, and bank removal (BR), in which revetments are removed and the section becomes triangular with the same roughness. The existing channel (EC; rectangular, n = 0.03) was used for comparison.

Discharge, depth, velocity and water temperature were simulated at 100-m and hourly resolution using a distributed runoff model[1)] coupled with a heat-budget water temperature model[2)]. Assuming that the depopulated basins become fully forested, two low-intervention scenarios were set (Fig. 2): an

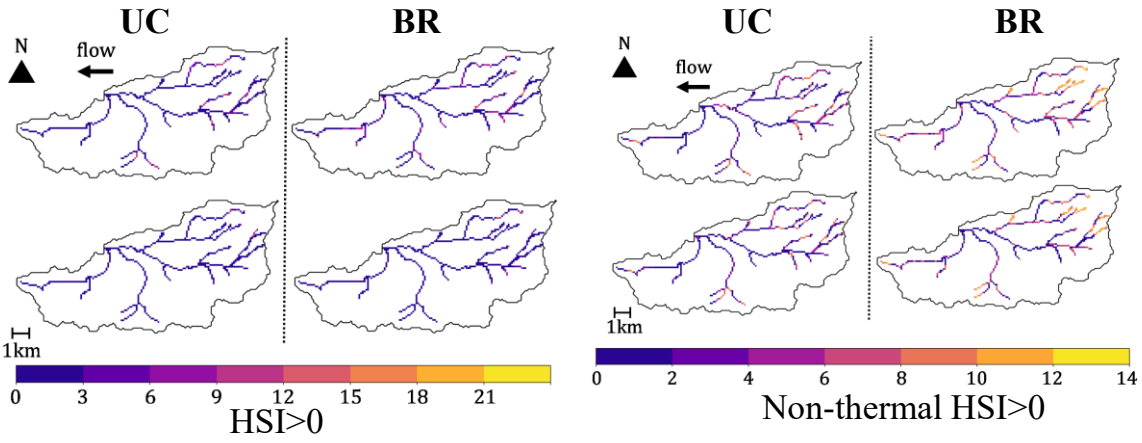


Fig. 3 Number of families with (a) HSI > 0 and (b) non-thermal HSI > 0 (WTG) in the Sukawa basin. left: UC, right: BR; top: RCP2.6, bottom: RCP8.5.

unmanaged channel (UC), in which vegetation encroachment raises Manning's roughness from 0.03 to 0.10 while the rectangular revetted section is retained, and bank removal (BR), in which revetments are removed and the section becomes triangular with the same roughness. The existing channel (EC; rectangular, n = 0.03) was used for comparison.

2.3 HSI model and thermal-range grouping

Habitat suitability was evaluated using the HSI model developed for the Natori River basin[3], which combines suitability indices (SI, 0–1) for 14 environmental variables (land use, slope, urbanization, distances to urban area and forest, and annual mean, maximum and minimum depth, velocity and water temperature) by their geometric mean. Because any SI = 0 gives HSI = 0, we counted the families with HSI > 0 among 23 families recorded in the study basins. To interpret temperature-driven losses, we used presence data of 36 families at 81 sites in the Omaru River basin, Kyushu[4], where the mean annual air temperature is 4–6 °C higher than in the study region, comparable to the RCP8.5 warming. Following Dewenter et al.[5], the occurrence temperature range of each family was defined as the difference between the maximum and minimum water temperatures at its occurrence sites, and families above the median (6.5 °C) were classified as the wide thermal-range group (WTG). For the WTG, a non-thermal HSI was computed from the 11 variables excluding water temperature.

3 Results and discussion

3.1 Loss of HSI under future warming

Across the three basins and all scenarios, annual maximum water temperature exceeded 21 °C, above which SI = 0 for all families, in 57.7% and 94.2% of channel cells under RCP2.6 and RCP8.5, by 2.7 and 3.4 °C on average. Consequently, the mean number of families with HSI > 0 in the Sukawa basin decreased from 3.45 (current climate, EC) to 0.83 (UC) and 1.76 (BR) under RCP2.6, and to 0.22 and 0.26 under RCP8.5 (Fig. 3a). BR reduced the loss under RCP2.6, but the difference almost vanished under RCP8.5. These zero values arise largely from extrapolation beyond the temperature range used to build the model and should not be read directly as local extinction.

3.2 Non-thermal HSI of wide thermal-range group

Of the 23 families, 14 were classified as the WTG, including all four Ephemeroptera families, whereas two of the three Plecoptera families fell into the narrow group, consistent with the reported thermal vulnerability of stoneflies[5]. For the WTG, the mean number of families with non-thermal HSI > 0 was 5.43 under the current climate (EC), and 1.97 (UC) and 3.92 (BR) under RCP2.6 and 1.79 and 3.13 under RCP8.5 (Fig. 3b). In UC, the increased roughness lowered velocity but greatly raised the annual maximum depth (e.g., 2.46 m vs 0.65 m for EC in the Ohtani River under RCP2.6), whereas BR limited it to 1.34 m. Suitable cells were concentrated in the headwaters in all scenarios, suggesting that even warm-tolerant taxa may be confined upstream by flow conditions.

4 Conclusions

Under the 2090 climate, annual maximum water temperature exceeded the thermal range of the existing HSI model, and HSI-based suitability almost disappeared regardless of management, highlighting the limitation of models built under the current climate. For families with wide occurrence temperature ranges, bank removal retained more suitable habitat than leaving channels unmanaged by moderating flood depth, under idealized channel conditions without bed deformation.

References

[1] Chiba, K. and Kazama, S.: Assessment of changes in the flow of small river basins due to depopulation using a distributed runoff model, J. JSCE B1, Vol.78, No.2, pp.535–540, 2022.

[2] Kubo, K., Inoshita, Y., Kazama, S. and Hiraga, Y.: Analysis of depopulation-induced land use and river channel changes on species diversity in small rivers, J. JSCE, Vol.82, No.16, 25-16014, 2026.

[3] Nukazawa, K., Kazama, S. and Watanabe, K.: Catchment-scale modeling of riverine species diversity using hydrological simulation, Ecohydrology, Vol.10, No.1, e1778, 2017.

[4] Nukazawa, K., Tanaka, R. and Mineda, H.: Importance of flow metrics on modeling macroinvertebrate community in dammed rivers, Ecol. Evol., Vol.15, No.10, e72411, 2025.

[5] Dewenter, B. S. et al.: The thermal breadth of temperate and tropical freshwater insects supports the climate variability hypothesis, Ecol. Evol., Vol.14, e10937, 2024.

Analysis of the Spatiotemporal Characteristics of Extreme Precipitation Using the Japanese Long-term Regional Reanalysis Dataset RRJ-Conv

○Sachio IWABU[1], Yusuke HIRAGA[1], Ryotaro TAHARA[1]
[1]Graduate School of Engineering, Tohoku University, Miyagi 980-8579, Japan.
• *E-mail: iwabu.sachio.q6@dc.tohoku.ac.jp.

Abstract

The characteristics of extreme precipitation vary depending on meteorological drivers, and corresponding differences in the tail behavior of probability distributions have been reported. In this study, the Japanese long-term regional reanalysis dataset RRJ-Conv was used to identify annual maximum 24-hour precipitation events across 109 major river systems in Japan. The rainfall patterns were classified using a self-organizing map (SOM) and the K-means method. The cluster composition of all annual maximum events was compared with that of the upper tail, and cluster-specific extreme-value distributions were evaluated for four representative river systems. The results revealed regional differences in rainfall-pattern diversity and in the patterns dominating the upper tail. The cluster composition of all annual maximum events did not necessarily correspond to that of the upper tail. Furthermore, differences in the upper tails of the cluster-specific extreme-value distributions were observed. These findings highlight the importance of considering rainfall spatial patterns and their associated extreme-value characteristics when evaluating extreme precipitation.

Keywords: RRJ-Conv; extreme precipitation; self-organizing map; 109 major river systems.

1 Introduction

Accurately characterizing the frequency of extreme precipitation is essential for river planning and flood risk assessment. Heavy rainfall occurs under different meteorological conditions, such as typhoons and frontal systems, and its spatiotemporal distribution and intensity vary accordingly. Tanaka et al. [1] demonstrated that the tail behavior of extreme-value distributions differs between typhoon-related and non-typhoon-related precipitation. This suggests that differences in rainfall spatial patterns should also be considered when evaluating extreme precipitation. Rather than directly classifying rainfall events by their meteorological causes, this study focuses on rainfall spatial patterns. The objectives are to clarify (1) regional differences in rainfall-pattern diversity and tail dominance and (2) differences in extreme-value distributions among rainfall-pattern clusters across 109 major river systems in Japan using RRJ-Conv.

2 Materials and methods

This study used RRJ-Conv, a Japanese long-term regional reanalysis dataset developed by the Japan Meteorological Agency and Tohoku University [2]. The dataset provides meteorological fields at an approximately 5-km grid spacing and hourly intervals from 1959 to 2022. The analysis covered 109 major river systems in Japan, with June–November selected as the analysis period for each year.

The 24-hour precipitation at each grid cell was normalized by the basin-averaged 24-hour precipitation, and grid cells with normalized values of 1.2 or greater were defined as rainfall areas. These areas were identified using eight-neighbor connectivity, and their spatial patterns were classified using a 10 × 10-node SOM trained for 10,000 iterations. The resulting 100 SOM nodes were then grouped into four clusters using the K-means method. Rainfall-pattern diversity was evaluated using normalized Shannon entropy based on the occurrence proportions of the clusters. For the 64 annual maximum 24-hour precipitation events in each river system, events with an empirical non-exceedance probability of 0.95 or greater were defined as the upper tail. The cluster occurring most frequently among these upper-tail events was defined as the tail-dominant cluster.

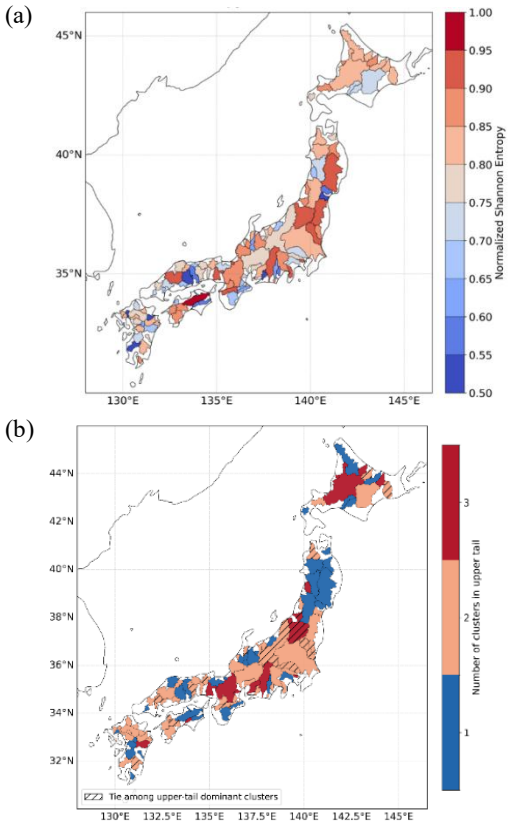


Fig. 1. (a) Diversity of rainfall patterns and (b) tail dominance across the 109 river systems in Japan.

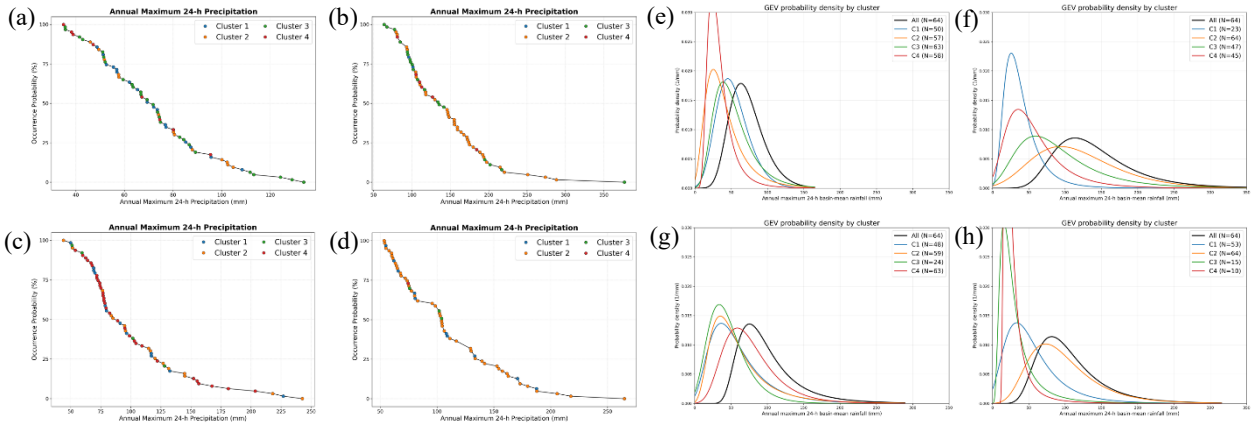


Fig. 2. Hazard curves and cluster-specific GEV distributions for four representative river systems: (a)–(d) hazard curves for the Kitakami, Tama, Yodo, and Takahashi River systems, respectively; (e)–(h) fitted GEV distributions for the Kitakami, Tama, Yodo, and Takahashi River systems, respectively.

Four representative river systems—the Kitakami, Tama, Yodo, and Takahashi river systems—were further analyzed. Hazard curves of annual maximum 24-hour precipitation were constructed, and individual events were distinguished by color according to their assigned clusters. In addition, a generalized extreme value (GEV) distribution was fitted to the annual maximum 24-hour precipitation values belonging to each cluster to compare the extreme-value distributions among rainfall patterns.

3 Results and discussion

3.1 Rainfall-Pattern Diversity and Tail Dominance

The comparison of 109 river systems revealed regional differences in rainfall-pattern diversity for annual maximum 24-hour precipitation. Evaluation using normalized Shannon entropy identified river systems in which multiple clusters occurred with relatively even proportions and those in which a particular cluster predominated (Fig. 1).

The cluster composition of all annual maximum events did not necessarily correspond to that of the upper tail. Although diverse rainfall patterns occurred among all annual maximum events, a particular cluster dominated the upper-tail events in some river systems. This indicates that the occurrence frequencies of rainfall patterns across all annual maximum events alone may not adequately characterize the rainfall patterns associated with extreme precipitation events.

3.2 Comparison of Hazard Curves and Cluster Specific GEV Distributions in Representative River Systems

For four representative river systems, annual maximum precipitation values on the hazard curves were compared by cluster, and GEV distributions were fitted to the annual maximum precipitation samples for each cluster. The results revealed differences among river systems in both the clusters contributing to extreme precipitation events and the tail characteristics of cluster-specific probability distributions (Fig. 2(a)–(h)).

In the Kitakami River system, Cluster 3 dominated the upper tail of the hazard curve (Fig. 2(a)). The GEV distributions also showed substantial differences in their upper tails, with Clusters 3 and 1 being strongly associated with extreme precipitation events, in that order. In contrast, the precipitation distributions of Clusters 2 and 4 were concentrated at relatively lower precipitation amounts (Fig. 2(e)). In the Tama River system, Cluster 2 appeared frequently in the upper portion of the hazard curve (Fig. 2(b)), and differences among clusters were also evident in their GEV distributions. In particular, Cluster 2 was strongly associated with extreme precipitation events (Fig. 2(f)).

In the Yodo River system, multiple clusters appeared in the upper tail of the hazard curve, indicating diverse rainfall patterns rather than dominance by a single cluster (Fig. 2(c)). The GEV distributions also exhibited characteristic differences in the extent of their upper tails (Fig. 2(g)). In the Takahashi River system, Cluster 2 appeared frequently across a broad range of the hazard curve and dominated its upper tail (Fig. 2(d)). Furthermore, the GEV distribution for Cluster 2 was broadly consistent with the distribution fitted to all annual maximum precipitation events (Fig. 2(h)).

These results indicate that rainfall-pattern diversity and the patterns dominating the upper tail vary among river systems, suggesting that the cluster composition of all annual maximum events alone may not be sufficient to fully characterize the rainfall patterns contributing to the upper tail. Furthermore, the analysis of the representative river systems revealed differences in the upper tails of cluster-specific GEV distributions (Fig. 2(e)–(h)). Therefore, when evaluating extreme precipitation, it is important to consider not only the entire annual maximum precipitation series as a single probability distribution but also the diversity of rainfall patterns and the patterns represented in the upper tail.

Reference

[1] Tanaka, T., Abe, J., Hiraga, Y., Kitano, T., and Sayama, T. (2026). Analysis of the Tail Characteristics of Generalized Extreme Value Distributions for Typhoon-Related and Non-Typhoon-Related Extreme Precipitation. *Journal of Japan Society of Civil Engineers*, 82(16), 25-16057.

[2] Fukui, S., Shirakawa, E., Soga, D., Ohara, R., Usui, K., Takiguchi, K., Ono, K., Hirose, T., Matsushima, S., Ito, J., Yamazaki, T., Saito, K., Seko, H., and Iwasaki, T. (2024). Long-term regional reanalysis for Japan with assimilating conventional observations (RRJ-Conv). *Journal of the Meteorological Society of Japan*, 102(6), 677–696.

Nationwide Assessment of Flood Retention Measures Utilizing Agricultural Land

○ Haruki TAMAKAWA[1*], Tomoaki MATSUURA[1], Atsuya IKEMOTO[1], Tsuyoshi TADA[2] & So KAZAMA[1]

[1]Department of Civil and Environmental Engineering, Graduate School of Engineering, Tohoku University, Miyagi 980-8579, Japan.

[2]Department of Civil and Environmental Engineering, National Defense Academy, Kanagawa 239-8686, Japan.

[*]E-mail: tamakawa.haruki.r1@dc.tohoku.ac.jp

Abstract

To quantify the flood control benefits of using farmland in middle reaches as flood retention areas, we identified uninhabited farmland along middle-stream rivers across Japan and conducted nationwide flood inundation simulations and flood damage estimation assuming that floodwater is guided into these areas. Approximately 2,468 km^2 of suitable land was identified nationwide. Using these areas as retarding basins was estimated to reduce the nationwide expected annual damage (EAD) by 2.5% (65.7 billion JPY/year) under the current climate. By river system, high reduction rates were found in the Iwaki River (23.2%) and the Shinano River (21.1%), and the Tone River showed the largest reduction of approximately 18.2 billion JPY/year. Although the damage reduction increased with flood magnitude from 1.4 trillion JPY (30-year event) to 3.9 trillion JPY (200-year event), the reduction rate was identical for the 100- and 200-year events (2.9%), indicating that the effect plateaus for large floods as the storage capacity becomes saturated.

Keywords: river flood; farmland; retarding basin; flood adaptation; nationwide assessment.

1 Introduction

Global warming is increasing the frequency and intensity of heavy rainfall worldwide [1], and extreme floods are projected to become more frequent in many regions, including Asia [2]. As levees alone cannot fully cope with intensifying rainfall, restoring the natural retention function of floodplains has attracted attention; in Europe, retention areas were shown to be more cost-effective than levee strengthening or land-use regulation [3]. In Japan, basin-wide flood management (Ryuiki Chisui) has become the core concept, and strategic flood inundation that guides overflow toward areas with fewer assets has been proposed [4]. However, no study has identified the spatial distribution of suitable sites at the national scale and quantified the resulting flood control effects.

This study therefore evaluates, through nationwide numerical simulation, the flood damage reduction potential of retarding basins utilizing farmland in middle reaches, prior to cost–benefit analysis.

2 Materials and methods

2.1 Flood inundation analysis and data

Flood inundation was simulated with a two-dimensional model using an eight-neighborhood connected collocated grid scheme [5] at a 250 m resolution, applied uniformly to river channels and floodplains over all of Japan. Probabilistic flood-contributing rainfall distributions, which produce extreme discharges of equal probability at any river point [6], were given for return periods of 10, 30, 50, 100 and 200 years. Present flood protection levels were reflected by lowering channel elevations following Yanagihara et al. [7]. National Land Numerical Information (land use, elevation, population), the nationwide Strahler stream order dataset [8] and a database of existing retarding basins in Japan [9] were used.

2.2 Selection of suitable sites

Cells satisfying all of the following conditions were extracted as suitable sites: (a) adjacent to rivers of stream order 4–7, along which all existing agricultural retarding basins are located [9]; (b) uninhabited (population < 1 per 250 m cell); (c) containing paddy fields, other farmland or wasteland, and no building land, sea, beach, golf course or other land use; and (d) a maximum inundation depth of at least 0.12 m in the 200-year flood, which is the minimum simulated depth among existing paddy-type retarding basins (Kariyata River retarding basin). Neighboring cells satisfying (b)–(d) were then added to give the sites spatial extent.

2.3 Representation of retarding basins

Following the Ichinoseki retarding basin, where farming continues with overflow about once per 10 years, the ground elevation of each suitable cell was set to the elevation of the adjacent channel plus its 10-year flood depth, so that floodwater begins to flow into the site only when a flood exceeds the 10-year level (mean lowering 3.77 m; median 1.95 m). This is a screening assumption, not an excavation plan; ring levees and overflow weirs were not considered.

2.4 Flood damage estimation

Direct damage to paddy fields, other farmland, business establishments, residences and golf courses was estimated following the Manual for Economic Investigation of Flood Control (MLIT). The EAD was obtained from the 30- to 200-year events and compared with and without the retarding basins, including damage within the sites.

3 Results and discussion

3.1 Suitable sites and nationwide damage reduction

About 2,468 km^2 of suitable land (0.58% of basin area on average; up to 5.5% in the Iwaki River) was extracted, whereas none existed in three urbanized systems (Tama, Tsurumi and Doki Rivers).

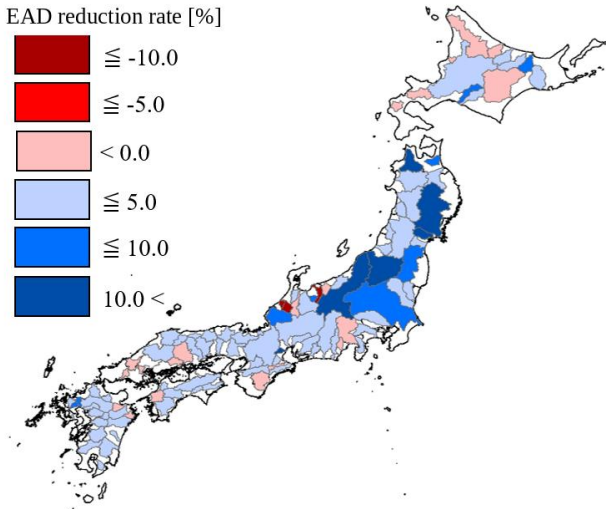


Fig. 1. EAD reduction rate by retarding basins for each class-A river system.

The EAD was reduced by 65.7 billion JPY/year, or 2.5% nationwide (Fig. 1). The highest reduction rates occurred in the Iwaki (23.2%), Shinano (21.1%), Agano (17.4%), Naruse (14.4%) and Kitakami (13.9%) River systems, and 45 of 109 class-A systems exceeded 1%. In contrast, nine systems showed increases, e.g. the Kakehashi (−28.5%) and Kurobe (−17.7%) Rivers, where inundation spread into the hinterland because ring levees were not modeled.

3.2 Effect of flood magnitude

The damage reduction increased with flood magnitude from 1.4 trillion JPY (30-year) to 3.9 trillion JPY (200-year), whereas the reduction rate rose from 1.9% to 2.9% and became identical for the 100- and 200-year events (Fig. 2). Inflow is limited in moderate floods, while in large floods the basins reach their storage limit. In 13 systems (e.g. Teshio, Tokachi), damage increased in the 30-year but decreased in the 200-year flood, suggesting basin-specific optimization of the inflow frequency.

3.3 Regional differences and controlling factors

Storage volume correlated only weakly with the EAD reduction (R^2 = 0.29; Fig. 3). The Tone River achieved the largest reduction (18.2 billion JPY/year), whereas the Ishikari River, with the largest storage volume (0.78 billion m^3), achieved only 0.66 billion JPY/year. Residential damage fell greatly in the Tone, Shinano and Arakawa systems but little in the Teshio, Mogami and Ishikari. In the Ishikari River, assets are concentrated along the Toyohira River tributary, where little farmland is available upstream. Thus, sites upstream of asset concentrations are key.

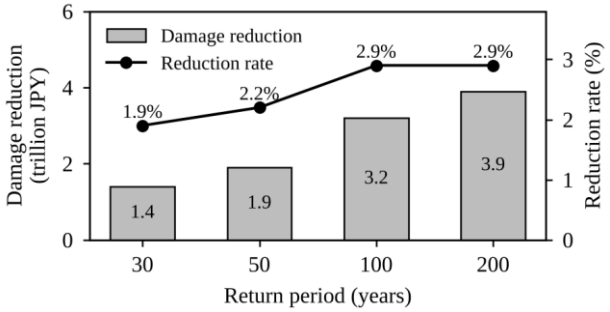


Fig. 2. Nationwide damage reduction and reduction rate by return period.

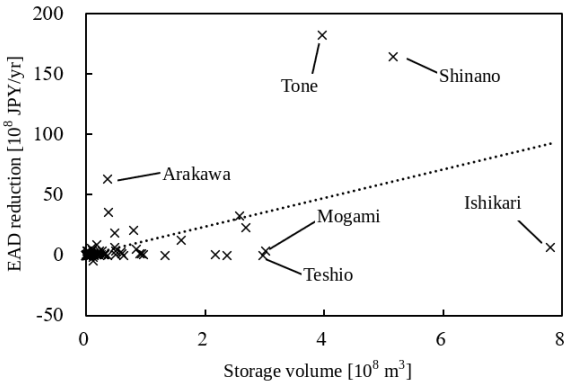


Fig. 3. Relationship between storage volume and EAD reduction for each river system.

4 Conclusions

About 2,468 km^2 of suitable farmland was identified, which could reduce the nationwide EAD by 2.5% (65.7 billion JPY/year). The reduction rate plateaued at 2.9% for 100- and 200-year floods owing to storage saturation, and the effect depended on site location relative to downstream assets rather than on storage volume. Modeling levees and assessing agricultural sustainability remain future work.

Acknowledgements: This research was supported by ERCA (JPMEERF25S12422) and JSPS KAKENHI (24H00329, 23K26202).

Reference

[1] IPCC, Climate Change 2021: The Physical Science Basis. Cambridge University Press (2021).
[2] R. Dankers et al., First look at changes in flood hazard in the Inter-Sectoral Impact Model Intercomparison Project ensemble, Proc. Natl. Acad. Sci., 111(9) (2014) 3257-3261.
[3] F. Dottori et al., Cost-effective adaptation strategies to rising river flood risk in Europe, Nat. Clim. Change, 13(2) (2023) 193-200.
[4] T. Ishikawa, Strategic flood inundation for future extreme floods, J. Jpn. Soc. Hydrol. Water Resour., 33(6) (2020) 263-270. (in Japanese)
[5] T. Tada, An eight-neighborhood connected collocated grid scheme for overland flow simulation, Hydrol. Res. Lett., 20(2) (2026) 113-118.
[6] T. Matsuura et al., Spatial estimation of extreme rainfall and extreme discharge and quantitative assessment of flood risk across Japan, J. JSCE, 81 (2025) 25-00171. (in Japanese)
[7] H. Yanagihara et al., Nationwide evaluation of changes in fluvial and pluvial flood damage and the effectiveness of adaptation measures in Japan under population decline, Int. J. Disaster Risk Reduct., 110 (2024) 104605.
[8] T. Yamamoto, T. Tada, S. Kazama, Datasets of Strahler stream order and flood plain masks in Japan, J. Jpn. Soc. Hydrol. Water Resour., 36(4) (2023) 297-305. (in Japanese)
[9] Y. Suwa, J. Nishihiro, Distribution and location characteristics of flood-control reservoir in Japan, Ecol. Civ. Eng., 23(1) (2020) 85-97. (in Japanese)

Future Groundwater Stress in the Yom and Nan River Basins under Climate Change

Chanchai PETPONGPAN[1], ○Chaiwat EKKAWATPANIT[1*], Supattra VISESSRI[2], Srinidhi JHA[3], Lucy BARKER[3] and Jamie HANNAFORD[3]

[1]Department of Civil Engineering, King Mongkut's University of Technology Thonburi, Bangkok 10140, Thailand.
[2]Department of Water Resources Engineering, Chulalongkorn University, Bangkok 10330, Thailand.
[3]UK Centre for Ecology & Hydrology (UKCEH), Wallingford, OX10 8BB, United Kingdom.
[*]E-mail: chaiwat.ekk@kmutt.ac.th

Abstract

Groundwater buffers monsoonal agricultural basins against drought, yet over-abstraction and changing recharge threaten its sustainability. This study projects near-future (2026–2035) groundwater stress in the Yom and Nan River Basins, Northern Thailand, by coupling the fully integrated SWAT-MODFLOW model with the Groundwater Stress Index (GSI). Recharge and ecosystem baseflow were simulated as dynamic surface–subsurface fluxes, and abstraction was derived from 8,024 pumping wells. Three CMIP6 GCMs (MIROC6, MIROC-ES2L and MPI-ESM1-2-LR), selected from 20 models, were downscaled with the change factor method under SSP1-2.6, SSP2-4.5, SSP3-7.0 and SSP5-8.5. All scenarios project warming of up to +0.71 °C, while recharge changes by −6.2% to +25.8%. The basins are already stressed in the reference period (2005–2014; GSI = 1.05–1.42 for two GCMs). Stress increases under most scenarios, and the area with GSI ≥ 1.0 expands by 9–59%, even under SSP1-2.6, with the highest GSI (1.66) under SSP5-8.5. Existing over-abstraction sets the stress baseline, while climate change amplifies its severity and extent, calling for location-specific groundwater management.

Keywords: Groundwater Stress Index; climate change; SWAT-MODFLOW; CMIP6; Thailand

1 Introduction

Groundwater supplies nearly half of global household water demand and sustains river baseflow [1]. In the monsoonal Yom and Nan River Basins of Northern Thailand, growing irrigation abstraction combined with shifting rainfall threatens long-term aquifer storage [2].

The Groundwater Stress Index (GSI), derived from the groundwater footprint concept, compares abstraction with recharge after reserving the groundwater required by ecosystems [3]. Most GSI studies use water-balance methods or global models in which environmental flow is a fixed fraction of recharge and stream–aquifer interaction is ignored [4]. Fully integrated models overcome this by simulating recharge and stream–aquifer exchange as linked physical processes [5]. This study therefore couples SWAT-MODFLOW with the GSI to (1) evaluate CMIP6 GCMs and project near-future climate, (2) quantify changes in recharge and ecosystem baseflow, and (3) identify groundwater stress hotspots under four SSPs.

2 Materials and methods

2.1 Study area and data

The Yom (24,047 km^2) and Nan (34,331 km^2) River Basins are major tributaries of the Chao Phraya River. Annual rainfall is 1,200–1,300 mm, mostly in May–October; land cover is 60% forest and 30% agriculture [2]. Productive unconsolidated aquifers lie along the downstream floodplains, and the Sirikit Dam regulates the Nan River. Inputs comprised a 90-m SRTM DEM, land use and soil maps, daily rainfall from 43 gauges, weather data from 10 stations, daily streamflow from 15 gauges, Sirikit Dam inflow and release records, monthly groundwater levels from 37 wells and hourly pumping rates from 8,024 wells.

2.2 SWAT-MODFLOW model

SWAT-MODFLOW links the semi-distributed SWAT model [6] with the groundwater model MODFLOW [7]. Daily percolation and river stage from SWAT are mapped onto a 900-m MODFLOW grid, and the simulated groundwater–river exchange is returned to SWAT daily [5]. After a three-year warm-up, the model was calibrated for 2007–2014 and validated for 2015–2020. Simulated daily streamflow achieved NSE > 0.70, R^2 > 0.77 and PBIAS within ±18%, and groundwater heads were reproduced with RMSE < 4 m [8].

2.3 Groundwater Stress Index

The GSI was calculated for each grid cell as:

$$GSI = C / (R - E) \quad (1)$$

where C is groundwater abstraction, R is recharge (soil percolation plus riverbed leakage) and E is ecosystem baseflow, i.e. the simulated groundwater discharge to streams [3, 4]. GSI < 0.5, 0.5–1.0 and ≥ 1.0 indicate low, moderate and high stress. Abstraction was held at historical rates to isolate the climate effect.

2.4 Climate projections

Monthly rainfall from 20 CMIP6 GCMs was compared with observations for 1990–2014. MIROC6, MIROC-ES2L and MPI-ESM1-2-LR performed best (NSE = 0.98, 0.87 and 0.83; RMSE = 12.95–35.59 mm) and were selected. Their outputs were downscaled to each station with the change factor method (additive for temperature, multiplicative for rainfall) and used to drive SWAT-MODFLOW for 2026–2035 under SSP1-2.6, SSP2-4.5, SSP3-7.0 and SSP5-8.5. Results were compared with GCM-driven reference runs for 2005–2014.

3 Results and discussion

3.1 Climate and groundwater recharge

All scenarios project warming, reaching +0.71 °C under SSP5-8.5 (MIROC-ES2L), whereas changes in annual rainfall depend on the model, ranging from slight decreases in MIROC-ES2L to +17% in MIROC6 under SSP1-2.6. Reference recharge ranged from 19.13 to 26.80 × 10^6 m^3/day among the GCMs. Future recharge generally increases, by up to +25.8% (MIROC6, SSP1-2.6), but declines in some runs, e.g. −6.2% for MPI-ESM1-2-LR under SSP2-4.5 (Table 1). Higher evapotranspiration under warming can therefore offset rainfall gains.

Table 1 Changes in recharge / area with GSI ≥ 1.0 (%) relative to 2005–2014.

Scenario	MIROC6	MIROC-ES2L	MPI-ESM1-2-LR
Reference R*	22.22	26.80	19.13
SSP1-2.6	+25.8 / +28.8	−1.4 / +59.4	+17.2 / +9.3
SSP2-4.5	+16.6 / +33.4	+2.4 / +50.3	−6.2 / +45.0
SSP3-7.0	+3.9 / +46.8	−1.3 / +55.7	+5.6 / +34.9
SSP5-8.5	+16.4 / +36.2	+7.0 / +46.6	+2.0 / +39.1

*Reference recharge in 10^6 m^3/day.

3.2 Groundwater stress

The basins are already under high stress in the reference period, with mean GSI of 1.05 (MIROC6) and 1.42 (MPI-ESM1-2-LR), while MIROC-ES2L indicates moderate stress (0.56) (Fig. 1). In the near future, GSI rises in most scenarios. Even under SSP1-2.6, MIROC-ES2L shifts from moderate to high stress (GSI = 1.17), and the area with GSI ≥ 1.0 grows in every run, by 9.3–59.4% (Table 1). The highest GSI, 1.66 (+17%), is projected by MPI-ESM1-2-LR under SSP5-8.5, and the high-emission pathways (SSP3-7.0 and SSP5-8.5) increase stress for all three GCMs. Stress hotspots expand mainly across the central and downstream plains, where pumping wells are concentrated.

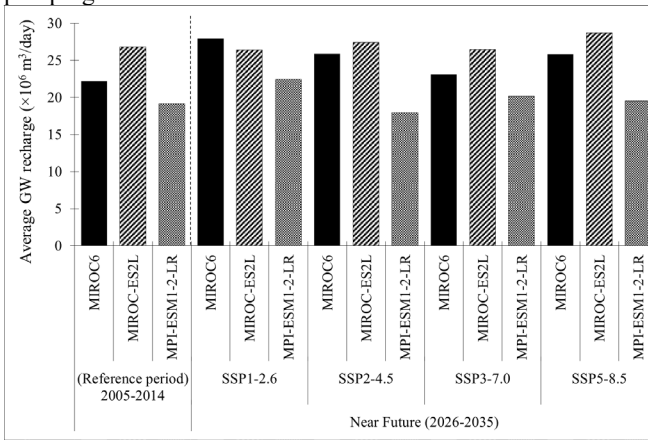


Fig. 1. Average GSI simulated by SWAT-MODFLOW for the reference (2005–2014) and near-future (2026–2035) periods; percentages show change from the reference period.

These results show that historical over-abstraction establishes an unsustainable baseline, consistent with evidence that abstraction is the dominant control on GSI, while climate change acts as a multiplier that increases the severity and extent of stress. Because *E* is simulated as a dynamic stream–aquifer flux rather than a fixed allocation, the framework captures dry-season periods when rivers depend on groundwater. As pumping is likely to rise with warming, the projected GSI values are conservative.

4 Conclusions

Coupling SWAT-MODFLOW with the GSI provided a physically consistent assessment of future groundwater stress in the Yom and Nan River Basins. The basins are already over-stressed, and near-future climate change is projected to increase stress under most scenarios, including the low-emission SSP1-2.6, with the most severe conditions under SSP5-8.5. Controlling abstraction in the identified hotspots, together with measures to enhance recharge, is therefore essential. Future work should incorporate dynamic pumping scenarios and groundwater quality.

Acknowledgments

This study was supported by KMUTT, Thailand Science Research and Innovation (TSRI) and the National Science, Research and Innovation Fund (NSRF) (Grant No. FRB6900121), and by UKCEH's NC International Programme (NE/X006247/1).

References

[1] T. Gleeson, M. Cuthbert, G. Ferguson, D. Perrone, Global groundwater sustainability, resources, and systems in the Anthropocene, Annu. Rev. Earth Planet. Sci. 48 (2020) 431–463.

[2] C. Petpongpan, C. Ekkawatpanit, S.H. Gheewala, S. Visessri, P. Saraphirom, D. Kositgittiwong, S. Kazama, Integrated management of surface water and groundwater for climate change adaptation using hydrological modeling, Environ. Dev. Sustain. 27 (2025) 14321–14341.

[3] T. Gleeson, Y. Wada, M.F.P. Bierkens, L.P.H. van Beek, Water balance of global aquifers revealed by groundwater footprint, Nature 488 (2012) 197–200.

[4] T. Mahdavi, Evaluation of quantitative and qualitative sustainability of aquifers by groundwater footprint methodology, Environ. Monit. Assess. 193 (2021) 368.

[5] R.T. Bailey, T.C. Wible, M. Arabi, R.M. Records, J. Ditty, Assessing regional-scale spatio-temporal patterns of groundwater–surface water interactions using a coupled SWAT-MODFLOW model, Hydrol. Process. 30 (2016) 4420–4433.

[6] J.G. Arnold, R. Srinivasan, R.S. Muttiah, J.R. Williams, Large area hydrologic modeling and assessment part I: Model development, J. Am. Water Resour. Assoc. 34 (1998) 73–89.

[7] A.W. Harbaugh, MODFLOW-2005, the U.S. Geological Survey modular ground-water model—the ground-water flow process, USGS Techniques and Methods 6-A16 (2005).

[8] C. Petpongpan, C. Ekkawatpanit, D. Kositgittiwong, Groundwater vulnerability assessment using modified DRASTIC method with integrated hydrological model, Groundw. Sustain. Dev. 29 (2025) 101416.

[9] Z. Zahmatkesh, M. Karamouz, E. Goharian, S.J. Burian, Analysis of the effects of climate change on urban storm water runoff using statistically downscaled precipitation data and a change factor approach, J. Hydrol. Eng. 20 (2015) 05014022.

Modernizing Flood Hazard and Risk Assessment using Gridded Rainfall Data, Stochastic Methods, and Physics-based Modeling

○ Daniel Wright[1*], Lei Yan[1], Benjamin FitzGerald[1], Antonia Sebastian[2], Marissa Weber[2], David Rosa[3], Keil Neff[4] & Haden Smith[4]

[1]Department of Civil and Environmental Engineering, University of Wisconsin-Madison, Madison, Wisconsin, United States of America.
[2]Department of Earth, Marine and Environmental Sciences, University of North Carolina, Chapel Hill, North Carolina, United States of America.
[3]Risk Management Directorate, Federal Emergency Management Agency, Washington DC, United States of America.
[4]Risk Management Center, US Army Corps of Engineers, Denver, Colorado, United States of America.

[*]E-mail: danielb.wright@wisc.edu

Abstract

Conventional flood hazard and risk assessment methods—including statistical flood frequency analysis (FFA) and design storm methods—rely on inadequate data sources and oversimplified assumptions and cannot easily incorporate modern advances in observations, modeling, and computing power. This presentation synthesizes more than a decade of recent research combining three complementary advances to modernize flood hazard and risk assessment: 1) high-resolution gridded rainfall data including from weather radar, satellites, and convection-permitting regional climate models; 2) stochastic storm transposition (SST), which resamples and randomly relocates observed extreme storms to generate large ensembles of realistic rainfall scenarios; and 3) physics-based, distributed hydrologic and hydraulic modeling that translates these scenarios into flood estimates throughout a river network. Case studies from distinct watersheds in the United States show how this framework can overcome key limitations of conventional methods and supports modern real-world flood risk assessment applications.

Keywords: Extreme rainfall; flooding; risk assessment; stochastic methods; physics-based modeling.

1 Introduction

Flood frequency analysis (FFA)—the science and art of estimating the probability distribution of floods, including key quantiles such as the 100-year flood—is a longstanding challenge with important real-world impacts. FFA results underpin the design of dams, levees, and stormwater infrastructure, floodplain mapping, and flood insurance. The approaches used in practice today, including station-based statistical flood frequency analysis (FFA) and design-storm methods, were formulated decades ago around existing rain gage and stream gage records [1]. These approaches face serious limitations: gage records are often too short to characterize rare extremes and are difficult to justify in nonstationary climatic and land use conditions; station-based methods give limited insight into the spatiotemporal processes that produce floods; and the approaches are not easily reconciled with modern precipitation remote sensing, atmospheric modeling, and distributed physics-based hydrologic modeling—thus leaving those scientific and technological advances underused in FFA practice.

In this presentation, an alternative approach to FFA is presented that overcomes many of the limitations of conventional methods. Specifically, stochastic storm transposition (SST) addresses these limitations by resampling and randomly relocating observed extreme storms within a homogeneous region to generate large numbers of realistic rainstorms over a watershed [1]. Because SST preserves observed rainfall space-time structure, it pairs naturally with gridded precipitation data (including from weather radar and high-resolution convection-permitting regional climate models) and physics-based hydrologic models. This presentation reviews more than a decade of recent SST research, including application to real-world flood risk assessment.

2 Materials and methods

The SST approach presented here requires several things: 1) a geographic transposition domain over which extreme rainfall properties are roughly homogeneous, such that a storm that occurred within the domain could have occurred with equal or similar probability and properties elsewhere in the domain; 2) a catalog of observed or dynamically-simulated extreme storms over that domain built from gridded rainfall, and 3) a resampling scheme. A random number of storms is drawn using a stochastic (typically Poisson-distributed) arrival process, and each storm's rainfall field is randomly shifted geographically, generating a synthetic year of rainstorms [2,3]. Repeating this procedure thousands of times yields a long synthetic record from which extreme precipitation annual exceedance probabilities (AEPs) can be estimated directly, without fitting a parametric distribution. More importantly, these transposed rainstorms can be used as inputs to a hydrologic model to estimate flood frequency. When used with distributed physics-based models specifically, SST unlocks important features including explicit modeling of the spatiotemporal interactions of precipitation structure and variability with landscape features and the ability to model flood frequency across a continuum of spatial scales.

We illustrate this framework using RainyDay, an open-source SST tool [4], coupled with distributed hydrologic

models that route each rainfall field through the watershed's channel network, accounting for antecedent soil moisture and snowpack [5,6,7,8]. This produces flood peaks at every network location rather than a single outlet. We will illustrate the approach for several watersheds around the United States that represent a wide diversity of hydroclimatic processes.

3 Results and discussion

In the Turkey River watershed in the state of Iowa, coupling SST with a distributed model produced flood estimates that are more consistent with observed peaks than statistical FFA and revealed that flood seasonality is changing—spring floods driven by snowmelt and rain-on-snow are becoming less frequent while summer floods by intense short storms are becoming more common—an important set of complex nonstationary hydrologic processes that FFA cannot resolve [3,6,7]. In addition, we use Turkey River to illustrate the potential for high-resolution convection-permitting regional climate model simulations to drive SST-based flood frequency estimates to better understand possible future flood outcomes [8].

In the mountainous Big Thompson basin in the state of Colorado, SST-based flood estimates were broadly consistent with both observational evidence and paleoflood information, and were very different from the results of traditional statistical FFA methods. This illustrates the fundamental centrality of flood physics in shaping flood frequency, while also illustrating that SST-based methods can extend to very rare AEPs (10^{-4} in this example) [7].

In the coastal Neuse watershed in North Carolina, SST-based flood damage assessments were compared against those based on traditional design storm methods [9]. Average annual losses based on SST methods were almost twice as large as those from design storm methods, highlighting the key roles of rainfall spatiotemporal variability in driving the probability distributions of flood damage.

4 Conclusions

Combining gridded rainfall data, stochastic storm transposition, and physics-based distributed hydrologic modeling offers a practical, increasingly mature framework for modernizing flood hazard and risk assessment—better representing rainfall space-time structure, enabling multiscale flood analysis in a single set of simulations, and supporting nonstationary climate and land-use conditions. Continued progress requires extending the approach to data-sparse regions with satellite remote sensing and numerical weather prediction, improving uncertainty quantification, and translating these research demonstrations into standard practice for floodplain mapping and infrastructure risk decisions.

We close by highlighting an ongoing major real-world application of SST: the Future of Flood Risk Data (FFRD) initiative, led by the Federal Emergency Management Agency and the US Army Corps of Engineers. FFRD aims to provide probabilistic flood hazard and risk assessment nationwide. Within FFRD, inland flooding across the entire United States will use SST and distributed models, posing major challenges in terms of scaling up of these methods to large numbers of large river basins across a huge diversity of physiographic and hydroclimatic regions. At the same time, FFRD is rapidly generating knowledge and tools for SST-based flood frequency analysis which will be useful in a very wide range of applications.

References

[1] Wright, D.B., Yu, G., England, John F., 2020. Six Decades of Rainfall and Flood Frequency Analysis Using Stochastic Storm Transposition: Review, Progress, and Prospects. Journal of Hydrology 585:124816.

[2] Wright, D.B., Smith, J.A., Baeck, M.L., Villarini, G., 2013. Estimating the frequency of extreme rainfall using weather radar and stochastic storm transposition. J. Hydrol. 488, 150–165.

[3] Wright, D.B., Smith, J.A., Baeck, M.L., 2014. Flood frequency analysis using radar rainfall fields and stochastic storm transposition. Water Resour. Res. 50, 1592–1615.

[4] Wright, D.B., Mantilla, R., Peters-Lidard, C.D., 2017. A remote sensing-based tool for assessing rainfall-driven hazards. Environ. Model. Softw. 90, 34–54.

[5] Zhu, Z., Wright, D.B., Yu, G., 2018. The impact of rainfall space-time structure in flood frequency analysis. Water Resour. Res. 54, 8983–8998.

[6] Yu, G., Wright, D.B., Zhu, Z., Smith, C., Holman, K.D., 2019. Process-based flood frequency analysis in an agricultural watershed exhibiting nonstationary flood seasonality. Hydrol. Earth Syst. Sci. 23, 2225–2243.

[7] Yu, G., Wright, D.B., Holman, K.D., 2021. Connecting Hydrometeorological Processes to Low-Probability Floods in the Mountainous Colorado Front Range. Water Resources Research 57(4).

[8] Yu, G., Wright, D.B., Li, Z., 2020. The Upper Tail of Precipitation in Convection-Permitting Regional Climate Models and Their Utility in Nonstationary Rainfall and Flood Frequency Analysis. Earth's Future e2020EF001613.

[9] Baer, J.A., Sebastian, A., Grimley, L.E., et al., 2026. Neglecting Spatiotemporal Rainfall Variability Misrepresents Flood Hazard and Risk." NPJ Natural Hazards.

Green Infrastructure and Urban Resilience: Effects on Seasonal Hydrology and Extreme Heat in Milwaukee, Wisconsin, USA

○ G. Aaron Alexander[1*], Daniel B. Wright[1] , Carolyn B. Voter[1], & Steven P. Loheide II[1]
[1]Department of Civil and Environmental Engineering, University of Wisconsin-Madison, Madison, Wisconsin, United states of America.
[*]E-mail: gaalexander3@wisc.edu

Abstract

As cities continue to expand and the climate continues to warm, urban resilience plans featuring Green Infrastructure (GI) are becoming more common. Traditionally, GI is implemented to reduce runoff, which in turn reduces flood impacts, while simultaneously helping cool cities. Despite GI's importance for resilience, the city-scale changes of heat and hydrology remain hard to quantify due to the small-scale nature of GI. Earth system models, which can simulate hydrology and heat simultaneously, are a clear tool for understanding the impacts of GI implementation, but they represent urban areas poorly and almost universally omit small-scale features like GI. This is particularly important for understanding changes in phenomena like urban heat islands (UHIs) and urban rainfall modification (URM), which GI could help abate. In this presentation, we utilize Noah-MP for Heterogenous Urban Environments (HUE), a new land-surface model capable of explicitly representing GI within a city, to simulate the effects of a city-scale urban resilience plan in Milwaukee, Wisconsin, USA. We develop four different potential GI scenarios to showcase how urban resilience effects seasonal hydrology, rainfall, and extreme heat at different scales. Our results indicate that widespread implementation of GI reduces runoff while increasing evapotranspiration and potential groundwater recharge in a dose-dependent manner. We also find that rainfall totals are slightly increased. Further, we find that extreme heat is reduced in our study region, but there are smaller reductions in extreme heat when accounting for heat stress (i.e. the Universal Thermal Comfort Index). Future work includes the need to develop datasets to use Noah-MP HUE in other regions, and an examination of other cities to support current urban resilience programs world-wide.

Keywords: green infrastructure; urban resilience; flooding; extreme heat; urban rainfall modification.

1 Introduction

Cities house most of the human population and are projected to expand throughout the next century. This expansion, characterized by impervious surfaces like buildings, roadways, and sidewalks, increases the amount of runoff that is generated within a city. Simultaneously, adding more impervious surfaces while replacing natural vegetation causes cities to form urban heat islands (UHIs), where heat is generally more extreme than surrounding natural ecosystems. There is also emerging evidence that cities around the globe are modifying rainfall, termed urban rainfall modification (URM), due to complex interactions between UHIs, enhanced convergence, and aerosols. This is especially important for coastal communities, as their proximity to large water bodies provide sources of moisture that can make convective rainfall more intense.

In response, cities globally are planning and building green infrastructure (GI). GI includes expanding tree canopy, installing bioswales, depaving, adding green roofs, changing roadways to permeable pavements, and transferring runoff to vegetated surfaces. While these practices are generally targeted at reducing runoff, and therefore reducing flooding and water quality impacts, the re-introduction of vegetation into urban spaces has important impacts on UHIs and changes rainfall (URM) that are critical for planning and adaptation purposes.

In this presentation, we use a regional earth systems model to explore the impacts that a real-world urban GI plan in the United States, Milwaukee, Wisconsin, has on seasonal hydrology, extreme heat, and rainfall over multiple years. This study utilizes a new land-surface model, Noah-MP for Heterogenous Urban Environments (HUE) [1], in which all GI within Milwaukee's greening plan are explicitly represented. Noah-MP HUE improves simulations of heat within cities [2] and better represents extreme rainfall mechanisms that drive flooding in the Milwaukee area [3], and therefore represents a critical step forward for the next generation of urban climate modeling.

2 Materials and methods

This study requires three distinct steps. The first involves classification of landcovers within the Milwaukee region to leverage HUE. We utilize datasets from local LiDAR studies, satellite remote sensing sources, and national imagery campaigns to generate 1 m^2 landcover maps. These landcover maps explicitly contain important features, such as tree that covers pavement and commercial buildings that are eligible for green roof installation, that allow for the generation of different scenarios used in this study.

The second step involved creating multiple, plausible scenarios of GI based on current policy within the Milwaukee area. To do this, we partnered with the Milwaukee Metropolitan Sewerage District (MMSD) to develop scenarios based on what current management targets. This leveraged a prioritization metric to help inform 'how much' of different GI should be included in what places. We developed four separate scenarios to test the effects that widespread adoption of GI could produce. These are 1) Baseline, a scenario with no GI that is representative of Milwaukee in 2018, 2) Half Policy, a scenario where half of MMSD targets are reached, 3) Full Policy, a scenario where

all of the MMSD targets are reached, and 4) Extra Policy, a scenario where ~150% of MMSD targets are reached.

The final step involved using these scenarios to run multiple years of simulations using a regional earth systems model, the Weather Research and Forecasting (WRF) model v4.7.1. For each year, we simulate the warm season in Milwaukee, 1 June – 1 Nov. We then perform analysis on changes in water budgets, including changes to runoff, evapotranspiration, and potential groundwater recharge. We further use storm tracking to analyze average changes to rainfall totals and rain rates in different areas of Milwaukee. Finally, we analyze both the number of extreme heat days and the diurnal evolution of surface conditions during these extreme heat days for both dry bulb temperatures and heat stress (i.e. the Universal Thermal Comfort Index).

3 Results and discussion

We find that GI reliably and, in a dose-dependent manner, decreases runoff and simultaneously increases evapotranspiration and potential groundwater recharge regardless of seasonal weather conditions. This occurs regardless of seasonal conditions (i.e. wet years vs. climactically normal years vs. dry years). We also find that GI often leads to a slight increase in rainfall, but this signal is inconsistent; there is no coherent spatial pattern in increases (across individual years or over multi-year average), and no coherent pattern of increase in rainstorm depth for "large" storms (i.e., storms with > 1" total rainfall [25.4 mm]). However, it is important to note that any seasonal increases in rainfall are always much smaller than the changes in evapotranspiration and deep drainage, thus runoff is reliably decreased and changed into other components of the hydrologic cycle due to GI even if rainfall increases.

We also find that GI are a powerful tool to reduce the number of extreme heat days, defined to be days where the max air temperatures in the downtown region of Milwaukee exceeds 90° F (32.2° C). The number of these extreme heat days decreases in a dose-dependent manner, with greater reductions occurring as the amount of GI increases. We also find that the changes in air temperatures on these hot days are widespread and "build" until the end of the day. Meanwhile, due to increased humidity due to GI, resulting heat index changes of smaller magnitude and are localized to only the hottest part of the day.

4 Conclusions

GI is increasingly being implemented in cities across the world. Understanding what changes in the regional climate these adaptation measures will create is critical for large-scale investment and future projects. Our results suggest that runoff is reduced due to either increased evapotranspiration or groundwater recharge. We also find that widespread GI implementation could reduce extreme temperatures.

We also find that rainfall slightly increases. This could point to an unexpected consequence of current urban climate adaptation measures. Understanding to what extent this rainfall increase occurs requires more years of simulations and more cities to be examined worldwide. Further work is also needed to interpret and downscale these results to more actionable scales. We close by highlighting ongoing work wherein we are generating similar landcover maps and prioritization metrics in other cities in the United States, discuss what data is needed for this model to be used in cities around the world, and discuss opportunities for hyper-local scale emulators to help generate neighborhood scale impacts.

References

[1] Alexander, G.A., Voter C.B., Wright D.B., Loheide II, S.P., 2024. Urban ecohydrology: Accounting for sub-grid lateral water and energy transfers in a land surface model. *Water Resources Research,* 60, e2023WR035511.

[2] Alexander, G.A., Wright D.B., Voter C.B., Loheide II, S.P., 2025. City-scale evaluation of urban ecohydrologic processes on surface energy balances, heat, and humidity. *Urban Climate,* 63, 102596.

[3] Alexander, G.A., Wright D.B., Voter C.B., Loheide II, S.P., 2026. Ecohydrologic Processes Modify Urban Rainfall Intensification in Land-Atmosphere Simulations. *Geophysical Research Letters,* 53, e2026GL121642.

Risk-Based Selection of Water Quality Monitoring Stations for Early Warning at the Ambatale Water Supply Scheme in Sri Lanka

○ Lalith RAJAPAKSE[1,2]*, Nalintha WIJAYAWEERA[1,2] & Suraj THARUKA[1,2]

[1]Department of Civil Engineering, University of Moratuwa, Moratuwa 10400, Sri Lanka.

[2]UNESCO-Madanjeet Singh Centre for South Asia Water Management (UMCSAWM), University of Moratuwa, Moratuwa 10400, Sri Lanka.

*E-mail: lalith@uom.lk.

Abstract

Effective protection of river-fed water supplies requires monitoring networks that reconcile early detection with reliable confirmation of water-quality deterioration at abstraction points. This study establishes a technical framework for designing an optimal real-time water quality monitoring network to protect the Ambatale Water Supply Scheme (AWSS) along the Kelani River, Sri Lanka. Facing increasing risks from rapid urbanization, dense industrialization, and climate-induced threats such as salinity intrusion, five spatial sensor combinations were evaluated using hydraulic travel times, historical water quality indices, and a multi-criteria decision analysis (MCA). Results identify Combination 03 (Pugoda, Nawagamuwa, Biyagama, and Ambatale Intake) as the optimal core network (weighted score of 4.65/5.00). This configuration establishes a three-layer upstream defense that maximizes early warning response time, isolates industrial risk corridors, and provides direct intake surveillance against saline front movements.

Keywords: Early warning; Kelani River; Multi-criteria assessment; Sensor placement; Water safety planning.

1 Introduction

The Ambatale Water Supply Scheme (AWSS) serves as the primary municipal drinking water source for the Greater Colombo region in Western Sri Lanka, producing over 500,000 m^3/day. Water-quality deterioration threatens river-water abstraction through industrial discharges, urban wastewater, and saline intrusion. At Ambatale, an intake-only sensor can confirm deterioration but cannot provide advance warning of a downstream-moving pollution plume. Conversely, distant sensors provide longer warnings but weaker certainty about the eventual intake concentration because of mixing, dilution and intervening discharges.

River monitoring design can jointly minimise contaminant detection time and maximise monitoring reliability [1]. Observability-based placement further supports contaminant source reconstruction, showing why source attribution requires explicit design consideration [2]. Accordingly, this study integrates historical water-quality evidence, preliminary transport-time estimates and operational constraints to identify a preferred monitoring configuration for the Ambatale intake in the Kelani River Basin.

2 Materials and methods

Candidate monitoring sites were evaluated based on their contributing river reaches, the spatial distribution of industrial pollution risks, and monthly water-quality indices from 20 stations during 2016–2024, with varying record lengths. Direct historical records were available for Ambatale and Pugoda, while Welivita and Kaduwela served as spatial proxies for Biyagama and Nawagamuwa, respectively. Site suitability was assessed using the Drinking Water Treatability Index (*DWTI*) and its component indices: the Sediment and Physical Quality Index (*SPQI*), Salinity Intrusion Index (*SII*), Nutrient Quality Index (*NQI*), Toxic Contaminant Index (*TCI*), and Microbial Risk Index (*MRI*). Higher index values indicate more favourable water-quality conditions. These indices were used to compare historical conditions and inform site selection, rather than to define operational alarm thresholds. Following *Eq.1* shows how *DWTI* is calculated by using component indices.

$$\mathrm{DWTI} = w_1\mathrm{SPQI} + w_2\mathrm{SII} + w_3\mathrm{NQI} + w_4\mathrm{TCI} + w_5\mathrm{MRI} \quad \text{Eq. 01}$$

where w_1 to w_6 represent the fixed weights assigned to the respective pollutant categories. The component weights were normalized so that the sum of all component weights equals 1.0, while the sub-weights were distributed equally among the parameters belonging to each component. The resulting weighting scheme is presented in ***Table 1*** below.

Table 1: Weights and parameters used for each component indices

Sub-index	Parameter	Exceedance (%)	Sub-weight	Weight
SPQI	Turbidity	80.2	0.060	0.06
SII	EC	6.6	0.085	0.17
	Chloride	6.8	0.085	
NQI	Nitrate	1.2	0.060	0.12
	Phosphate	1.9	0.060	
TCI	Cr	13.7	0.200	0.40
	Pb	7.4	0.200	
MRI	T. Coli	45.0	0.125	0.25
	E. Coli	89.5	0.125	

Travel time was estimated as $t = L/v$ using approximate channel distance L and assumed mean velocity v. The adopted velocity ranges were 0.6–1.0, 1.0–1.5 and 1.5–4.2 m/s for low, typical and high flow, respectively. These screening assumptions exclude spatially variable hydraulics, dispersion and pollutant transformation and therefore do not represent calibrated plume-arrival predictions.

Five configurations were compared, each retaining Biyagama and Ambatale as mandatory stations. Additional sites were Nawagamuwa (C1), Pugoda (C2), Nawagamuwa and Pugoda (C3), Nawagamuwa, Ruwanwella and

Haltotawatta (C4), or Raggahawatta tributary (C5). Ratings of 1–5 were assigned to warning time (20%), industrial and urban risk coverage (20%), spatial coverage (15%), source attribution (15%), redundancy (10%), water-quality evidence (10%), and cost/operational feasibility (10%). Weighted sums ranked the alternatives.

3 Results and discussion

Industrial activity was concentrated in the lower basin, supporting monitoring within the urban and industrial corridor. Historical mean DWTI values at Welivita (64.26) and Kaduwela (63.95) were close to Ambatale (64.09), supporting their use as lower-reach reference stations (***Fig. 1***). Victoria Bridge (54.80) and Raggahawatta Ela (54.66) had poorer overall conditions. Victoria Bridge had particularly low salinity and microbial indices, while Raggahawatta supported targeted tributary surveillance. Victoria Bridge is a historical reference, not a proposed sensor site; its salinity-monitoring function is assigned to Ambatale intake. These observations support combined upstream pollution surveillance and intake-level salinity monitoring, but monthly records cannot demonstrate detection of short-lived incidents.

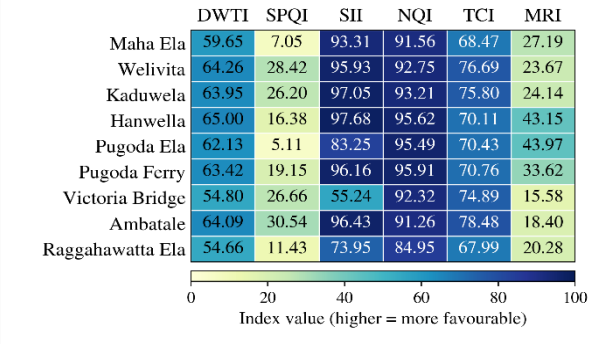


Fig. 1: Historical mean water-quality indices variation across the basin-wide stations

Among the combinations, C3 ranked first (4.65), followed by C4 (4.20), C2 (3.40), C1 (3.35) and C5 (2.90) (***Fig. 2***). Pugoda provides early main-stem warning, Nawagamuwa monitors the lower industrial corridor, and Biyagama provides final upstream confirmation. Ambatale directly monitors intake conditions. C4 offers stronger tributary attribution but requires five stations and omits Pugoda. C5's lower network-level score does not negate Raggahawatta's local pollution risk. The ranking is conditional on the adopted weights and judgement-based ratings.

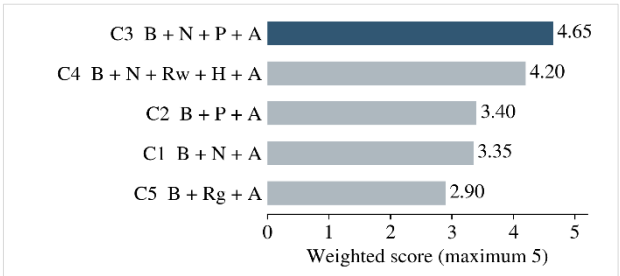


Fig. 2: Configuration ranking; A: Ambatale; B: Biyagama; N: Nawagamuwa; P: Pugoda; Rw: Ruwanwella; H: Haltotawatta; Rg: Raggahawatta

Under the assumed high-flow range, transport times shorten to 2.04–5.72 hr from Pugoda, 0.73–2.04 hr from Nawagamuwa and approximately 6–18 min from Biyagama. The operational response window would be further reduced by detection, verification and communication delays. Sequential alarms could help identify the affected reach, although missed detections, sensor faults and pollutant transformation would complicate source attribution.

Continuous pH, turbidity, electrical conductivity and dissolved oxygen should be complemented by organic, nutrient, metal and microbial measurements. Priority additions include TDS/salinity, ammonia/ammonium, iron and cadmium; arsenic and mercury are precautionary indicators, not evidence of established contamination. Ambatale requires particular attention to conductivity, salinity and chloride. Measurement frequency and methods must match sensor and laboratory capabilities; five-day Biochemical Oxygen Demand (BOD) cannot provide immediate warning. Operational use requires calibrated baselines, telemetry checks and predefined responses [3]. For Ambatale, site-specific baselines, telemetry checks and predefined intake-response procedures are therefore essential. The assessment remains limited by spatial proxies, monthly sampling, assumed velocities and judgement-based ratings.

4 Conclusions

A four-station core network at Pugoda, Nawagamuwa, Biyagama and Ambatale provides the strongest assessed balance between warning time, lower-basin risk coverage and operational feasibility. The configuration integrates successive upstream detection with direct intake surveillance. A phased implementation strategy is recommended, with subsequent tributary monitoring guided by observed pollution recurrence and source-attribution requirements. Hydraulic validation and sensitivity analysis are required before using the results in operational warning protocols.

Acknowledgements

This work draws on the UN-Habitat project on Safe and Resilient Water Supply for Western Cities – Integrating Climate Resilience into Water Safety Plans (WSPs) of the Ambatale Water Supply Scheme (AWSS), involving Uni-Consultancy Services of University of Moratuwa and the National Water Supply and Drainage Board, Sri Lanka.

References

[1] I. T. Telci, K. Nam, J. Guan, and M. M. Aral, "Optimal water quality monitoring network design for river systems," *J. Environ. Manage.*, vol. 90, no. 10, pp. 2987–2998, Jul. 2009, doi: 10.1016/J.JENVMAN.2009.04.011.

[2] M. Bartos and B. Kerkez, "Observability-Based Sensor Placement Improves Contaminant Tracing in River Networks," *Water Resour. Res.*, vol. 57, no. 7, p. e2020WR029551, Jul. 2021, doi: 10.1029/2020WR029551.

[3] R. Murray, R. Janke, W. E. Hart, J. W. Berry, T. Taxon, and J. Uber, "Sensor network design of contamination warning systems: A decision framework," *J. Am. Water Works Assoc.*, vol. 100, no. 11, pp. 97–109, Nov. 2008, doi: 10.1002/J.1551-8833.2008.

Enhancing Health Security through Strengthened Legal Governance, Institutional Integration, and Technological Advancement for Sustainable Water Management in the Kelani River Basin, Sri Lanka

o H.L. Kamal PRIYANTHA [1*], H.M.H. Karunaweera MAKUMBURA [1] & W.A.T.D. WANNIARACHCHI[1]

[1]Central Environmental Authority, Baththaramulla, Sri Lanka.
[*]E-mail: kamal@cea,lk

Abstract

The Kelani River is a vital source of drinking water for the Colombo metropolitan region and supports industrial, agricultural and ecological activities. Protecting its water quality is essential for public health and sustainable development. This study evaluates the role of the Central Environmental Authority's (CEA) committee on siting of High and Medium Polluting Industries (H&M committee) in preventing industrial pollution through regulatory governance, inter-agency coordination and improved wastewater-management practices, under the Cabinet Memorandum framework establish to protect Kelani river water quality.

The study reviews 25 proposal records covering 2018–2026 across 106 most-sensitive and 91 sensitive Grama Niladhari divisions. The assessment considers high and medium industrial categories such as textile, food and beverage, vehicle service, gas and oil storages, and criteria are wastewater quantity,treatment technologies, discharge destinations and committee decisions, with particular emphasis on protecting the Ambatale, Biyagama & Nawagamuwa drinking-water intakes.Preliminary findings indicate that 16 proposal entries were approved, including two conditional approvals, while 05 proposals were rejected and the remaining proposals require resubmission after improvements to the treatment systems. The data describe wastewater generation, pollution levels and reduced pollution loads in to the river after rejecting the siting of textile processing industries. Out of 07 textile industries producing a total wastewater quantity of 9,336 m3/day, accounted COD load of 23,340x10^3kg/day and a BOD load of 8,402.4 x10^3kg/day. By rejecting 02 industries, with a wastewater quantity of 8901 m3/day, and followed by treatment the reduced COD and BOD loads to the river system was 2,227.75 x10^3kg/day and 267.25 x10^3kg/day respectively.Five food and beverage industries discharging 3,070 m3/day of wastewater was evaluated for their treatment methods, discharge points and reuse technologies, and approved subject to conditions for strict compliance and monitoring by reducing the raw wastewater COD load of 15,350 x10^3kg/day in to 757.5 x10^3kg/day and the BOD load of 9,210 m3/day in to 92.1 x10^3kg/day respectively.Seven vehicle service, gas and oil storage facilities were evaluated which discharge 88 m3/day. The COD of untreated wastewater was 264 x10^3kg/day and the BOD load was 70.4 x10^3kg/day. After treatment, the COD and BOD loads were 22 x10^3kg/day, and 2.64 x10^3kg/day by reducing the pollution load discharge in to the river.The records identify preventive measures including wastewater recycling, biological and chemical treatment, reverse osmosis, zero-liquid-discharge systems, controlled reuse and oil separation. The study concludes that the H&M Committee provides an important mechanism for reducing potential industrial threats to drinking-water sources by institutional coordination, regulatory enforcement and operational monitoring which further enhance source-water protection. To quantify the committee's environmental effectiveness requires verified wastewater flows, pollutant concentrations, treatment performance and compliance data. These improvements are essential to strengthen the drinking-water safety, public-health security and sustainable management of the Kelani River Basin.

Keywords: Kelani River Basin 1; drinking-water safety 2; health security 3; CEA 4; H&M Committee 5.

1.0 Introduction

The Kelani River Basin (KRB), is located in the western region of Sri Lanka which drains fresh water to the Kelani River through its tributaries. Recharges from surface and ground water regimes of the basin, the Kelani River is the 4th longest river (145 km) among 103 major rivers in Sri Lanka.The river supplies 80% of drinking water for Colombo region [1] by main Kelani river intake points at Ambatale, Biyagama & Nawagamuwa which account 728,364 m3/day . According to CEA data base 2026 June about 5515 industries are distributed in the KRB which contribute to the pollution loading of the river. As depicted in its regulations and standards published under the National Environmental Act No 47 of 1980, the CEA is entrusted with issuing Environmental Protection Licenses, Environmental Recommendation for siting of industries and approving of projects.[2],[3],[4] for protection of the environment

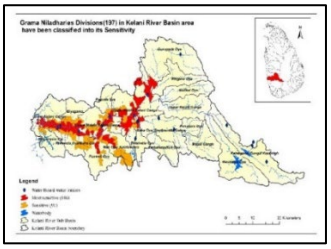
Table 1 Industry distribution in Kelani river basin.

District	A	B	C	Total
Colombo	166	2179	870	3215
Gampaha	126	1020	456	1602
Kalutara	05	19	07	31
Kandy	0	02	03	05
Kegalle	46	225	260	531
N-eliya	01	40	63	104
Rathnapura	0	15	12	27
Total	**344**	**3500**	**1671**	**5515**

including water resources. Despite the existing legal procedures, the CEA is empowered with the task of implementing the Cabinet Memorandum No 93/340/166and 93/340/166/1 and consider the guidelines set out for siting of industries in the vicinity of Kelani river. [5]The Cabinet decision also specifically entrusted the CEA with monitoring establishment of industries along the Kelani River, reporting violations/non-adherence to the relevant Project Approving Agencies.

2.0 Materials & Methods

The study reviews administrative sensitivity classifications, industrial categories based on pollution potential on 25 industrial proposals received during the period of 2018–2026. The sensitivity framework identifies 106 most-sensitive and 91 sensitive GN divisions across Colombo, Gampaha, Kegalle and Ratnapura districts as shown in figure 01.



Each proposal was considered in terms of industrial category, wastewater type and quantity, treatment technology, intended discharge or reuse destination, and recorded committee outcome.

Fig 1. Sensitive & most sensitive GN

The assessment also considered potential pathways for organic pollution, oils, hazardous chemicals, heavy metals and persistent contaminants to reach the Kelani River or connected waterways.

3.0 Results & Discussion

Out of the 25 proposals 16 were recorded as approved, including two conditional approvals. Remaining proposals require resubmission while 05 proposals were rejected. The industry types ranged from textile processing, Food, Distilleries, rubber based industries, oil / petroleum related activities, service station and waste management.

These preliminary results show that the H&M Committee process accommodates both approval and intervention where further technical scrutiny, redesign or relocation is considered necessary. The data [6] describe wastewater generation, pollution levels and reduced pollution loads in to the river after rejecting the siting of Textile processing industries during the evaluation, which out of 07 textile industries producing a total wastewater quantity of 9,336 m3/day, accounted COD load of 23,340x10^3kg/day and a BOD load of 8,402.4 x10^3kg/day. By rejecting 02 industries, with a wastewater quantity of 8901 m3/day, and followed by treatment the reduced COD load to the river system was 2,227.75 x10^3kg/day and the reduced BOD load was 267.25 x10^3kg/day.Five food and beverage industries discharging 3,070 m^3/day of wastewater was evaluated for their treatment methods, discharge points and reuse technologies, and approved subject to conditions for strict compliance and monitoring by reducing the raw wastewater COD load of 15,350 x10^3kg/day in to 757.5 x10^3kg/day and the BOD load of 9,210 m^3/day in to 92.1 x10^3kg/day respectively. Seven vehicle service industries involving motors, gas and oil storage industries were evaluated which produced 88 m3/day. As the untreated wastewater COD load was 264 x103kg/day and the BOD load was 70.4 x103kg/day. After treatment, the COD load decreases to 22 x103kg/day, and the BOD load decreases to 2.64 x103kg/day reducing the pollution load discharge in to the river.Their systematic implementation, supported by effective regulatory oversight and inter-agency coordination, can contribute significantly to sustainable industrial development, improved raw-water quality and long-term public-health protection.The GN-based sensitivity framework provides a valuable administrative foundation for screening industrial proposals. Its effectiveness can be further enhanced by integrating GIS-based analysis, updated land-use and flood-hazard data, river networks, and assessments of contaminant travel time and downstream intake vulnerability.Industrial risk assessments should consider hazardous materials, wastewater generation, treatment performance, residual-waste management, and potential accidental releases. Strong coordination among the CEA, NWSDB, Industrial Technology Institute, Board of Investment, Ministry of Industry, and planning authorities would promote consistent decision-making, effective monitoring, and timely enforcement.

4.0 Conclusions and Recommendations

The CEA's H&M Committee plays a vital preventive role in reducing potential industrial wastewater loads entering the Kelani River Basin through regulatory review, pollution-control requirements and the promotion of appropriate wastewater-management practices. By evaluating industrial proposals against applicable environmental protection standards, discharge limits and wastewater-treatment requirements, the Committee helps minimize pollutant releases at their source and safeguard river-connected water resources. The review of industrial proposals provides a practical basis for strengthening pollution prevention before contaminants reach rivers and drinking-water intakes. Vulnerability can further improve the prioritization of inspections and monitoring.Overall, strengthening the H&M Committee's regulatory oversight, wastewater-management requirements and inter-agency coordination can contribute to cleaner rivers, improved raw-water protection and greater drinking-water security in the Kelani River Basin. Quantifying this contribution through verified proposal records, wastewater volumes, compliance rates and pollutant-load measurements will provide a robust evidence base for demonstrating progress towards sustainable industrial development and long-term.

5.0References

[1] Abeysinge, N. D. A., Samarakoon, M., Analysis of variation of waterquality in Kelani River, Sri Lanka. Int. J. Environ. Agric. Biotechnol.2017,2,23895

[2]CEA Industries/activities listed under part "A", "B", "C", and "D" in the Gazette Notification No.2264/18 dated 27.01.2022.

[3]CEA(Protection and Quality) Regulation Gazette Notification No. 1534/18 dated 01.02.2008.and its amendment No.2264/17 dated 27.01.2022.

[4]CEA Guideline for issuance of Environmental Recommendations and Environmental Protection Licenses 2024.

[5] Cabinet paper No.93/340/166 and 93/140/166/1 dated 15·09·1993.

[6] CEA H&M File data 2018 -2026.

Correlation-Based Assessment of Water Quality Parameters in the Kelani River Basin, Sri Lanka

Jagath MANATUNGE[1*] & Nalintha WIJAYAWEERA[1]
[1]Department of Civil Engineering, University of Moratuwa, Colombo, 10400, Sri Lanka.
[*]E-mail: manatunge@uom.lk

Abstract

The Kelani River Basin (KRB) is a major water resource in Sri Lanka, supporting domestic water supply and a range of urban, industrial, and agricultural activities. Water-quality monitoring in the basin covers physicochemical, nutrient, microbiological, and heavy-metal parameters, but parameter availability differs among stations. This study examines Pearson correlation matrices from 20 monitoring locations to identify spatially recurring and station-specific relationships. The results revealed strong but spatially variable relationships between heavy metals and other water-quality parameters. At Hanwella Bridge, zinc showed strong positive correlations with sulphate (r = 0.957) and chloride (r = 0.920), while at Karawanella Bridge, zinc was strongly correlated with electrical conductivity (r = 0.991). At Victoria Bridge, chromium was strongly correlated with turbidity (r = 0.824) and phosphate (r = 0.764). Iron exhibited moderate negative correlations with pH at Raggahawatte Ela (r = −0.543), Pugoda Ela (r = −0.524), and Kaduwela Bridge (r = −0.523). These findings highlight the potential of correlation analysis to identify site-specific relationships between heavy metals and other water-quality indicators, supporting targeted monitoring and the selection of candidate proxy variables.

Keywords: correlation analysis; heavy metals; monitoring; water quality

1 Introduction

River pollution is a major concern, particularly in river basins exposed to increasing urbanisation, industrial development, and agricultural activities. The discharge of untreated wastewater, industrial effluents, and agricultural runoff can introduce heavy metals, nutrients, organic pollutants, and pathogenic microorganisms into river systems, threatening aquatic ecosystems and human health [1].

Correlation analysis is widely used in water quality assessment to evaluate the strength and direction of relationships between measured water quality parameters. Multiple interacting factors influence river water quality, including natural geochemical processes, hydrological conditions, land-use patterns, and anthropogenic activities such as industrial discharges and agricultural runoff. Consequently, water quality parameters may show interrelationships that offer insight into the processes driving water chemistry and potential pollution sources [2].

Correlation analysis, particularly Pearson's correlation coefficient, quantifies the strength and direction of linear relationships between pairs of variables, with coefficients ranging from −1 to +1. Identifying these relationships can support the interpretation of complex water quality datasets, the identification of potential pollution indicators, and the prioritisation of monitoring parameters and locations. Furthermore, correlations between routinely measured parameters and pollutants that require laboratory analysis may provide a basis for developing proxy-based estimation approaches, subject to independent validation [2].

However, heavy-metal measurements may be limited in their temporal frequency and spatial coverage across monitoring locations. Examining correlations between heavy metals and routinely measured water-quality parameters can help identify potential proxy indicators for further investigation and support the targeted allocation of monitoring resources. Accordingly, this study investigates the spatial consistency and station-specific variability of correlations among water-quality parameters across 20 monitoring stations in the Kelani River Basin, with particular emphasis on heavy-metal relationships.

2 Materials and methods

The Kelani River is an important source of water for Sri Lanka, and the KRB includes urbanised and industrialised areas where water-quality pressures warrant sustained monitoring. This study used monthly water quality data from 20 water quality monitoring stations along the Kelani River from 2016 to 2020 for the analysis.

Pearson's correlation is a mathematical representation of

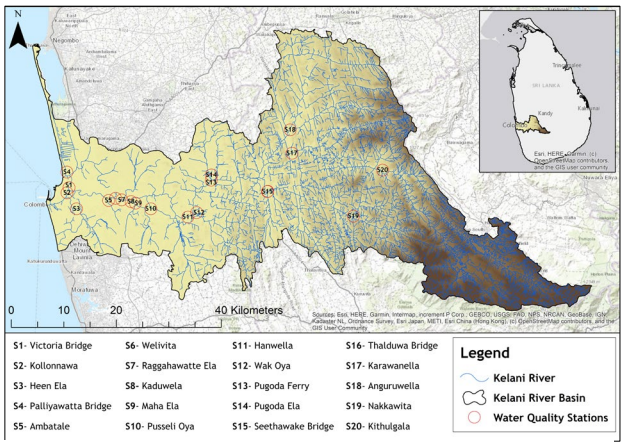


Fig. 1: Kelani River Basin and the locations of the river water quality monitoring stations

the correlation between two water quality parameters in a data set. Pearson's correlation coefficient (r) measures the linear relationship by considering the covariance of the two parameters. Although the parameters may exhibit non-linear characteristics, Pearson's correlation serves as a valuable initial screening tool to pinpoint parameters that exhibit significant linear correlations.

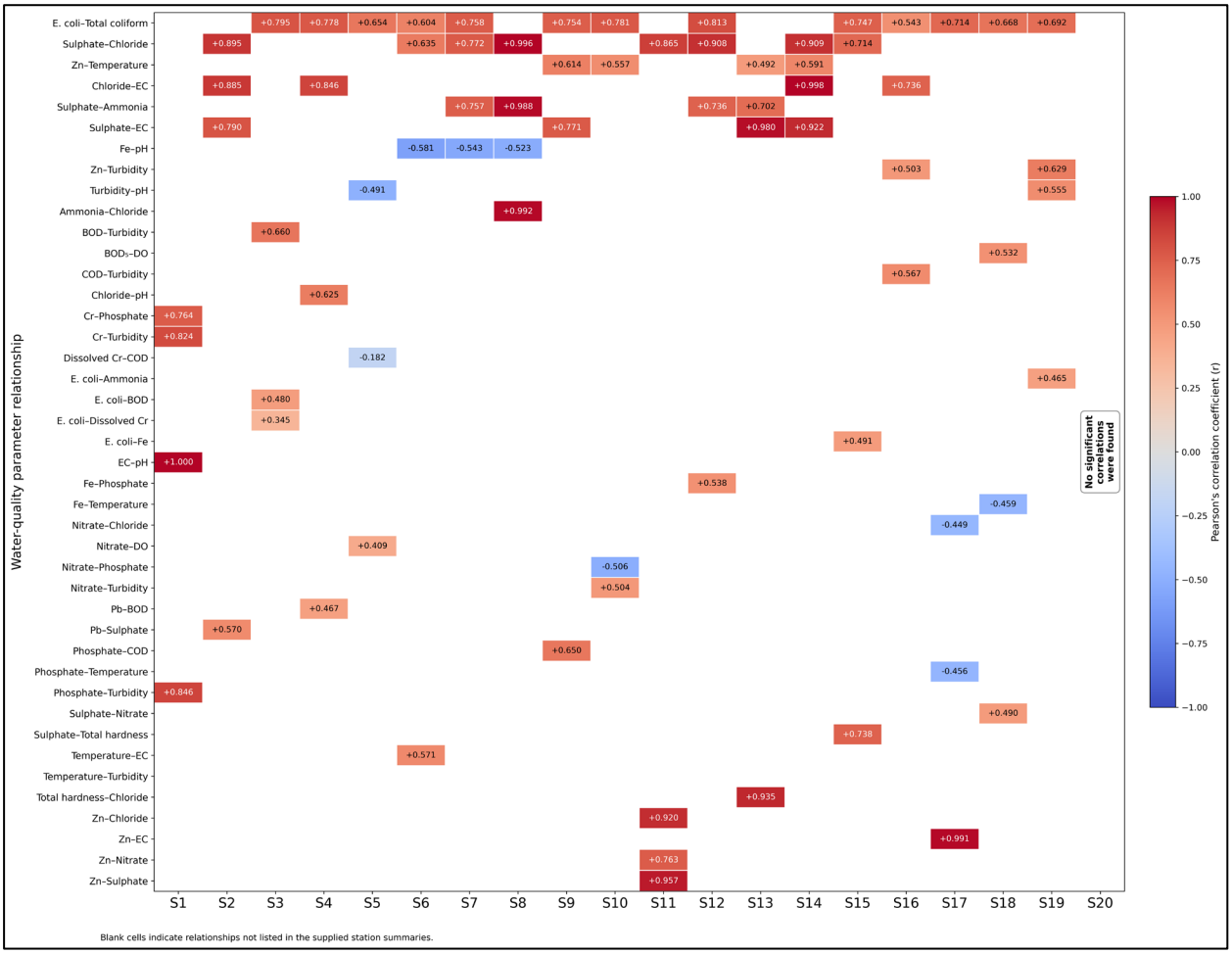


Fig. 2: Significant correlations between parameters for the 20 monitoring stations

3 Results and discussion

The spatial distribution of Pearson correlation coefficients across the 20 monitoring stations is illustrated in Fig. X.

The correlation analysis identified several recurring relationships across the Kelani River Basin (KRB). Electrical conductivity (EC) and total coliform exhibited strong positive correlations at 11 stations, namely Aguruwella, Hanwella Bridge, Heen Ela, Karawanella Bridge, Maha Ela, Nakkawita Bridge, Palliyawatta Bridge, Pusseli Oya, Raggahawatte Ela, Seethawake Ferry, and Wak Oya. Sulphate and chloride showed strong positive correlations at seven stations: Hanwella Bridge, Kaduwela Bridge, Pugoda Ela, Pugoda Ferry, Raggahawatte Ela, Victoria Bridge, and Wak Oya. Ammonia and sulphate were strongly correlated at five stations: Kaduwela Bridge, Pugoda Ela, Pugoda Ferry, Raggahawatte Ela, and Wak Oya. Sulphate and total hardness showed strong positive correlations at two stations, while iron and pH exhibited moderate negative correlations at Raggahawatte Ela, Pugoda Ela, and Kaduwela Bridge. These relationships highlight recurring patterns in the basin's water chemistry, although their strength varies spatially. The associations should therefore be interpreted in the context of local conditions and should not be taken as direct evidence of common pollution sources or causal relationships.

4 Conclusions

The correlation analysis revealed substantial spatial variability in the relationships among water quality parameters across the Kelani River Basin, with recurring positive associations between E. coli and total coliforms, and between sulphate and chloride at multiple monitoring stations.

The analysis revealed distinct relationships between heavy metals and other water-quality parameters across the basin. Zinc showed particularly strong positive correlations with sulphate and chloride at Hanwella Bridge, and with electrical conductivity at Karawanella Bridge, while chromium was strongly correlated with turbidity and phosphate at Victoria Bridge. Iron exhibited recurring negative correlations with pH at Kaduwela Bridge, Raggahawatte Ela, and Welivita, suggesting that pH may be a relevant parameter for further investigation of iron behaviour.

Reference

[1] WHO. A Global Overview of National Regulations and Standards for Drinking-Water Quality; World Health Organization: Geneva, Switzerland,2018; ISBN978-92-4-151376-0.

[2] Ahmed, U.; Mumtaz, R.; Anwar, H.; Shah, A.A.; Irfan, R.; García-Nieto, J. Efficient Water Quality Prediction Using Supervised Machine Learning. Water 2019, 11, 2210

An Overview of Water Quality in the Kelani River Basin: Current Status and Spatial–Temporal Changes

○ Luminda GUNAWARDHANA[1,2*], Nalintha WIJAYAWEERA[1,2] & Suraj THARUKA[1,2]
[1]Department of Civil Engineering, University of Moratuwa, Moratuwa 10400, Sri Lanka.
[2]UNESCO-Madanjeet Singh Centre for South Asia Water Management (UMCSAWM), University of Moratuwa, Moratuwa 10400, Sri Lanka.
[*]E-mail: lumindang@uom.lk.

Abstract

Kelani River is one of Sri Lanka's most important water resources, supplying water for domestic, industrial, and other uses, particularly in the Colombo metropolitan region. However, increasing urbanisation, industrial development, and wastewater discharges have contributed to the deterioration of river water quality. This study investigates overall water quality in the river, potential pollutant sources, and water quality variations in spatial and temporal scales. The study employs monthly water quality observations from 17 monitoring stations for 2016–2020, statistical analysis, unsupervised machine learning, and pollution indices. The findings identify industrial and domestic wastewater as major pollution pressures, with cadmium (Cd), iron (Fe) and zinc (Zn) among the significant industrial pollution indicators. Sewage pollution is particularly pronounced at several tributary and urban monitoring locations, while seasonal analysis reveals variations associated with monsoonal rainfall. Collectively, the studies demonstrate the value of combining water quality monitoring, machine learning and process-based modelling to identify pollution hotspots and support targeted river basin management.

Keywords: Water quality; industrial pollution; sewage pollution; machine learning; monsoonal variability.

1 Introduction

River water quality is increasingly threatened by urban expansion, industrialisation and inadequate wastewater management. These pressures are particularly important in the Kelani River Basin, which covers approximately 2,234 km² in western Sri Lanka and includes densely populated urban areas and industrial zones [1]. The river originates in the central highlands, flows through several urban and industrial areas, and discharges into the Indian Ocean. It is a critical source of raw water for the Colombo region, making pollution control essential for drinking-water security, aquatic ecosystems, and sustainable economic development.

This study intended to present an assessment of the overall water quality of the Kelani River using water quality observations, machine learning techniques, and water quality indices. Together, they provide a basis for identifying significant pollutants, distinguishing potential pollution sources, and understanding the influence of seasonal hydrological processes.

2 Study Area

The Kelani River Basin (Fig. 1) receives substantial rainfall from the monsoon. During 2016–2020, the mean annual rainfall across six rain gauges, estimated using the Thiessen Polygon method, was 3,720 mm. The Southwest Monsoon (May–Sep) contributed 53% of annual rainfall, followed by the Second Intermonsoon (Oct–Nov, 23%), First Intermonsoon (Mar–Apr, 15%) and Northeast Monsoon (Dec–Feb, 10%). Its upper reaches include relatively less urbanised areas, whereas the middle and lower reaches experience increasing population density, industrial activity and wastewater discharge. Industrial estates, urban settlements and tributaries draining developed areas are potential sources of pollution. Two major export processing zones, Biyagama and Seethawake, are located within the Lower Kelani River Basin (LKRB), along with numerous other industries situated along the river corridor. The basin also contains drinking-water abstraction points (e.g., Ambathale and Biyagama Water Treatment Plants) and numerous tributaries that convey both natural runoff and human-generated pollutants into the main river.

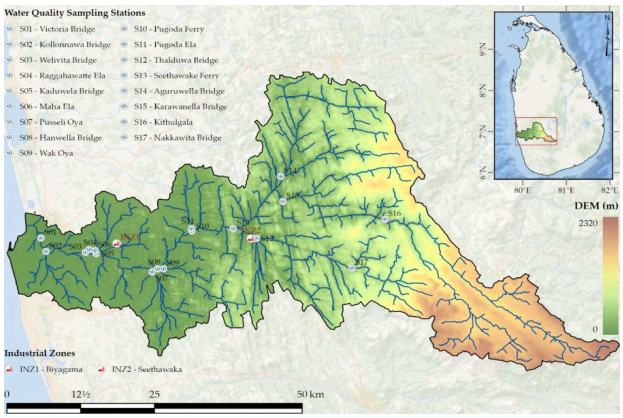


Fig. 1. Study area and water quality measuring points.

3 Method

The spatial and seasonal assessment analysed 17 water quality parameters at 17 monitoring stations (Fig. 1) using monthly observations from 2016 to 2020. Pearson correlation analysis, factor analysis, hierarchical clustering, and self-organising maps were applied to identify relationships among water quality parameters, underlying pollution patterns, and spatial differences between monitoring locations.

The sewage pollution study developed a basin-specific sewage pollution index (SPI) using five selected water quality parameters. The methodology involved parameter selection, sub-index development, weighting, and aggregation. Random forest modelling and the rank-order centroid method were used to determine parameter weights, while a long short-term memory artificial neural network (LSTM-ANN) was used to validate the results.

The industrial pollution study applied factor and cluster analyses alongside a novel industrial pollution index (IPI), using six parameters: nitrate, Fe, Cd, chromium (Cr), lead (Pb) and Zn. The index was validated using machine-learning models, and its results were compared with the spatial patterns identified through unsupervised learning.

4 Results and discussion

The analysis of the exceedance of the CEA standard limit suggested that the water quality in the Kelani River often exceeds the permissible limits (Table 1). Victoria Bridge and Kollonnawa stations are downstream of the Ambatale water intake, while the other sampling locations are upstream of the Ambatale intake. The results of the exceedance percentage analysis indicate a clear spatial variation in water-quality deterioration along the Kelani River. Stations in the downstream reaches showed comparatively higher exceedance levels, indicating greater water-quality deterioration and potential priority areas for further pollution assessment.

The combined findings indicate that pollution in the Kelani River Basin arises from multiple sources, particularly industrial effluents, domestic sewage and urban wastewater, with agricultural runoff and land-use-related sediment inputs also contributing to water quality deterioration.

Heavy metals are among the most significant industrial pollution concerns. The IPI study identified cadmium, iron, and zinc as major parameters influencing industrial pollution status. Cadmium was particularly concerning, with concentrations exceeding the applicable standard limits by approximately 29–32% across the 17 monitoring stations during 2016–2020. Iron also showed frequent exceedances, ranging from approximately 2% to 37%. These findings indicate the need for targeted investigation of industrial discharges and their effects on the river and its tributaries [1].

Sewage and domestic wastewater represent another major pollution pressure. The SPI study identified Maha Ela, Raggahawatte Ela, Seethawake Ferry, Kollonnawa Bridge, Victoria Bridge and Pugoda Ela as locations consistently classified as extremely polluted by sewage. Several are tributary or urban monitoring locations, highlighting the importance of investigating wastewater discharges entering the river through smaller waterways.

Organic pollution is also reflected in conventional indicators such as biochemical oxygen demand (BOD) and chemical oxygen demand (COD), while reduced dissolved oxygen (DO), elevated turbidity and suspended solids, and increased nutrient concentrations can indicate additional environmental pressures. Earlier assessments of the upper and lower catchments found that the lower catchment generally exhibited poorer water quality, with elevated COD, BOD, ammonia, nitrite, phosphate, turbidity and total suspended solids, together with lower DO at several locations. These parameters provide important supporting evidence of organic loading, nutrient enrichment, and sediment-related impacts.

Table 1 Frequency of exceedance (as a percentage) of the water quality standard limits.

Station	Turbidity	DO	COD	BOD	Sulphate	Chloride	Nitrate	Ammonia	TH	Fe	T. Coli	E. Coli
Victoria Bridge	96.6	22.5	52.3	12.4	6.1	40.4	3.4	56.1	21.5	1.9	66.1	92.7
Kollonnawa	98.2	80.0	77.8	54.5	2.9	32.7	0.0	85.4	13.3	9.3	54.5	97.6
Welivita	91.1	11.1	27.6	5.6	0.0	0.0	0.0	28.9	0.0	1.8	39.3	95.1
Raggahawatte Ela	98.9	94.4	71.3	54.4	4.5	2.2	5.7	65.1	0.0	10.9	26.8	80.5
Kaduwela	90.0	13.3	25.3	10.0	0.0	0.0	0.0	28.9	0.0	1.8	28.6	90.2
Maha Ela	96.7	87.8	71.3	47.8	0.0	0.0	0.0	50.6	0.0	25.5	12.5	92.7
Pusseli Oya	93.0	47.4	33.9	7.0	0.0	0.0	0.0	36.0	0.0	11.4	15.9	90.2
Hanwella	88.9	12.2	25.3	2.2	0.0	0.0	0.0	28.9	0.0	1.8	7.1	78.0
Wak Oya	87.8	17.8	24.1	3.3	1.5	0.0	1.1	31.3	0.0	5.5	16.1	78.0
Pugoda Ferry	85.6	13.3	25.3	3.3	1.5	0.0	0.0	21.7	0.0	1.8	30.4	85.4
Pugoda Ela	97.8	48.9	59.8	4.4	1.5	4.4	1.1	56.6	0.0	16.4	12.5	80.5
Thalduwa Bridge	64.4	2.3	15.5	1.1	0.0	0.0	0.0	22.2	0.0	1.9	11.9	93.3
Seethawake Bridge	93.3	45.6	50.6	20.0	9.1	0.0	0.0	71.1	0.0	3.6	30.4	85.4
Karawabella Bridge	60.9	6.9	16.7	2.3	0.0	0.0	0.0	16.0	0.0	1.9	6.8	82.2
Anguruwella	59.8	8.0	17.9	4.6	0.0	0.0	0.0	18.5	0.0	5.7	10.2	68.9
Nakkawita	51.2	2.3	16.9	3.5	0.0	0.0	0.0	13.8	0.0	1.9	6.9	70.5
Kithulgala	52.3	2.4	18.1	4.7	0.0	0.0	0.0	21.3	0.0	1.9	3.4	56.8

The latent-variable study found that monitoring stations near industrial zones and the river mouth exhibited greater water quality variability and more frequent exceedances of national guidelines. Industrial pollution variables and sewage-related variables showed distinct seasonal fluctuations [2], demonstrating that pollution cannot be understood solely through annual average concentrations. The lower basin exhibited greater variability in pollution-related latent variables than less urbanised upstream areas.

4 Conclusions

The four studies collectively demonstrate that the Kelani River Basin faces interconnected industrial, sewage-related and other anthropogenic pollution pressures, with generally greater water quality degradation in the lower basin. Cadmium, iron and zinc emerge as important industrial pollution indicators, while sewage pollution is particularly severe at several urban and tributary monitoring locations. Organic pollution, nutrient enrichment, reduced dissolved oxygen and elevated suspended solids provide further evidence of deterioration at affected sites.

Seasonal rainfall influences pollutant mobilisation and transport, while persistent downstream contamination indicates that additional sources may remain unidentified. Integrating water quality monitoring, machine-learning-based pollution indices and hydrological and pollutant transport models offers a promising framework for identifying priority locations and guiding interventions. Future management should prioritise industrial effluent control, sewage management, tributary-level monitoring and seasonal surveillance, particularly near drinking-water abstraction areas. These measures are essential to protect public water supplies, maintain river ecosystem health and improve the long-term sustainability of the Kelani River Basin.

Reference

[1] Wijayaweera, N., Gunawardhana, L., Bamunawala, J., Sirisena, J., Rajapakse, L., Patabendige, C. S., & Karunaweera, H. Use of machine learning and indexing techniques for identifying industrial pollutant sources: A case study of the lower Kelani River Basin, Sri Lanka. Water, 16, (2024). Article 2766.

[2] Wijayaweera, N., Gunawardhana, L.N., Kazama, S. et al. Exploring spatial and seasonal water quality variations in Kelani River, Sri Lanka: a latent variable approach. Environ Monit Assess 196 (2024). Article 1063.

Model and data interactions for hydrologic prediction in a changing climate

Seong Jin NOH[1*], Bomi KIM[1], Hyeonjin CHOI[2], Yaewon LEE[1], Hyuna WOO[1] & Minyoung KIM[1]

[1] Department of Civil Engineering, Kumoh National Institute of Technology, Gumi 39177, South Korea.

[2] Climate and Environmental Research Institute, Korea Institute of Science and Technology (KIST), Seoul 02792, South Korea.

*Corresponding author: Seong Jin Noh. E-mail: seongjin.noh@kumoh.ac.kr

Abstract

Data assimilation (DA) and deep learning (DL) provide overlapping ways to infer hydrologic behavior from incomplete information. Their interaction raises questions about which quantities observations can identify and when explicit updating adds value beyond using recent observations directly. Super-resolution can amplify the usable spatial information in coarse rainfall fields through relationships learned from finer observations, while emulation makes simulated system behavior rapidly available. Urban flood assimilation, CCTV-based reconstruction and climate storyline studies illustrate additional ways in which models and observations constrain or extend an assessment. Potential connections include learning assimilation components, updating learned representations and reconstructing training targets. These exchanges also carry assumptions and errors: accurate outputs need not uniquely identify physical states, and reproducing an analysis mean need not preserve uncertainty. Their assessment requires matched observation availability and attention to model error, uncertainty propagation and computational cost, with reconstruction distinguished from forecasts at positive lead times.

Keywords: Hydrologic prediction; Data assimilation; Deep learning; Uncertainty; Flood modeling; Climate storylines.

1 Introduction

Hydrologic inference is often underdetermined: different combinations of system states, parameters and model errors can produce similar observations. A water-level measurement may constrain the evolving flood while leaving its underlying causes unresolved. Additional data can help distinguish plausible explanations when they provide information about otherwise unobserved quantities. This places the representation of the system, and the assumptions connecting observations to that representation, at the center of hydrologic prediction.

Data assimilation (DA) and deep learning (DL) address this problem through overlapping forms of inference [1]. Assimilation constrains an evolving model representation, while learning can establish relationships across variables, spatial scales and events. Their combination can change both the quantities being estimated and the relationships through which observations inform them. Physically named states need not be uniquely identifiable, and learned states can contain useful hydrologic memory without corresponding to individual physical stores.

We examine when explicit updating adds value beyond using recent observations directly, how learned relationships enrich sparse or coarse information, and how errors propagate when DA and DL exchange information. We discuss what these interactions can contribute to hydrologic prediction and climate change impact assessment. Figure 1 summarizes the shared basis and potential connections of DA and DL.

2 Materials and methods

We draw on examples of urban flood assimilation, CCTV-based reconstruction, rainfall super-resolution, inundation emulation, and climate storyline assessment. The discussion focuses on the information available, the quantities inferred, and the assumptions connecting observations to model representations. These applications illustrate complementary capabilities and possible integration pathways, with attention to uncertainty and the conditions under which each approach is useful.

3 Results and discussion

What can observations identify? In synthetic urban flood experiments, sewer and surface observations constrain uncertain rainfall and inlet efficiency through a coupled sewer–surface model [2]. Their value depends on which uncertainties they resolve. CCTV-derived depths combined with simulated spatial patterns provide spatial reconstruction beyond individual observation points [3]. Neither an improved fit nor a physically named state guarantees a unique physical explanation. Conversely, a learned representation can contain useful hydrologic memory without identifying absolute storage. The relevant question is whether observations constrain the quantities needed for the intended prediction.

When does explicit updating add value? In one large-sample comparison, supplying recent discharge directly to a long short-term memory model was more effective than updating its internal states [4]. A differentiable process model, however, benefited mainly from hydrologic-state adjustment [5]. These findings are conditional on model representation and observation access. Irregular, indirect or multivariate observations motivate further investigation of explicit assimilation, but comparative evidence remains limited. A gain over a model without recent observations cannot establish the contribution of the updating algorithm itself.

What is transferred between methods? DL can approximate costly model propagation or learn recurring model errors. In the reverse direction, DA can update learned states or inputs and reconstruct training targets where measurements are sparse (Fig. 1c). These connections transfer assumptions and errors as well as information. Assimilation increments may combine structural, input, observation and sampling errors, so learning an increment does not identify a unique missing process. Likewise, an emulator that reproduces an analysis mean does not necessarily reproduce the associated uncertainty.

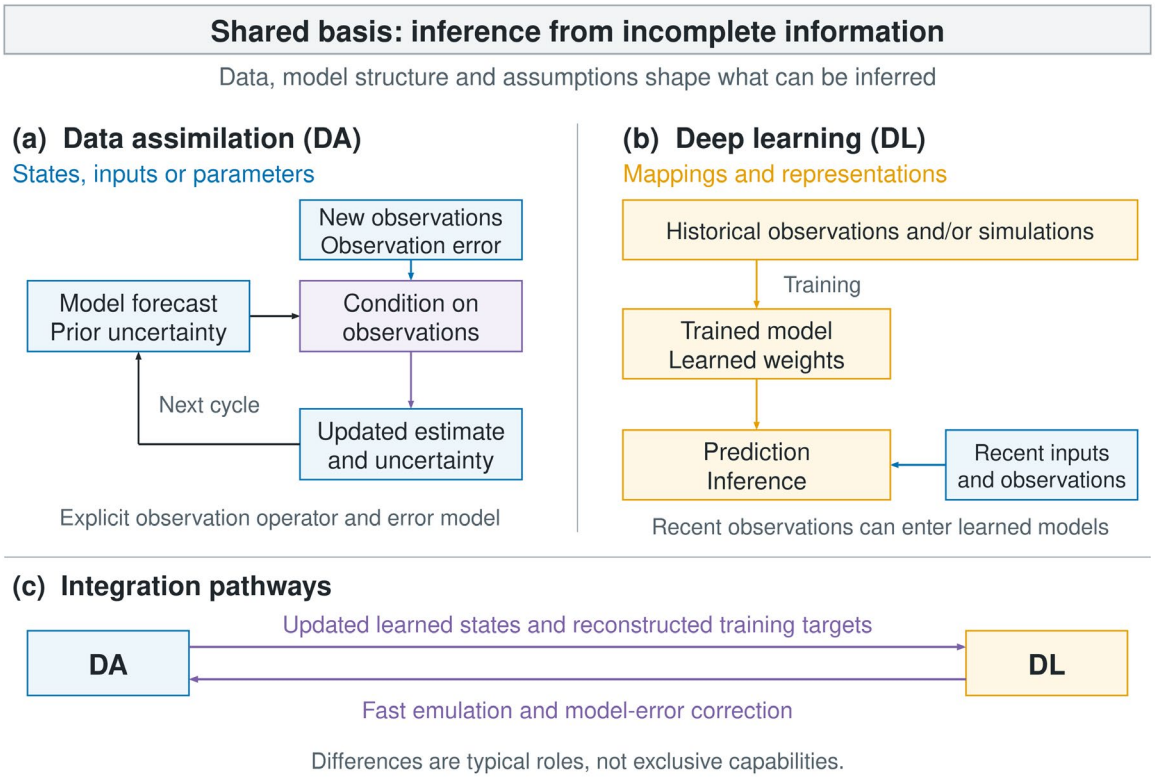


Fig. 1. Shared inference basis and integration pathways of data assimilation (DA) and deep learning (DL). The roles overlap: DA can update learned models, while DL can support observation-based inference.

How can learning amplify usable information? Super-resolution combines coarse inputs with spatial relationships learned from high-resolution examples. In the Radar-AMEDAS study, DL reconstructs 1 km rainfall fields from 10 km inputs, making finer spatial organization available for hydrologic assessment. This information amplification draws on the training data as well as the current input; the added detail is a conditional reconstruction. Inundation emulation similarly makes relationships encoded in hydrodynamic simulations available for repeated assessment. A deep-learning model reproduces a 48 h inundation sequence in approximately 5 s on a GPU [6]. Together, these applications suggest ways to enrich spatial information and expand the range of conditions that can be assessed within a response window.

How can unfamiliar conditions be examined? The multi-storyline assessment shows that precipitation-maximizing and inundation-maximizing scenarios can differ within selected ensembles. The Hinnamnor storyline study shows that warming-induced flood amplification varies across river scales [7]; the companion reservoir study proposes paired simulations to assess how routing modifies this pattern. These experiments can inform demanding evaluation cases for learned models and flood preparedness. Their results remain conditional on the specified scenarios and model configurations.

4 Conclusions

In this talk, we discuss how machine learning, particularly deep learning, and data assimilation infer hydrologic behavior from incomplete information and how their capabilities can be combined. Super-resolution, emulation, and observation updating illustrate opportunities to enrich spatial information and support rapid assessment.

With suitable representations and uncertainty treatment, their integration should help extend hydrologic prediction and climate change impact assessment across a wider range of conditions. Climate storylines offer a way to examine model responses under conditions beyond the observed record.

References

[1] A.J. Geer, Learning earth system models from observations: machine learning or data assimilation? Phil. Trans. R. Soc. A, 379 (2021) 20200089.

[2] B. Kim, Y. Lee, S. Lee, S.J. Noh, Probabilistic urban flood prediction with multivariate assimilation of sewer and surface observations, Water Res., 301 (2026) 126065.

[3] M. Kim et al., Observation-constrained urban flood mapping by fusing CCTV-derived flood depths with hydrodynamic simulations: the Dorim-cheon basin, Seoul, South Korea, J. Hydrol. Reg. Stud., manuscript under review.

[4] G.S. Nearing et al., Data assimilation and autoregression for using near-real-time streamflow observations in long short-term memory networks, Hydrol. Earth Syst. Sci., 26 (2022) 5493–5513.

[5] A. Jamaat et al., Update hydrological states or meteorological forcings? Comparing data assimilation methods for differentiable hydrologic models, J. Hydrol., 663 (2025) 134137.

[6] H. Woo, B. Kim, S.J. Noh, Dynamic urban pluvial flood emulation with SegFormer: Input design and diagnostic evaluation, manuscript under review.

[7] Y. Lee et al., Scale-dependent flood hazard amplification under warming climates: a tropical cyclone Hinnamnor storyline in South Korea, Geosci. Lett., 13 (2026) 56.

Beyond rainfall maxima: multi-storyline hydrodynamic assessment of inundation extremes under climate change

Bomi KIM[1*], Yusuke HIRAGA[2] & Seong Jin NOH[1]
[1]Department of Civil Engineering, Kumoh National Institute of Technology, Gumi 39177, Republic of Korea.
[2]Department of Civil and Environmental Engineering, Tohoku University, Sendai, Miyagi 980-8579, Japan.
[*]E-mail: kimbom3835@kumoh.ac.kr

Abstract

Flood hazard maps commonly derive worst-case inundation from the basin-average Probable Maximum Precipitation (PMP), implicitly assuming that the largest rainfall produces the largest inundation. We discuss whether this assumption holds under current and future climate conditions, using an integrated framework that propagates climate-conditioned, convection-permitting rainfall storylines through a high-resolution two-dimensional (2D) hydrodynamic model. Weather Research and Forecasting (WRF) rainfall storylines used storm transposition for current-climate conditions and added pseudo-global warming (PGW) perturbations for the 2050s and 2090s. Storylines selected by cumulative basin-average precipitation drove the GPU-accelerated 2D H12 model at 30 m resolution in two basins with contrasting terrain and land cover. We examine how changes in rainfall maxima are reflected in inundation-area maxima, whether the precipitation-maximising storyline also produces the largest inundation footprint within each ensemble, and how the differences are distributed across depth and land-cover classes. Preliminary results suggest smaller relative increases in inundation-area maxima than in precipitation maxima by the 2090s, and show that different storylines sometimes produce the two maxima within the selected ensembles, supporting the hydrodynamic evaluation of multiple candidate storylines in climate-conditioned flood hazard assessment.

Keywords: Probable maximum precipitation; Climate change; Storyline approach; Hydrodynamic modeling; Inundation extremes.

1 Introduction

Worst-case floods govern the design of critical infrastructure and the preparation of flood hazard maps. The Probable Maximum Flood (PMF) is conventionally defined as the flood produced by the Probable Maximum Precipitation (PMP), and worst-case inundation for hazard mapping is likewise derived from the basin-average PMP.

The translation from rainfall to flood is, however, strongly nonlinear: flood response depends not only on rainfall magnitude but also on its spatial and temporal organization, catchment processes and local topography. Whether rainfall-based storyline selection captures spatial inundation extremes under climate change remains insufficiently examined. We discuss a framework that propagates climate-conditioned, convection-permitting rainfall storylines through a high-resolution 2D hydrodynamic model, focusing on (1) how changes in rainfall maxima translate into inundation-area maxima and (2) whether the precipitation-maximising storyline also produces the largest inundation footprint within each selected ensemble.

2 Materials and methods

The framework links rainfall-storyline selection with ensemble hydrodynamic simulation. It was applied to two basins in northwestern Honshu, Japan, the Akagawa (AKB) and Arakawa (ARB) basins, which have similar drainage-network development but contrasting basin geometry and lowland extent (Fig. 1, Table 1). Topography and land cover were prepared on a 30 m grid with four land-cover classes: impervious surfaces, paddy fields, water bodies and other pervious surfaces.

Table 1 Characteristics of the study basins.

Characteristic	AKB	ARB
Basin area (km²)	856.7	1,150.0
Form factor	0.17	0.22
Area with slope < 2° (%)	9.52	3.79
Area at elevation ≤ 20 m (%)	13.80	1.42

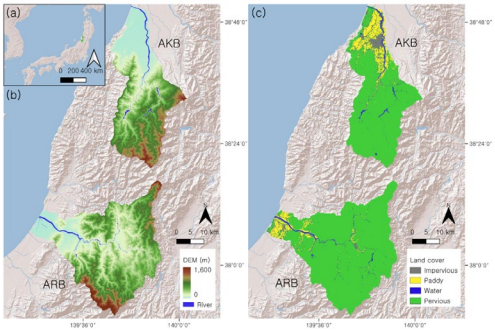


Fig. 1. Study areas: (a) location, (b) 30 m DEM and river network, (c) land cover.

Extreme rainfall storylines were obtained from the WRF simulations of the August 2022 northern Japan event by Hiraga et al. [1], based on the PMP-oriented framework of Hiraga et al. [2], which combines storm transposition with PGW perturbations derived from three global climate models under SSP2-4.5 for the 2050s and 2090s. Hourly rainfall from the 1.33 km WRF domain over the 96 h event period was mapped to the 30 m H12 grid. For each basin and climate period, candidate storylines were ranked by cumulative basin-average precipitation and the ten largest were selected

for inundation simulation (Fig. 2); the unshifted current-climate simulation (CTL) served as a reference.

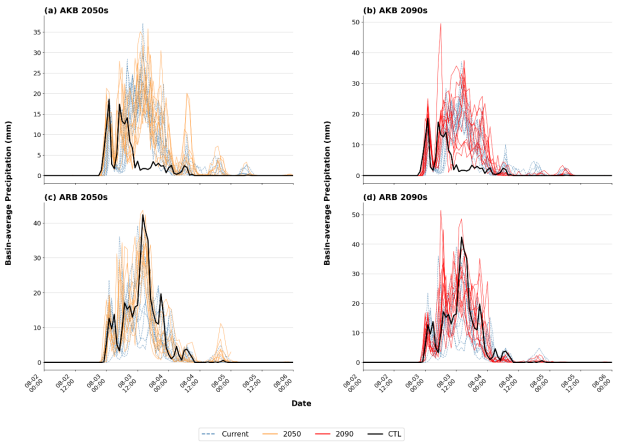


Fig. 2. Hourly basin-average precipitation of the selected storylines for (a, b) AKB and (c, d) ARB in the 2050s and 2090s. Black, CTL; blue dashed, current climate; orange and red, 2050s and 2090s.

Inundation was simulated with the physics-based 2D surface-flow hydrodynamic model [3]. Effective rainfall was calculated using runoff coefficients, with a uniform Manning's roughness coefficient of 0.03. Each storyline was simulated for 96 h from a dry initial condition. For the August 2022 event, a simulation using 1 km radar–rain gauge analyzed precipitation reproduced the main GSI-estimated inundation pattern near one basin outlet, with some overextension.

3 Preliminary results and discussion

Fig. 3 compares the ranking of the ten selected storylines by cumulative precipitation with their ranking by event-maximum inundation area, defined as the area of cells exceeding a water depth of 0.1 m at any time, excluding permanent water bodies. The precipitation-maximising storyline did not consistently produce the largest inundation footprint. Building on this correspondence analysis, we discuss how the ensemble maxima of precipitation and inundation area change from current-climate to 2090s conditions, and how the inundated area is distributed across depth and land-cover classes. Preliminary results suggest that inundation-area maxima increase relatively less than precipitation maxima by the 2090s. We also compare the precipitation- and inundation-area-maximising storylines in terms of their rainfall distribution and the depth and land-cover composition of their footprints, and consider possible roles of rainfall placement, timing and surface-flow redistribution, whose individual effects were not isolated.

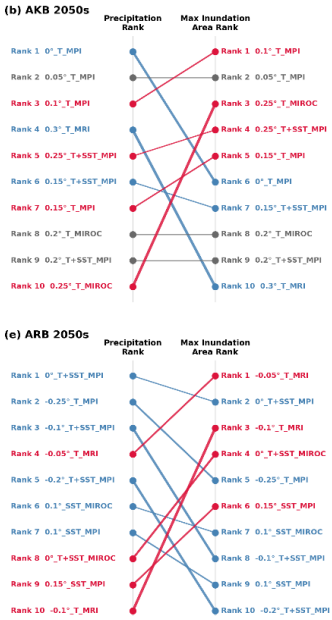


Fig. 3. Precipitation versus inundation-area rankings of the ten selected storylines (upper, AKB; lower, ARB; 2050s). Red and blue lines: inundation rank higher and lower than precipitation rank.

4 Conclusions

Propagating climate-conditioned, convection-permitting rainfall storylines through a high-resolution 2D hydrodynamic model showed that, within the selected ensembles, the precipitation-maximising storyline did not consistently produce the largest inundation footprint and that inundation-area maxima increased relatively less than precipitation maxima by the 2090s. Rainfall maxima alone therefore cannot fully characterize spatial inundation extremes under climate change, and multiple candidate storylines should be evaluated hydrodynamically against the intended inundation metric.

Reference

[1] Hiraga, Y., Watanabe, S., Yamashita, T., Takizawa, H., Climate change effects on probable maximum precipitation (PMP) of mesoscale convective systems: Model-based estimation and large ensemble-based frequency analysis, Journal of Hydrology, 661 (2025) 133724.

[2] Hiraga, Y., Tahara, R., Meza, J., A methodology to estimate probable maximum precipitation (PMP) under climate change using a numerical weather model, Journal of Hydrology, 652 (2025) 132659.

[3] Kim, B., Ryu, H., Lee, S., Lee, J.-H., Noh, S.J., Portable multi-GPU urban flood modeling via MPI-OpenACC: Evaluating acceleration, scaling, and workload-per-GPU, Environmental Modelling & Software, 200 (2026) 106957.